Alma Mater Studiorum
Università di Bologna

Dottorato di Ricerca in Fisica

XXIII Ciclo

Measurement of the atmospheric muon charge ratio with the OPERA detector

Author:
Nicoletta Mauri

Advisor:
Dott. Maximiliano Sioli

PhD Coordinator:
Prof. Fabio Ortolani

Anno Accademico 2009/2010

Contents

Introduction

Cosmic rays are atomic nuclei reaching the Earth from outside. Since their discovery in the beginning of the last century [1], great progress has been achieved towards the understanding of the origin, transport and acceleration mechanisms of the primary cosmic rays, their interaction processes in the galactic and extra galactic media, and also in the Earth's atmosphere, but they are still subject of intense research. The study of high energy cosmic rays is relevant for both astrophysics and particle physics.

- For astrophysics: even if cosmic rays were discovered one century ago their origin is still unknown. We have only some theoretical hypotheses about the mechanisms able to accelerate them up to the highest energies.
- For particle physics: part of the interactions between primary high energy cosmic rays and atmospheric nuclei occur in kinematic regions not yet studied at accelerators. In the center of mass, the highest energies reached by primary cosmic rays are about a factor 20 higher than the energies available at the LHC.

The interaction of primary cosmic rays in the Earth's atmosphere leads to the production of a cascade of secondary particles (air shower) with various components: electromagnetic showers, hadrons, muons and neutrinos. The last two are the penetrating components of the particle cascade. Since muons and neutrinos are able to reach underground and underwater depths, their study covers many aspects of cosmic ray physics.

Many cosmic ray experiments used several air shower-related observables which provide an understanding of the hadronic interactions and shed light on the chemical composition of the primary particles. The atmospheric muon charge ratio R_μ, defined as the number of positive over negative charged muons, is one of these observables. The behavior of the muon charge ratio is linked to the mechanism of multiple production of pions and kaons in the atmosphere, to the primary cosmic ray composition (in particular to ratio of protons to heavier primaries) and spectrum (the spectral index γ), and - at very high energy - to the contribution of prompt muons.

Underground experiments naturally select very energetic muons.
OPERA[1] is located in the underground Gran Sasso Laboratory, at an average depth of 3800 meters of water equivalent (m.w.e.). OPERA is the first large magnetized detector that can measure the muon charge ratio at the LNGS depth with a good acceptance for cosmic ray muons coming from above. The detector observes underground muons with a minimum surface energy of 1 TeV and their energy spectrum has a mean value of about 2 TeV. In this energy range the muon charge ratio is expected to rise due to the increasing kaon contribution. Moreover R_μ is expected to depend on the underground muon multiplicity which is related to the energy of the primary cosmic rays and to their chemical composition.

This thesis presents the measurement of the muon charge ratio with the OPERA detector. Chapter 1 sets the stage by summarizing cosmic ray physics and underlying the dependencies of the muon charge ratio. Chapter 2 describes the OPERA experiment with its hybrid electronic detectors/emulsion structure. Monte Carlo generators and detector simulation are described in Chapter 3. A dedicated software, presented in Chapter 4, was developed for the reconstruction of cosmic ray events. Chapter 5 reports the measurement of the underground muon charge ratio separately for single and multiple muon events. The charge ratio as a function of the surface muon energy is discussed in Chapter 6, in which possible interpretations in terms of cosmic ray and particle physics models are given.

---

[1] **O**scillation **P**roject with **E**mulsion t**R**acking **A**pparatus

Chapter 1

Cosmic ray muon physics

Cosmic ray muons detected by underground experiments like OPERA are not cosmic in origin: together with neutrinos, muons are the most abundant remnants of cosmic ray showers initiated by the primary cosmic radiation.

Primary cosmic rays are particles accelerated at astrophysical sources continuously bombarding the Earth's atmosphere. *Secondary* particles are produced by interactions of the primaries with the air nuclei. Muons predominantly originate from the decay of secondary charged pions and kaons: in this sense, muons are atmospheric in origin. The most important decay channels and respective branching ratios are

$$\begin{aligned} \pi^{\pm} &\rightarrow \mu^{\pm} + \nu_{\mu}(\bar{\nu}_{\mu}) \qquad (\sim 100\%) \\ K^{\pm} &\rightarrow \mu^{\pm} + \nu_{\mu}(\bar{\nu}_{\mu}) \qquad (\sim 63.5\%) \end{aligned} \tag{1.1}$$

Due to the small energy loss ($\sim$ 2 GeV in the whole atmosphere), the relatively long lifetime and the fairly small interaction cross section, atmospheric muons are the most numerous charged particles at sea level and the only ones able to arrive deep underground.

Because of the close relation between muon and neutrino production, the parameters characterizing muon physics can provide important information on atmospheric neutrino flux.

1.1 Primary cosmic rays

Primary cosmic rays are extraterrestrial stable charged particles and nuclei that span an energy range from a few MeV to beyond 10^{20} eV. Within fourteen decades in energy, the observed primary spectrum can be described by an inverse power law in energy with a flux which drops more than 30 orders of magnitude. The differential intensity of primary nucleons is given approximately by

$$\frac{dN}{dE} \propto E^{-\alpha} \tag{1.2}$$

where E is the energy-per-nucleon (including rest mass energy), $\alpha \equiv \gamma + 1 = 2.7$ is the differential spectral index of the cosmic ray flux and γ is the integral spectral index. This approximation is valid in the energy range from several GeV to beyond 100 TeV. At lower energies, not all particles can reach the Earth because of the shielding of the geomagnetic field and the "modulation" by the solar wind; correspondingly the observed spectrum starts flattening below 10 GeV.

At higher energies, two changes of the spectral index happen. Between 10^{15} and 10^{16} eV a steepening of the spectrum called *knee* is observed, when α changes from 2.7 to about 3. A further flattening of the spectrum occurs at around 10^{19} eV, known as the *ankle* of the spectrum. Above these ultra-high energies, just beyond 10^{20} eV, a rapid steepening of the spectrum, known as GZK cut-off, results from the inelastic interactions with the cosmic microwave background radiation. In order to illustrate these structures, it is common to scale the differential energy spectrum with a similar power law, $E^{2.5}$, as shown in Fig. 1.1.

The experimental features of the primary spectrum hold clues of the origin of cosmic rays. The cosmic radiation below the knee is explained by the Fermi mechanism, a stochastic acceleration in the shock fronts of supernova remnants [2], which naturally explains particle acceleration up to $\sim$ 100 TeV.

The origin of the knee in the energy spectrum is very important for the understanding of the origin of (galactic) cosmic rays. Many approaches are discussed in the literature. In the first scenario the knee is associated with the upper limit of acceleration by galactic supernovae. The maximum energy that can be achieved by the Fermi mechanism is proportional to the nucleus charge [4]:

$$E_{\text{max}} \leq Z \times 3 \times 10^{4}\,\text{GeV} \tag{1.3}$$

Thus, if there is a steepening of the spectrum due to the end-point of this kind of acceleration mechanism, then the composition should become progressively enriched in heavier nuclei as energy increases through the cut-off region [5]. Another cause can be a change in the propagation of galactic cosmic rays (rigidity cut-off), i.e. a rigidity-dependent leakage from the galaxy that increases with energy [6]. If the steepening depends on the rigidity, in the same way for all nuclei, then protons would steepen

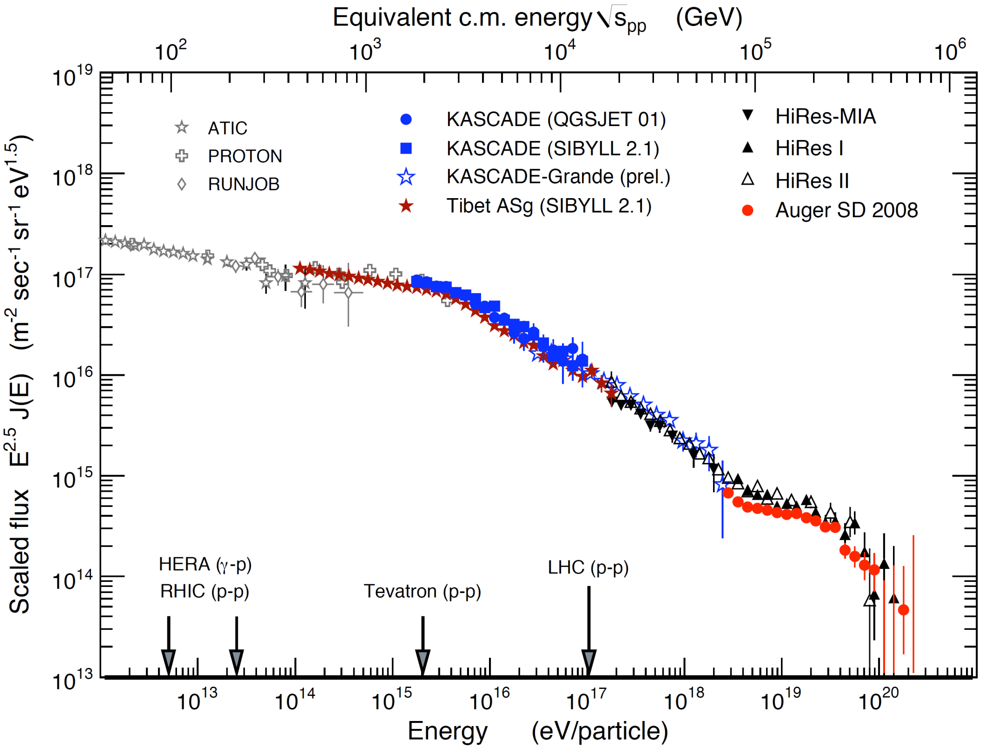

Figure 1.1: The all-particle spectrum of cosmic rays as obtained by direct measurements above the atmosphere as well as from air shower experiments. For references to the data see [3].

first, then helium, then CNO, and so on with the heavier nuclei. This scenario would give an increasingly heavy composition as well, in association with a steepening of the all particle energy per nucleus spectrum. A third cause can be the presence of different kinds of sources and acceleration processes, like neutron stars, binary systems and the same extensive supernova remnants [7]. This would predict the onset of a new proton source in this energy range, contrarily to the previous scenarios.

Regarding the ankle, a popular explanation is that the ankle is associated with the onset of an extragalactic population that is less intense but has a harder spectrum, thus dominates at sufficiently high energy. There are arguments [8] suggesting that the primaries with energy up to 10^{18} eV originate in this galaxy. Around the ankle energy, the confinement of the galactic cosmic rays is expected to end: the gyroradius in the 3 μGauss galactic field becomes comparable to the size of the galaxy. Since cosmic rays are no longer confined by galactic magnetic fields, it is natural to assume that they are produced by extragalactic sources.

The different theoretical hypotheses about the spectrum features predict enhancements of different chemical components. Clearly, a knowledge of the composition, especially for the knee, is crucial for discriminating among the possibilities. This has inspired a large set of measurements of the relative abundances of primary nuclei. The problem of determining the composition of the primary cosmic rays above the knee is obviously difficult because the primaries are not observed directly.

Direct measurements are possible up to 10^{15} eV/nucleon, where the cosmic ray flux is high enough to collect directly significant statistics, taking the detectors at high altitudes with balloons or satellites. The results of these experiments show that about 79% of the primary nucleons are free protons and about 70% of the rest are nucleons bound in helium nuclei [9]. The fractions of the primary nuclei are nearly constant over this energy range.

Above about 10^{15} eV/nucleon, the flux is too low and only indirect measurements are available. The spectrum is inferred by air shower detectors, but they do not provide any event by event information about the primary. The parameter γ, that is very sensitive to the chemical composition of the primaries, is measured from the distribution of secondary and tertiary particles. Even if several experiments have measured the energy spectrum in this energy region, and, however, the chemical composition of the cosmic ray particles around and above the knee is still not well understood, most of the experiment results go in the direction of a heavier composition.

At present, the major contribution on the uncertainties in the interpretation of indirect measurements is the limited knowledge of hadronic interaction models: part of cosmic ray interactions occurs in kinematic regions only partially covered by fixed target or collider experiments, i.e. high rapidity and high $\sqrt{s}$. Most of the observed particles at sea level or underground comes from the very forward region, where almost all the energy of the interactions is concentrated, allowing the shower penetration down the atmosphere. At present, there is a common effort to provide to the scientific community more and more detailed event generators for the modeling of these interactions.

1.2 Cosmic rays in the atmosphere

Upon encountering the Earth's atmosphere, primary cosmic rays interact with the air nuclei and produce fluxes of secondary, tertiary (and so on) particles. All these particles together create a cascade, called air shower.

The transverse momenta acquired by the secondaries cause the particles to spread laterally as they propagate in the target. As the cascade develops longitudinally, penetrating deeper and deeper into the target, the particles are less and less energetic since the energy of the initiating particle is split and redistributed among more and more participants.

An important parameter to describe the interactions and the subsequent propagation of the particles produced is the atmospheric depth X, measured in g/cm^2, defined as the integral in altitude of the atmospheric density above the observation level h:

$$X = \int_h^\infty \rho(h^{'})\, dh^{'} \approx X_0\, e^{-h/h_0} \tag{1.4}$$

In the last step, an approximation for an isothermal atmosphere was used, where $X_0 = 1030\,\mathrm{g/cm^2}$ is the atmospheric depth at sea level and $h_0 \simeq 8.4$ km is the scale height in the atmosphere [11]. The relation 1.4 is valid for vertically incident particles. For zenith angles $\theta \lesssim 70°$, for which the flat Earth approximation holds, the atmospheric depth is scaled with $1/\cos\theta$, giving the *slant depth.* For larger zenith angles, the curvature of the Earth has to be accounted for. The atmospheric profile gives a total horizontal atmospheric depth of about 36000 g/cm^2.

The atmosphere of the Earth consists mainly out of nitrogen and oxygen (0.78 and 0.21 of the total number of nuclei, respectively): the interaction target for the primary beam is half protons and half neutrons.

Fig. 1.2 shows the vertical fluxes of the major cosmic ray components in atmosphere as a function of the atmospheric depth, for $E > 1$ GeV. Except for protons and electrons near the top of the atmosphere, all particles are produced in interactions of the primary cosmic rays in the air. Muons and neutrinos are products of the decay of charged mesons, while electrons and photons originate in decays of neutral mesons.

The flux of cosmic rays through the atmosphere is described by a set of coupled cascade equations with boundary conditions at the top of the atmosphere to match the primary spectrum. Numerical or Monte Carlo calculations are needed to account accurately for decay and energy loss processes, and for the energy-dependences of the cross sections and of the primary spectral index γ. Approximate analytic solutions are, however, useful in limited regions of energy [2, 12].

Before going to present the transport equations and their solutions, since some approximations related to the physics of high energy collisions will be used, a brief recall of important features of strong interactions is presented.

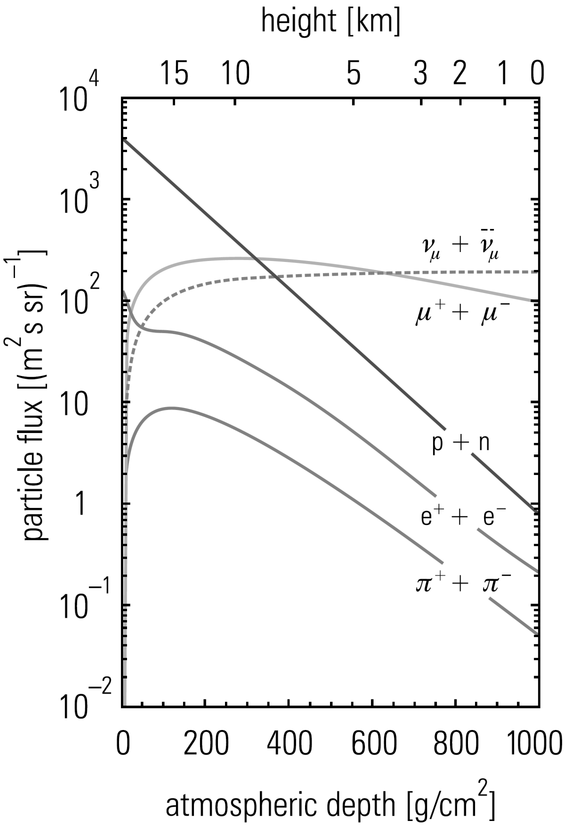

Figure 1.2: Vertical fluxes of cosmic rays in the atmosphere with $E > 1$ GeV estimated from the nucleon flux of Eq. 1.8 [10].

1.2.1 Phenomenology of strong interactions

Feynman Scaling Model The Lorentz *invariant inclusive cross section* for the production of secondary particles in a high energy hadronic interaction, $d^3\sigma/(dp^3/E)$, after integration of the phase space over the azimuthal angle, is given by the expression

$$\frac{E\, d^3\sigma_{\text{inel}}}{dp^3} = f(s, x, p_t) \tag{1.5}$$

where s is the center of mass energy squared and x, called the Feynman variable (Feynman-x), is the fraction of maximum available longitudinal momentum in the center of mass, defined as

$$x = \frac{p_{l,\mathrm{CM}}}{p_{l\,\max,\mathrm{CM}}} = 2\left(\frac{p_{l,\mathrm{CM}}}{\sqrt{s}}\right) \tag{1.6}$$

The Feynman hypothesis which is the foundation of the Feynman scaling model [13] states that in the limit, at very high energies ($s \gg m_p$, where m_p is the proton mass), the invariant cross section expressed in the variables x and p_t becomes asymptotically independent of the energy, E. Thus,

$$\lim_{s\to\infty} f(s, x, p_t) = \bar{f}(x, p_t) \tag{1.7}$$

Fragmentation and Limiting Fragmentation The fragmentation of relativistic nuclei in collision with target nuclei is an important topic where our knowledge is rather incomplete. It is observed in high energy hadronic collisions, predominantly in nucleon-nucleon collisions. Up to fairly high energies (hundreds of TeV) the bulk of the proton-proton inelastic cross section is due to processes with small transverse momentum (soft processes). Jet experiments have a simple interpretation only at relatively large transverse momentum (hard processes). In the forward region instead, QCD calculations become impractical because of the large coupling constants, which prevent the use of the perturbation theory. Then predictions rely on phenomenological models, albeit motivated by the ideas of the constituent quark model.

For these typical hadronic processes, the produced particles reflect the motions of the constituents. The distributions of longitudinal momentum of the produced particles reflect the momentum distributions of the constituents inside the incident particles: they tend to scale with the incident energy. The few fast products are closely correlated with the projectile nucleon, i.e., it looks as if they are fragments of the latter.

Using the formalism just introduced, the Feynman-x is limited to $-1 < x < 1$. The condition that x remains fixed as $s \to \infty$ ensures that the particle produced is a fragment of the beam particle or of the target particle (depending on the sign of $p_{l,\mathrm{CM}}$). These are called respectively the beam and the target fragmentation region. For $p_{l,\mathrm{CM}} > 0$ (forward fragmentation region) there is no dependence on the target in the scaling limit, and the distribution is similarly independent of the nature of the projectile when $p_{l,\mathrm{CM}} < 0$. The kinetic region $x \sim 0$ as $s \to \infty$ is called the central region: in this region the Feynman scaling is violated. The invariance with energy of the inclusive distributions, i.e. scaling, in the fragmentation region is the hypothesis of *limiting fragmentation* (HLF) [14].

Regarding cosmic ray showers, the particles in the narrow angle forward cone are of great significance as they are the principal carriers of the energy and determine to a good extent the longitudinal development of air showers. Of particular importance is the projectile fragmentation because it affects the development of a shower. The target fragments are in this case of lesser importance. Thus, the secondary production is independent of the target nature.

The link between proton-proton and proton-air collisions that is necessary to cross-check cosmic ray and accelerator or collider data is established with the help of Glauber theory [15]. Accurate elasticity measurements in collider experiments are difficult because of the inaccessibility of the very forward direction: the produced particles are "lost" in the beam pipe.

Up to now, accelerator experiments tested the HLF without significant deviations for interactions up to $\sqrt{s} = 0.9$ TeV [16].

1.2.2 Primary interaction and secondary propagation

A hadron cascade is a highly complex process. It is the basic energy transport mechanism in an air shower. The properties of hadron cascades are investigated with sophisticated Monte Carlo simulation programs on high speed computers. These allow to include easily every known process as well as distributions of stochastic processes that produce realistic fluctuations, and hypothetical mechanisms that are subject of exploration. Limiting factors for the complexity and accuracy of today's simulations are only imposed by our limited knowledge of the processes that we implement, by the capacity of the computers and the available computing time.

Nevertheless, the cascade process can be studied analytically, using the transport equations. The analytical approach can only yield average properties, the important topic of fluctuations is ignored, but it permits the overlook of the main functional features of the cascade and the trends of its development.

Primary interaction

The transport equations model the air shower development and depend on the properties of the particles and their interactions. The most simple approach to handle the hadron cascade is to consider a one-dimensional cascade (disregarding transverse momenta) and to limit the multitude of particles to nucleons, pions and muons. For nucleons, considered stable compared to their transit time through the atmosphere, the basic transport equation can then be written as

$$\frac{dN\,(E,X)}{dX} = -\frac{N(E,X)}{\lambda_N(E)} + \int_E^\infty \frac{N(E',X)}{\lambda_N(E')} F_{NN}(E,E') \frac{\mathrm{d}E'}{E} \tag{1.8}$$

where $N(E,X)dE$ is the downward flux of nucleons at depth X in the atmosphere within the energy interval E and $E+dE$, $\lambda_N(E)$ is the energy dependent interaction mean free path of nucleons and $F_{NN}(E,E^{'})$ is the dimensionless inclusive cross section (integrated over transverse momentum) for an incident nucleon of energy $E^{'}$ to collide with an air nucleus and produce an outgoing nucleon with energy E. In general, the inclusive particle production is defined as

$$F_{ij}(E,E^{'}) = E\frac{dn_j(E,E^{'})}{dE} \tag{1.9}$$

where dn_j is the number of particles of type j produced on average in the energy bin dE around E per collision of an incident particle of type i.

The first term on the right side of Eq. 1.8 represents the loss of nucleons due to interactions (sink term), the second term represents the gain of nucleons from interactions (source term).

The nucleon *mean free path* λ_N in atmosphere is given (in units of slant depth) by

$$\lambda_N = \frac{A\,m_p}{\sigma_N^{\rm air}} \tag{1.10}$$

where $\sigma_N^{\rm air}$ is the interaction cross section of nucleon in air, A is the mean mass number of air nuclei and m_p denotes the proton mass. For nucleons in the TeV range, $\sigma_N^{air} \approx 300$ mb; considering an average atmospheric nucleus with $A \approx 14.5$ we obtain $\lambda_N \approx 80$ g/cm^2. The mean free path λ_N is energy dependent through the σ_N energy dependence. In this context, the cross section for an inelastic collision of a nucleon with an air nucleus is assumed to be constant in energy. The probability of a nucleon to interact with the atmosphere along an infinitesimal dX in the slant depth is given by dX/λ_N. Since the total vertical atmospheric depth is about $1000\,\mathrm{g/cm}^2$ (more than 11 interaction lengths), the primary nucleons do not survive to the surface, but interact with the air creating secondary particles.

The function $F_{NN}(E,E^{'})$ is defined in the laboratory frame, where we can define $x_L = E/E^{'}$, the fraction of "beam" energy carried away by the outgoing produced particle. For high energy interactions, when $E \gg \sqrt{p_t^2+m^2}$, $x_L \approx$ Feynman-x (defined in the center-of-mass frame).

To solve this simple transport equation, we need to make some assumptions.

- It is assumed that a nucleus of mass A with energy E can be treated as A independent nucleons of energy E/A (so-called superposition approximation). This simplification is justified by the fact that at energies relevant for air showers the binding energies of the nucleons can be neglected. Furthermore, all primary nucleons are supposed to follow the same energy dependence, such that the total nucleon flux reads as

$$\Phi(E) = \Phi_0(E) \cdot E^{-\alpha} = (n_0 + p_0) \cdot E^{-\alpha} \tag{1.11}$$

where n_0 and p_0 denote the flux of neutrons and protons respectively.

- The interaction length does not depend on energy

$$\lambda_N(E) \to \lambda_N = \text{constant} \tag{1.12}$$

  This is justified by the mild logarithmic energy dependence of the cross section in the TeV range.

- The Feynman scaling holds (see Sec. 1.2.1), i.e.

$$F_{NN}\left(x_L = E/E^{'}, E\right) \to F_{NN}(x_L) \tag{1.13}$$

With these approximations, the solution to the cascade equation for nucleons is

$$N(E, X) = g(0)\, e^{-X/\Lambda} E^{-(\gamma+1)} \tag{1.14}$$

where the *attenuation length* is given by

$$\frac{1}{\Lambda} = \frac{1}{\lambda_N}\left[1 - \int_0^1 (x_L)^{\gamma-1} F_{NN}(x_L)\, \mathrm{d}x_L\right] \tag{1.15}$$

Thus, in the scaling validity region, nucleon fluxes in atmosphere have the same energy spectrum as the primary cosmic rays [17].

The *spectrum weighted moments* of the inclusive cross section characterize the hadronic interactions in atmosphere:

$$Z_{NN} \equiv \int_0^1 (x_L)^{\gamma-1} F_{NN}(x_L)\, \mathrm{d}x_L \tag{1.16}$$

The Z-factors determine the development of uncorrelated fluxes of secondaries in atmosphere [20]. Due to the steep primary spectrum, since $\gamma > 1$, the contribution to the Z-moment from $x_L \to 0$ is suppressed. Thus, the uncorrelated fluxes depend on the behavior of the inclusive cross section only in the forward fragmentation region, when x is sufficiently large. This characteristic validate the approximation done: Feynman scaling is still valid in the fragmentation region, i.e. HLF holds (Sec. 1.2.1), while is strongly violated in the central region.

A consequence of this formulation is the "leading pion" effect: when the multiplicity per collision of produced pions becomes very large, the smaller average energy fraction x of the pions from sea quarks makes their contribution suppressed. The "leading pion" (with $x > 0$) will reflect the projectile fragmentation region and thus the momentum distribution of its quarks. Since there are more protons than neutrons in the primary cosmic rays, given the two u-quarks of the proton, positive pions are favored in the fragmentation region.

Secondary production

All types of hadrons can be produced in the interactions of an energetic hadron. A system of coupled transport equations is needed to describe in details the hadron fluxes in atmosphere:

$$\frac{dN_i\,(E,X)}{dX} = -\Big(\frac{1}{\lambda_i} + \frac{1}{d_i}\Big) N_i(E,X) + \sum_j \int \frac{N_j(E_j)}{\lambda_j} F_{ji}(E_i,E_j) \frac{\mathrm{d}E_j}{E_i} \tag{1.17}$$

where d_i is the decay mean free path. The first sink term handles the energy dependent competition between interaction and decay.

If we couple the resulting set of transport equations in the proper sequence, we can in principle construct an analytic expression of the hadron cascade. The solution of these equations should allow us to compute the particle flux in space and time anywhere within the atmospheric target, i.e., the number, location and energy of the associated particles. However, this is an extremely difficult task, normally handled by Monte Carlo simulations or by numerical integrations. Analytic solutions, useful for qualitative understanding, can only be obtained for the most simple requirements and under severe approximations.

Considering pion initiated interactions, we neglect the production of a pair nucleon-antinucleon from pions and consider only the pion-nucleon interaction. A simplified equation of the pion flux is

$$\begin{aligned} \frac{d\Pi}{dX} = -\Big(\frac{1}{\lambda_\pi} + \frac{1}{d_\pi}\Big)\Pi + \int_0^1 \frac{\Pi(E/x_L,X) F_{\pi\pi}(E_\pi, E_\pi/x_L)}{\lambda_\pi(E/x_L)} \frac{\mathrm{d}x_L}{x_L^2} + \\ + \int_0^1 \frac{N(E/x_L,X) F_{N\pi}(E_\pi, E_\pi/x_L)}{\lambda_N(E/x_L)} \frac{\mathrm{d}x_L}{x_L^2} \end{aligned} \tag{1.18}$$

where d_π is the decay mean free path of pions in units of slant depth, defined as

$$\frac{1}{d_\pi} = \frac{m_\pi c^2 h_0}{E\, c\tau_\pi\, X\, \cos\theta} \equiv \frac{\epsilon_\pi}{E\, X\, \cos\theta} \tag{1.19}$$

The first term on the right hand side of Eq. 1.18 stands for the loss of pions through interaction and decay. Decay or interaction dominates depending on whether $1/d_\pi$ or $1/\lambda_\pi$ is larger. At the critical energy $\epsilon_\pi \equiv m_\pi\, c\, h_0/\tau_\pi$ the interaction probability in the atmosphere equals the decay probability. The remaining two terms account for pion production in nucleon and pion initiated interactions, respectively.

The scaling version of Eq. 1.18 is

$$\begin{aligned}\frac{d\Pi}{dX} = &-\Big(\frac{1}{\lambda_\pi} + \frac{1}{d_\pi}\Big)\Pi(E,X) + \\ &+\frac{1}{\lambda_\pi}\int_0^1 \Pi(E/x_L, X) F_{\pi\pi}(x_L)\frac{\mathrm{d}x_L}{x_L^2} + \\ &+\frac{Z_{N\pi}}{\lambda_N} E^{-(\gamma+1)} e^{-X/\Lambda_N}\end{aligned} \tag{1.20}$$

where the driving source term is proportional to the nucleon flux, with the same energy dependence $E^{-(\gamma+1)}$ and the Z-moments are defined analogously to Eq. 1.16.

Neglecting the pion decay ($E \gg \epsilon_\pi$), the scaling limit solution of Eq. 1.18, with boundary condition $\Pi(E,0) = 0$, is

$$\Pi(E,X) = E^{-(\gamma+1)} \frac{Z_{N\pi}}{1 - Z_{NN}} \frac{\Lambda_\pi}{\Lambda_\pi - \Lambda_N} \Big(e^{-X/\Lambda_\pi} - e^{-X/\Lambda_N}\Big) \tag{1.21}$$

The pion interaction and regeneration are included in a single variable, the attenuation length Λ_π:

$$\Lambda_\pi \equiv \frac{\lambda_\pi}{1 - Z_{\pi\pi}} \tag{1.22}$$

The pion flux reaches its maximum at $X \approx 140\,\mathrm{g/cm^2}$ [11], which corresponds to an altitude of about 15 kilometers, then declines as $\exp(-X/\Lambda_\pi)$.

The charged kaon initiated interactions are treated as the pion ones, the solution is obtained replacing the subscript π by subscript K. Numerical values for the attenuation lengths are $\Lambda_N \sim 120\,\mathrm{g/cm^2}$, $\Lambda_\pi \sim 160\,\mathrm{g/cm^2}$ and $\Lambda_K \sim 180\,\mathrm{g/cm^2}$ [2].

1.2.3 Atmospheric muon production

Most muons are produced high in the atmosphere in the first few generations of the interaction cascade. The small cross section implies that they can penetrate dense columns of matter without being much affected. Their subsequent influence on the average shower development is therefore negligible. Muons are the ideal test particles for investigating the regions of early shower development at great heights from ground level. They are the messengers carrying at least part of the shower history directly to the observer.

Muons are copiously produced by the decay of unstable secondary particles like pions and kaons, but also charmed particles. The bulk of the decay processes that yield muons are “ordinary” production mechanisms shown in Eq. 1.1: two-body decays with a $\nu_\mu(\bar{\nu}_\mu)$ associated to satisfy the conservation laws.

In addition to ordinary muons, high-energy muons can also be produced in semileptonic decays of charmed mesons like $D^{\pm}, D^0$ and others. The mean lifetime of charmed particles is $\leq 10^{-12}$ s. Hence, charmed particle decays are *prompt decays* and yield so-called *prompt* or *direct muons* that are in general energetic for kinematic reasons. All long-lived unstable particles (10^{-8} s $\leq \tau \leq 10^{-10}$ s) are subject to competition between interaction and decay as they propagate in the atmosphere. The probability for either process to occur depends on the mean life of the particle and is a function of its kinetic energy and the local atmospheric density, which is a function of altitude. This interrelationship is responsible for the zenith angle enhancement of the bulk of the muons in air showers, a phenomenon which muons from charmed particle decays do not exhibit. Since the production cross section of charmed mesons in proton-nucleon interactions is rather small, D decays contribute significantly only at very high energies.

Due to the energy degradation of the hadron cascade in a shower as it penetrates into deeper regions of the atmosphere, the hadronic collisions become less energetic and likewise the secondaries, some of which are prospective parent particles of the muons. Therefore, muons resulting from later generations of interactions that occur at greater depth in the atmosphere are less energetic than those from the first few generations originating from great heights.

Here we concentrate on pions and kaons as muon (and neutrino) parents. The analytical form of the muon production spectrum at a given height in the atmosphere can be derived by folding the two-body decay kinematics of the parent mesons with their production spectrum. The production spectrum of muons, differential in depth and energy, is given by

$$\mathcal{P}_\mu\left(E,X\right) = \sum_j \int_{E_{min}}^{E_{max}} \frac{dn_{\mu j}(E,E^{'})}{dE} \mathcal{D}_j(E^{'},X)\mathrm{d}E^{'} \qquad (1.23)$$

where $dn_{\mu j}(E,E^{'})/dE$ is the inclusive spectrum of muons from decay of particles j

with energy $E^{'}$. E_{min} and E_{max} are the minimum and maximum energy of the parent that can give rise to the muon. D_j is the spectrum of the decaying mesons of energy $E^{'}$ at depth X, which is the flux of such particles weighted by the decay probability $\epsilon_j/(E^{'}X\cos\theta)$. For two-body decay $M \to \mu\,\nu$, the kinematic limits on the laboratory energies of muons and neutrinos are

$$E(\mu^2/M^2) \leq E_\mu \leq E \tag{1.24}$$

and

$$0 \leq E_\nu \leq E(1-\mu^2/M^2) \tag{1.25}$$

where E is the laboratory energy of the decaying meson. Numerically, as a consequence of the small difference between the muon and the pion mass, the muon carries most of the energy in the $\pi \to \mu\,\nu$ decay: $\langle E_\mu\rangle/E_\pi = 0.79$ and $\langle E_\nu\rangle/E_\pi = 0.21$ in the laboratory frame. On the other hand, the kaon mass is much larger than the muon mass and therefore the muon and neutrino share about the same amount of energy in the $K \to \mu\,\nu$ decay: $\langle E_\mu\rangle/E_K = 0.52$ and $\langle E_\nu\rangle/E_K = 0.48$. This is the reason why, despite the small Z_{pK}-factors, kaons are an important source of atmospheric muon neutrinos, becoming the principal one at TeV energies.

The production spectrum of muons is calculated from Eq. 1.23, by folding the kinematics for $\pi \to \mu\,\nu$ and $K \to \mu\,\nu$ with the spectrum of decaying parents:

$$\begin{aligned}\mathcal{P}_\mu\,(E,X) = & \frac{\epsilon_\pi}{X\,\cos\theta\,(1-r_\pi)}\int_{E_\mu}^{E_\mu/r_\pi}\frac{\Pi(E,X)}{E}\frac{\mathrm{d}E}{E}+\\ & +\frac{0.635\,\epsilon_K}{X\,\cos\theta\,(1-r_K)}\int_{E_\mu}^{E_\mu/r_K}\frac{K(E,X)}{E}\frac{\mathrm{d}E}{E}\end{aligned} \tag{1.26}$$

where $r_j \equiv \mu^2/m_j^2$ and m_j is the mass of the parent meson j of total energy E.

1.3 Cosmic rays at the surface

Primary nucleons (protons and neutrons) with the initial high energies dominate over all other particle species down to altitudes of 9 km, where muons take over. Nucleons above 1 GeV/c at ground level are degraded remnants of the primary cosmic radiation. Because of the low interaction probability of neutrinos these particles are practically not at all absorbed in the atmosphere. Their flux increases monotonically because additional neutrinos are permanently produced by particle decays.

A measurement of charged particles at sea level clearly shows that, apart from some protons, muons are the dominant component (Fig. 1.2). They represent approximately 80% of the charged component of secondary cosmic rays at sea level. The muon flux through a horizontal area amounts to roughly one particle per cm^2 and per minute: $I_v(E_\mu > 1\,\mathrm{GeV}) \approx 70\,\mathrm{m}^{-2}\,\mathrm{s}^{-1}\,\mathrm{sr}^{-1}$ [21].

The muon spectrum at sea level is a direct consequence of the meson source spectrum. There are, however, several modifications. For low energies the muon decay probability is increased. A muon of 1 GeV with a Lorentz factor $\gamma \sim 10$ has a mean decay length $d_\mu \approx \gamma\,\tau_\mu\,c \sim 6$ km. Since pions are typically produced at altitudes of 15 km and decay relatively fast (for $\gamma = 10$ the decay length is only $d_\pi \approx 78$ m), the decay muons do not reach sea level but rather decay themselves or get absorbed in the atmosphere.

At high energies the situation is changed. For pions of 100 GeV ($d_\pi = 5.6$ km, corresponding to a column density of 160 g/cm^2 measured from the production altitude) the interaction probability dominates ($d_\pi > \lambda_\pi$). Pions of these energies will therefore produce further tertiary pions in subsequent interactions, which will also decay eventually into muons, but providing muons of lower energy. Therefore, the muon spectrum at high energies is always steeper compared to the parent pion spectrum.

The mean energy of muons at the ground is ≈ 4 GeV [9]. The energy spectrum is almost flat below 1 GeV, steepens gradually to reflect the primary spectrum in the 10-100 GeV range, and steepens further at higher energies because pions with $E_\pi > \epsilon_\pi$ tend to interact in the atmosphere before they decay. Asymptotically ($E_\mu \gg 1$ TeV), the energy spectrum of atmospheric muons is one power steeper than the primary spectrum. The overall angular distribution of muons at the ground is $\propto \cos^2\theta$, which is characteristic of muons with $E_\mu \sim 3$ GeV. At lower energy the angular distribution becomes increasingly steep, while at higher energy it flattens, approaching a $\sec\theta$ distribution for $E_\mu \gg \epsilon_\pi$ and $\theta < 70°$. Fig. 1.3 shows the muon energy spectrum at sea level for two zenith angles, $\theta = 0°$ and $\theta = 75°$. At large angles low energy muons decay before reaching the surface and high energy pions decay before they interact, thus the average muon energy increases.

If muons from inclined horizontal directions are considered, a further aspect has to be taken into account. For large zenith angles the parent particles of muons travel relatively long distances in rare parts of the atmosphere. Because of the low area density at large altitudes for inclined directions the decay probability is increased compared to the interaction probability. Therefore, for inclined directions pions will produce predominantly high-energy muons in their decay. The result of these considerations

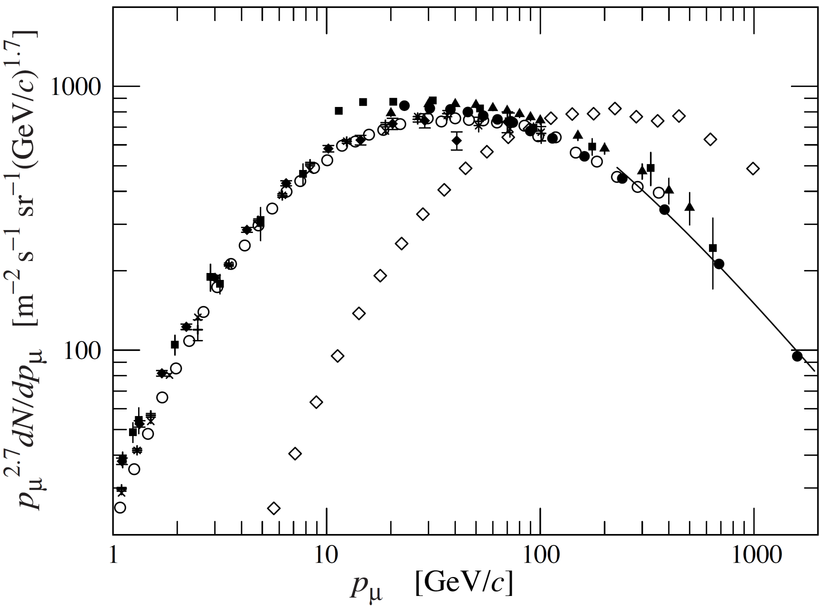

Figure 1.3: Spectrum of muons at $\theta = 0°$ and $\theta = 75°$. For references to the data see [9]. The line plots the result from Eq. 1.28 for vertical showers.

is in agreement with observation. Around 170 GeV the muon intensity at 83° zenith angle starts to outnumber that of the vertical muon spectrum [10]. The intensity of muons from horizontal directions at low energies is naturally reduced because of muon decays and absorption effects in the thicker atmosphere at large zenith angles.

Fig. 1.4 gives a quantitative impression of this effect. The calculation is a Monte Carlo type and accounts for the curvature of the Earth. 1 GeV/c muons fade fairly quickly with angle and their flux decreases by about a factor of 10 at 60°. The flux of 100 GeV/c muons is relatively flat up to $\cos\theta \simeq 0.2$ and then quickly declines. 1 TeV/c muons flux monotonically increases with the zenith angle. Especially sensitive to the zenith angle is the flux of TeV muons at the approach to the horizontal direction. A small difference in $\cos\theta$ changes dramatically the thickness and the density profile of the atmosphere and the muon energy spectrum. For this reason the measurements of almost horizontal muons are very difficult to interpret.

The muon energy and angular distribution reflect a convolution of production spectrum, energy loss in the atmosphere and decay.

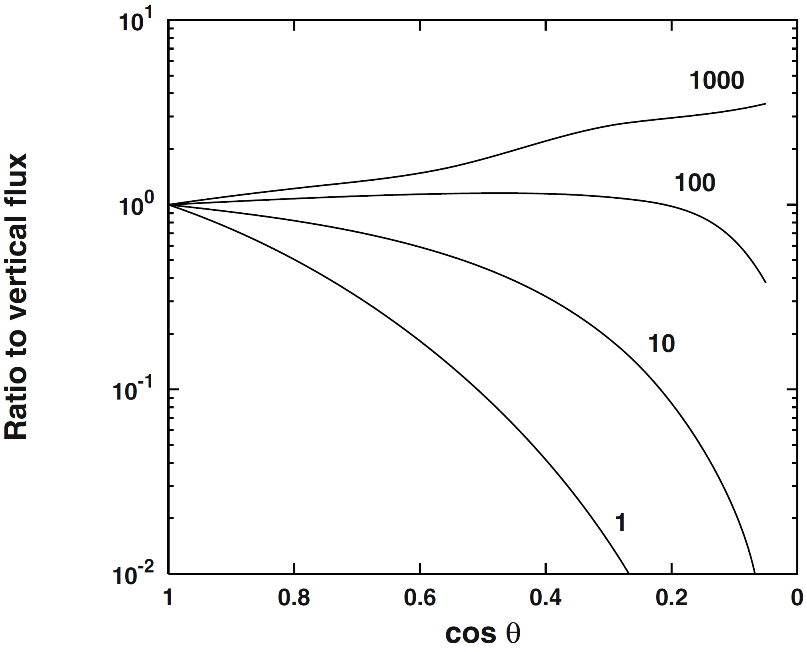

Figure 1.4: Monte Carlo calculation of the ratio of the inclined to the vertical muon flux as a function of the cosine of the zenith angle θ [11]. Muon momentum is given by each curve in GeV/c.

1.3.1 Muon flux

When the muon decay and energy loss are negligible ($E_\mu \gg \epsilon_\mu \simeq 1$ GeV), the muon energy spectrum at sea level is obtained after integration over the muon production in the whole atmosphere (Eq. 1.26) [2]

$$\mu(E_\mu) = \int_0^\infty \mathcal{P}_\mu(E_\mu, X)\mathrm{d}X \tag{1.27}$$

An approximate solution is

$$\frac{\mathrm{d}N_\mu}{\mathrm{d}E_\mu} \approx \frac{0.14\,E^{-2.7}}{\mathrm{cm}^2\,\mathrm{s\ sr\ GeV}} \left\{ \frac{1}{1+\frac{1.1\,E_\mu}{\epsilon_\pi(\theta)}} + \frac{0.054}{1+\frac{1.1\,E_\mu}{\epsilon_K(\theta)}} \right\} \tag{1.28}$$

The two terms give the contribution from pions and kaons. Eq. 1.28 neglects a small contribution from charm and heavier flavours, which starts to be important at very high energies.

A good approximation for $\epsilon_i(\theta)$ which takes into account the Earth's curvature is

$$\epsilon_i(\theta) = \frac{\epsilon_i(0)}{\cos\theta^*} \tag{1.29}$$

with

$$\cos\theta^* = \sqrt{1 - \sin^2\theta \left(\frac{R_e}{R_e + h}\right)} \tag{1.30}$$

where R_e is the Earth's radius and h is the average muon production height. By using Eq. 1.30 the zenith angle is evaluated at the muon production point and not at the detector site. By choosing $h = 30$ km an agreement within 5% with the precise $\epsilon_i(\theta)$ computation is obtained [12].

The competition of decay and interaction of the muon parents plays a crucial role and the relative importance of the two processes depends on energy. Three different energy regions are distinguishable:

- $E_\mu \gg \epsilon_{\pi,K}$: where $\epsilon_\pi = 115$ GeV and $\epsilon_K = 850$ GeV are the critical energies for vertical directions. The meson production spectrum has the same power law dependence of the primary cosmic rays, but the rate of their decay steepen one power of E_μ since the pion and kaon decay probability is suppressed. The thickness of the atmosphere is not big enough for pions to decay, since the Lorentz factor scale the decay length. Because of the $\cos\theta$ factor, pions decay more easily in non-vertical showers and muons at large angles have a flatter energy spectrum. For $E > \epsilon_\pi$ the inclined muon spectrum is flatter than the vertical one and the muon flux is respectively higher.

  The energy dependence is then $\mathrm{d}N_\mu/\mathrm{d}E_\mu = E_\mu^{-(\gamma+2)}$ and the zenith dependence is $\mathrm{d}N_\mu/\mathrm{d}\cos\theta \propto (\cos\theta)^{-1}$.

- $\epsilon_\mu \lesssim E_\mu \lesssim \epsilon_{\pi,K}$: in this energy range, almost all mesons decay and the muon flux has the same power law of the parent mesons, and hence of the primary cosmic rays. The muon flux is almost independent on the zenith angle.

- $E_\mu \lesssim \epsilon_\mu$: in this case, muon decay and muon energy loss become important and Eq. 1.28 overestimates the flux.

An important feature is the contribution of K decays to muon production as a function of the energy, shown in Fig. 1.5. The relative contribution increases substantially with energy even in this approximation in which Z_{NK} is assumed constant. At low energy, about 5% of vertical muons come from kaon decays; at $E_\mu \sim 100$ GeV, the fraction increases to about 8%, to 19% at 1 TeV and to 27% asymptotically. As a consequence of the two-body decay kinematics, the enhancement of the kaon contribution

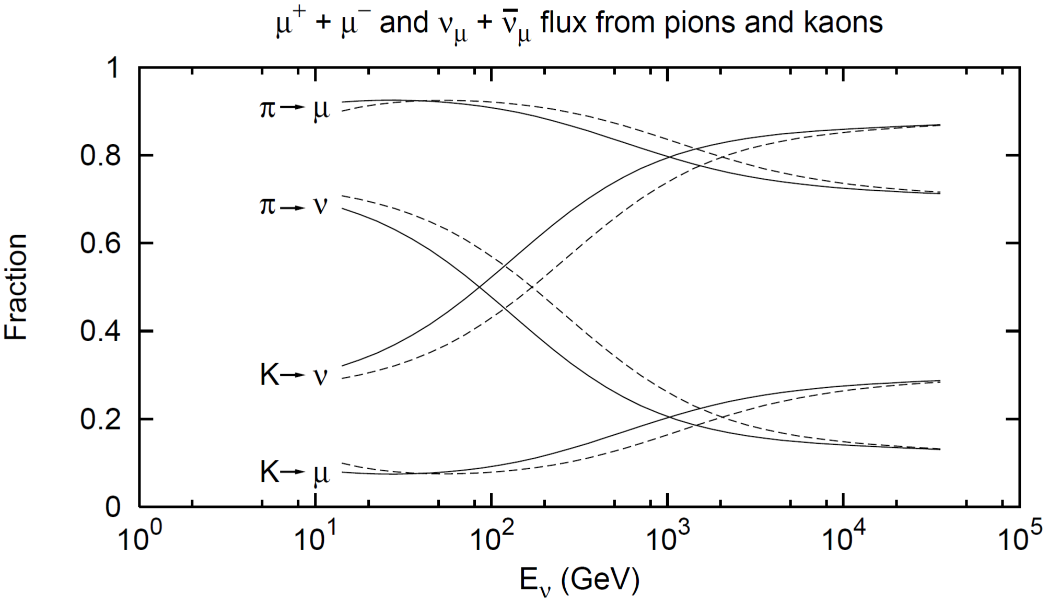

Figure 1.5: Fraction of muons and muon neutrinos from pion decay and from kaon decay vs. neutrino energy. Solid lines for vertical, dashed lines for zenith angle 60° [18].

to atmospheric neutrino production is particularly important. For the calculation of neutrino fluxes in the TeV energy range, the knowledge of the Z-factors for kaons is crucial.

An analogous additive term for charmed particles can be added to Eq. 1.28. Given a critical energy $\epsilon_{\mathrm{charm}} \approx 4 \times 10^7$ GeV, the angular distribution of the prompt muon component is isotropic, since the corresponding $\cos\theta$ factor is suppressed at least in the TeV energy range. Since the charmed particles almost always decay before interacting, the energy spectrum has the same spectral index of the primary one, while the ordinary muon component has an extra $\sec\theta/E_\mu$ factor, characteristic of the competition between decay and interaction. Because of their flatter energy spectrum, prompt muons will eventually dominate the muon flux at very high energy, despite the production of charm parents is lower compared to pion and kaons.

1.3.2 Muon charge ratio

The muon charge ratio $R_\mu \equiv N_{\mu^+}/N_{\mu^-}$, defined as the number of positive over negative charged muons, is an interesting quantity for the study of high energy hadronic interactions in atmosphere and the nature of the primaries. The behavior of the surface muon charge ratio is linked to our understanding of mechanism of multiple production of pions and kaons in the atmosphere, to the primary cosmic ray composition (in particular to ratio of protons to heavier primaries) and spectrum (the spectral index γ), and to the contribution of prompt muons at very high energy. As seen in the previous Sections, the scenario of multiple production of secondaries is dominated by soft particles, for which there is no clear and comprehensive theoretical understanding nor data from accelerators for kinematical reasons. For all these reasons, the muon charge ratio at sea level was extensively studied and the experimental measurements have been continuing [19]. Here a simplified model of the muon charge ratio is considered, in order to elucidate the essential physics features.

In an oversimplified model, the primary spectrum consists only of protons which interact once with the atmospheric nuclei, producing pions which all decay into muons [20]. Kaon contribution is ignored. The single-particle distribution for pions produced in proton-proton collision is, from Eq. 1.9

$$F_{p\pi^{\pm}}(E_{\pi}, E_p) \equiv \frac{E_{\pi}}{\sigma_{pp}^{\mathrm{inel}}} \frac{d\sigma_{p\rightarrow\pi^{\pm}}(E_{\pi}, E_p)}{dE_{\pi}} \tag{1.31}$$

where E_p and E_{π} are the laboratory energies of the primary proton and secondary pion, respectively, and $\sigma_{pp}^{\mathrm{inel}}$ is the total inelastic proton-proton cross section. Assuming a primary spectrum from Eq. 1.2

$$\frac{dN}{dE} = N_0 E^{-(\gamma+1)} \tag{1.32}$$

then the pion spectrum is

$$\Pi^{\pm}(E_{\pi}) \equiv \frac{d\Pi^{\pm}(E_{\pi})}{dE_{\pi}} = \frac{const}{E_{\pi}} \int_{E_{\pi}}^{\infty} dE E^{-(\gamma+1)} F_{p\pi^{\pm}}(E_{\pi}, E_p) \tag{1.33}$$

Applying the hypothesis of limiting fragmentation, Eq. 1.33 is simplified in the form

$$\Pi^{\pm}(E_{\pi}) = (const) E_{\pi}^{-(\gamma+1)} Z_{p\pi^{\pm}} \tag{1.34}$$

where, analogously to Eq. 1.16, the spectrum weighted moments are defined

$$Z_{p\pi^{\pm}} = \int_0^1 (x)^{\gamma-1} F_{p\pi^{\pm}}(x)\, \mathrm{d}x \tag{1.35}$$

Here the approximation $x_L = E_{\pi}/E \approx x$-Feynman is used, since it is valid for high energy interactions ($E, E_{\pi} \rightarrow \infty$, see Sec. 1.2.2). Consequently, in this model, the muon charge ratio is given by

$$R_\mu \equiv \frac{\mu^+(E_\mu)}{\mu^-(E_\mu)} = \frac{\Pi^+(E_\pi)}{\Pi^-(E_\pi)} = \frac{Z_{p\pi^+}}{Z_{p\pi^-}} \tag{1.36}$$

This simple model reveals the salient features of the muon charge ratio:

1. In this approximation, when the pion contribution can be considered the only one, from Eqs. (1.34)-(1.36) R_μ results explicitly independent of the muon energy.
2. $R_\mu > 1$ because the proton fragments more often into π^+ than π^-.
3. R_μ depends on the power γ of the primary spectrum.
4. R_μ does not depend on the nature of the target nuclei: the $x > 0$ forward region reflects the projectile nature.
5. Pionization region ($x \sim 0$) is suppressed: the steepness of the primary spectrum in the weighting factor $x^{\gamma-1}$ minimize the effects of the central region, where the Feynman scaling is violated.

For $x > 0$, the initial proton charge causes $F_{p\pi^+}(x) > F_{p\pi^-}(x)$.

An analytic estimate considering both protons and neutrons in the primary flux is presented in [20]. Still accounting only for muons from pion decay, the result for the muon charge ratio is

$$R_\mu = \frac{1 + \delta_0 \mathcal{A}\mathcal{B}}{1 - \delta_0 \mathcal{A}\mathcal{B}} \approx 1.25 \tag{1.37}$$

where δ_0 is the relative proton excess at the top of the atmosphere ($\delta_0 \equiv (p_0 - n_0)/(p_0 + n_0)$),

$$\mathcal{A} \equiv (Z_{p\pi^+} - Z_{p\pi^-})/(Z_{p\pi^+} + Z_{p\pi^-})$$

and

$$\mathcal{B} \equiv (1 - Z_{pp} - Z_{pn})/(1 - Z_{pp} + Z_{pn})$$

The equations were simplified by the following isospin symmetries valid for isoscalar targets ([22]):

$$Z_{pp} = Z_{nn} \quad Z_{pn} = Z_{np}$$

and

$$\begin{aligned} Z_{\pi^+\pi^+} &= Z_{\pi^-\pi^-} \quad Z_{p\pi^+} = Z_{n\pi^-} \\ Z_{\pi^+\pi^-} &= Z_{\pi^-\pi^+} \quad Z_{p\pi^-} = Z_{n\pi^+} \end{aligned}$$

Experimentally one observes that the charge ratio of muons at sea level is constant over a wide momentum range (10 GeV - few hundreds of GeV) and takes on a value $R_\mu \approx 1.27$.

The muon charge ratio reflects the excess of protons over neutrons in the incident cosmic rays. This excess is "remembered" and transmitted through the interactions in atmosphere, even if the multiplicity per collision of produced pions, the muons' parents, becomes very large. Because of the steepness of the primary cosmic ray spectrum, muons of a given energy come from relatively fast secondaries; i.e. they reflect the projectile fragmentation region. Since the fragmentation region of the proton reflects the momentum distribution of its quarks, and since it has two u-quarks of charge $+2/3$ and only one d-quark of charge $-1/3$, positive pions are favored in the fragmentation region. This causes an excess of positive over negative muons at all energies. The energy independence of the ratio also reflects the invariance with energy of the inclusive distributions, i.e., scaling in the fragmentation region (HLF, see Sec. 1.2.1).

At $E_\mu > \epsilon_K$, the kaon contribution becomes important, as seen in Sec. 1.3.1. When a s-$\bar{s}$ quark pair is created in a sufficiently high energy hadronic collision, conservation of the strangeness and baryon quantum numbers S and B is responsible for the difference between the kaon Z-factors. Whereas a K^+ ($B = 0$, $S = 1$) can be produced together with a Λ ($B = 1$, $S = -1$), the production of a K^- requires at least one associated baryon and an additional strange meson. In the process $pp \rightarrow \Lambda K N +$ anything, two-particle correlation is important and the momenta of these two particles will be correlated as well.

Thus, positively charged kaons are generated much more frequently than K^- because of the $K^+\,\Lambda$ production. This reflects in $Z_{pK^+} \gg Z_{nK^-} \approx Z_{pK^-}$, differently from the pion symmetries. The ratio K^+/K^- is greater than the ratio π^+/π^-: the increase with energy of the muon charge ratio R_μ reflects the increasing importance of kaons in the TeV range.

1.4 Cosmic rays underground

Primary cosmic rays almost never reach sea level. Secondary particles like hadrons, electrons and γ-rays interact immediately with the rock and are quickly absorbed. 10 meters of rock provide two or three times more column depth than the whole atmosphere. Only muons and neutrinos penetrate to significant depths underground. The muons produce tertiary fluxes of photons, electrons, and hadrons, that constitutes the last remnants of the cosmic ray shower.

The spectrum of underground muons still keeps the information on the primary cosmic ray flux. Deep underground detectors are not subject to the time restrictions of balloon and satellite experiments, so they can measure the muon flux for a very long time. But the muon spectrum at high energy ($E_\mu \sim 1$ TeV) steepen one power and the intensity is decreased by a factor 1000 with respect to the primary cosmic ray flux, so underground detectors have to be big. And the penetrating component of cosmic rays underground is a complex convolution of different processes. In addition to a good description of the muon production spectrum also the muon energy loss at high energy should be known very well, as the composition and the thickness of the rock overburden should be described in details.

Energy loss processes for muons can be divided into two categories: continuous and discrete. The former is due to ionization, which depends weakly on muon energy and can be considered nearly constant for relativistic particles. For GeV muons, this is the only essential energy loss process. At the underground detector depths, discrete energy losses become important: bremsstrahlung, direct electron-positron pair production and electromagnetic interaction with nuclei (photoproduction). These radiative processes are discrete bursts along the muon trajectory. On average, however, the energy loss rate is proportional to E. In general then the total muon energy loss is

$$\frac{\mathrm{d}E_\mu}{\mathrm{d}X} = -a - bE_\mu \tag{1.38}$$

where $b = b_{br} + b_{pair} + b_{ph}$ is the sum of fractional energy loss in the three radiation processes. Since the material and the density of the overburden vary for different experiments, the slant depth X is commonly given in units of meters of water equivalent (1 m.w.e. $\equiv 10^2$ g/cm^2).

1.4.1 Propagation through rock

The standard rock is defined as a common reference for deep underground detectors. It is characterized by density $\rho = 2.65$ g/cm^3, atomic mass $A = 22$ and charge $Z = 11$. When comparing measurements done at various locations, it is necessary to correct for differences in density of rock. The factors a and b are mildly energy dependent as well as dependent upon the chemical composition of the medium: in particular $a \propto Z/A$ and $b \propto Z^2/A$. The parameterization in standard rock gives the values $a \simeq 2$ MeV per g/cm^2 and $b \approx 4 \times 10^{-6}$ cm^2/g [11]. The critical energy is the energy ϵ_μ at which ionization energy loss equals radiation energy loss: $\epsilon_\mu \equiv a/b \simeq 500$ GeV, above which discrete processes dominate over continuous ones. The general solution of Eq. 1.38 is the average energy $\langle E_\mu \rangle$ of a beam of muons with initial energy $\mathcal{E}_\mu$ after penetrating a depth X of rock:

$$\langle E_\mu(X)\rangle = (\mathcal{E}_\mu + \epsilon_\mu)e^{-bX} - \epsilon_\mu \tag{1.39}$$

The minimum energy required for a muon at the surface to reach slant depth X is the solution of Eq. 1.39 with residual energy $E_\mu = 0$:

$$\mathcal{E}_\mu^{min} = \epsilon(e^{bX} - 1) \tag{1.40}$$

The range R for a muon of energy $\mathcal{E}_\mu$, i.e. the underground depth that this muon will reach, is

$$R(\mathcal{E}_\mu) = \frac{1}{b}\ln(1 + \frac{\mathcal{E}_\mu}{\epsilon_\mu}) \tag{1.41}$$

The above quantities are average values, for precise calculations of the flux of muons underground one needs to take into account fluctuations in range. These expressions are good under the assumption that the muon energy loss is continuous and that muons lose equal amount of energy in propagating through 1 g/cm^2 of matter. This is approximately true for energies up to 100 GeV, when ionization dominates. At higher energy the muon energy loss is not continuous: muons can occasionally lose a major fraction of their energy in a single, so-called catastrophic collision. Because of the stochastic character of muon interaction processes with large energy transfers (e.g., bremsstrahlung) muons are subject to a considerable range straggling [10]. Fluctuations are inherent to the radiative processes, and they replace the range R with a distribution of ranges. The higher $\mathcal{E}_\mu$ is, the more dominant are the radiation processes and the more important are the fluctuations of the energy loss: the range distribution becomes broader [12].

1.4.2 Muon bundles

Multiple muon events are closely packed bundles of muons, usually of high energy, that originate from parents created by the same cosmic ray primary. Multi-muon events are used to explore the properties of very high energy hadronic interactions and to study the longitudinal development of showers. This latter aspect is a link to the mass of the shower initiating primary. In general, high-energy muons are produced by high-energy primaries and, in particular, muon showers correlate with even higher primary energies and heavier primary mass. The muon multiplicity n_μ is an observable which manifests primary mass sensitivity [21].

The primary interaction vertex of particles which initiate the air showers is typically at an atmospheric altitude of 15 km. Since secondary particles in hadronic cascades have small transverse momenta (about 300 MeV/c only), as seen in Sec. 1.2.1, the high-energy muons essentially follow the shower axis. Considering a single interaction of a primary nucleon, producing mesons of energy $E_{\pi,K}$ with transverse momentum p_t at a slant height h_{prod}, the separation of a high energy muon from the shower axis is given by [25]

$$r \sim \frac{p_t}{E_{\pi,K}} h_{\text{prod}} \tag{1.42}$$

For primary energies around 10^{14} eV, lateral displacements of energetic muons (≈ 1 TeV) of typically several meters are obtained at shallow depths underground. This displacements are exclusively caused by transferred transverse momenta; typical multiple-scattering angles for muon energies ~ 100 GeV in thick layers of rock (50-100 m) are on the order of a few mrad [10].

The multiplicity of produced secondary particles increases with energy of the initiating particle (for a 1 TeV proton the charged multiplicity of particles for proton-proton interactions is about 15). Since the secondaries produced in these interactions decay predominantly into muons, one observes bundles of nearly parallel muons underground in the cores of extensive air showers.

1.4.3 The OPERA kinematic region of interest

The OPERA experiment is a hybrid electronic detector/emulsion apparatus, located in the underground Gran Sasso laboratory, at an average depth of 3800 meters of water equivalent (m.w.e.). While the primary physics goal of the experiment is to detect neutrinos from the CNGS beam, the great depth and wide acceptance of the detector combined with the overburden of the Gran Sasso site open the possibility to use OPERA as an efficient cosmic-ray muon detector. In particular it is the first large magnetized detector that can measure the muon charge ratio at the LNGS depth, with an acceptance for cosmic ray muons coming from above $\mathcal{A} = 599$ m^2 sr ($\mathcal{A} = 197$ m^2 sr for muons crossing the spectrometer sections). OPERA detects underground muons with a minimum surface energy of 1 TeV produced by primary cosmic rays of $\sim$20 TeV/nucleon average energy. The average underground muon momentum is $\sim$270 GeV/c [72].

Eq. 1.28 contains most of the aspects already discussed in the previous Sections. First we note that the correct variable to describe the evolution of the charge ratio is the product $\mathcal{E}_\mu \cos\theta^*$, the "vertical surface energy" [23, 24]. The evaluation of the muon surface energy $\mathcal{E}_\mu$ depends on the rock depth crossed by the muon to reach the detector and therefore the distribution of $\mathcal{E}_\mu \cos\theta^*$ is related to the shape of the overburden. Measurements of the muon charge ratio at high energies and large zenith angles, corresponding to $\langle \mathcal{E}_\mu \cos\theta^* \rangle \sim 0.5$ TeV, are given in Ref. [77]. More recent data with large statistics at $\langle \mathcal{E}_\mu \cos\theta^* \rangle \sim 1$ TeV are presented in Ref. [78]. These results suggest a smooth transition toward the energy region where kaon contribution becomes significant.

The LNGS laboratory is located at $\langle \mathcal{E}_\mu \cos\theta^* \rangle \simeq 2$ TeV, well above the kaon critical energy ϵ_K. This allows the measurement of the ratio Z_{NK^+}/Z_{NK^-} whose value is poorly known in the fragmentation region. This has also a strong impact on the evaluation of the flux of TeV atmospheric neutrinos, which are dominated by kaon production.

Moreover, given the size of the OPERA detector and the average separation between multi-muons (Sec. 1.4.2), it is possible to measure separately the muon charge ratio for single and for multiple muon events. This allows to select different energy regions of the primary cosmic ray spectrum and to test the R_μ dependence on the primary composition.

Chapter 2

The OPERA experiment

OPERA is a long baseline neutrino experiment aiming at the observation of direct ν_τ appearance in a pure ν_μ beam [26, 27, 28]. This would represent the final and unambiguous proof of the $\nu_\mu \leftrightarrow \nu_\tau$ oscillation as it has been interpreted in the atmospheric sector by disappearance experiments like Super-KamiokaNDE, MACRO and MINOS [29, 30, 31]. The direct appearance search is based on the detection of τ leptons produced in the charged current interactions (CC) of τ neutrinos. The neutrino beam is produced by the protons accelerated in the CERN SPS and injected in the CNGS[1] beam line, 730 km away from the detector location. The OPERA experiment is installed in Hall C of the underground Gran Sasso Laboratory (LNGS[2]), aligned with the CNGS baseline, under 1400 meters of rock overburden.

The experiment was designed to identify the tau lepton, characterized by a very short lifetime ($c\tau = 87\ \mu$m), according to its decay topology and kinematics. This requires a micrometric resolution and a mass of the order of a kton, to maximize the neutrino interaction probability. To accomplish these requirements, the detector concept is based on the Emulsion Cloud Chamber (ECC) technique, combined with real-time detection techniques (electronic detectors): OPERA is a hybrid apparatus with a modular structure, illustrated in Fig. 2.2. The ECC basic unit in OPERA is a *brick* made of 56 lead plates (absorbers), providing the necessary mass, interleaved with 57 nuclear emulsion films, providing the necessary spatial and angular resolution. The electronic detectors are used to trigger the neutrino interactions, to locate the brick in which the interaction took place, to identify muons and measure particle momentum and charge.

---

[1] **C**ERN **N**eutrinos to **G**ran **S**asso

[2] **L**aboratori **N**azionali del **G**ran **S**asso

2.1 The CNGS neutrino beam

The CNGS beam was designed and optimized for the ν_τ appearance starting from a pure ν_μ beam [32]. The high energy of the beam (the mean neutrino energy is $\sim$17 GeV), well above the threshold for τ production, was chosen to maximize the number of CC interactions at Gran Sasso of ν_τ produced by the oscillation mechanism. The average L/E_ν ratio is 43 km/GeV, that makes the ν_μ spectrum "off peak" with respect to the maximum oscillation probability for $\Delta m^2 = 2.4 \times 10^{-3}\text{eV}^2$ [33, 34]. This value results from a compromise between the requirements of a significant CC interaction cross section and a large oscillation probability.

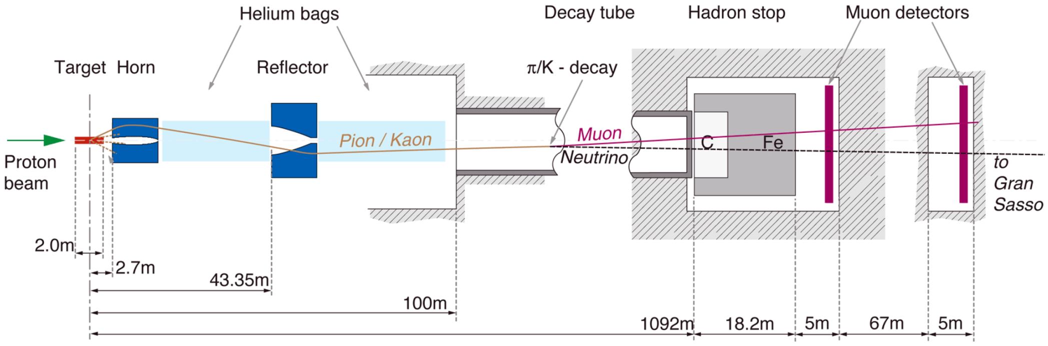

Figure 2.1: Schematic outline of the main components of the CNGS beam line [32].

A schematic layout of the CNGS facility at CERN is shown in Fig 2.1. The CNGS is a conventional neutrino beam: the 400 GeV/c proton beam extracted from the SPS accelerator hits a carbon target producing pions and kaons. The target unit contains 13 graphite rods with a diameter of 4 mm, well containing the proton beam, for an overall target length of 2 m. The positively charged π/K are energy-selected and guided with two focusing lenses, called "horn" and "reflector", in the direction of Gran Sasso. Each of these two toroidal lenses is 7 m long, and they are separated by a helium tube 31 m long, in order to reduce the interaction probability for secondary hadrons. Downstream of the reflector there is a second helium tube 41 m long, at the end of that starts the CNGS decay tunnel. The tunnel is 994 m long, with a diameter of 2.45 m, under vacuum at less than 1 mbar. Here the focused hadrons forming a parallel beam decay into ν_μ and μ^+ with an opening angle of $\sim$ 2 mrad. All the remaining hadrons, i.e. protons that have not interacted in the target, pions and kaons not decayed in flight, are absorbed by a massive iron and graphite hadron stopper at the end of the vacuum pipe. The muons, absorbed downstream in around 500 m of rock, are monitored by two muon detector stations. The first one is located immediately downstream of the hadron stopper, the second one after 67 m of rock. This allows the measurement of the intensity of the produced neutrino beam and the beam profile, giving an on-line feedback for the beam quality control. The separation of the two stations allows a rough estimation of the muon energy spectrum, since the energy threshold is different in the two chambers.

$\langle E_{\nu_\mu} \rangle$	17 (GeV)
$L/\langle E_{\nu_\mu} \rangle$	43 (km/GeV)
ν_μ	7.36×10^{-9} ($\mathrm{m}^{-2}\mathrm{pot}^{-1}$)
ν_e/ν_μ	0.89%
$\bar{\nu}_e/\nu_\mu$	0.06%
$\bar{\nu}_\mu/\nu_\mu$	2.1% (CC)
ν_τ/ν_μ	negligible
ν_μ CC	5.05×10^{-17} ($\mathrm{pot}^{-1}\mathrm{kton}^{-1}$)

Table 2.1: CNGS beam features and interactions expected in OPERA [32].

During a nominal cycle, there are two SPS extractions 10.5 μs long (pulses), separated by 50 ms, of 2.4×10^{13} protons each at 400 GeV/c. The CNGS beam features are given in Table 2.1: the $\bar{\nu}_\mu$ contamination is 2.1% in terms of CC interactions, the $(\nu_e + \bar{\nu}_e)$ contamination is lower than 1% and the prompt ν_τ contamination is totally negligible.

Due to the Earth curvature, neutrinos from CERN enter the Hall C with an angle of 3.3 °C with respect to the horizontal plane. The nominal integrated beam intensity is 4.5×10^{19} protons on target (p.o.t.) per year (200 operational days), designed to operate for 5 years. The number of corresponding CC and NC ν_μ interactions expected at Gran Sasso is about 3800/kton/year. Assuming $\Delta m^2 = 2.4 \times 10^{-3}\mathrm{eV}^2$ and maximal mixing, at the nominal beam intensity and with a target mass of 1.25 kton, 115 ν_τ CC interactions are expected after 5 years of data taking. Considering the overall efficiency to detect the τ, OPERA should observe about 10 signal events with less than one background event.

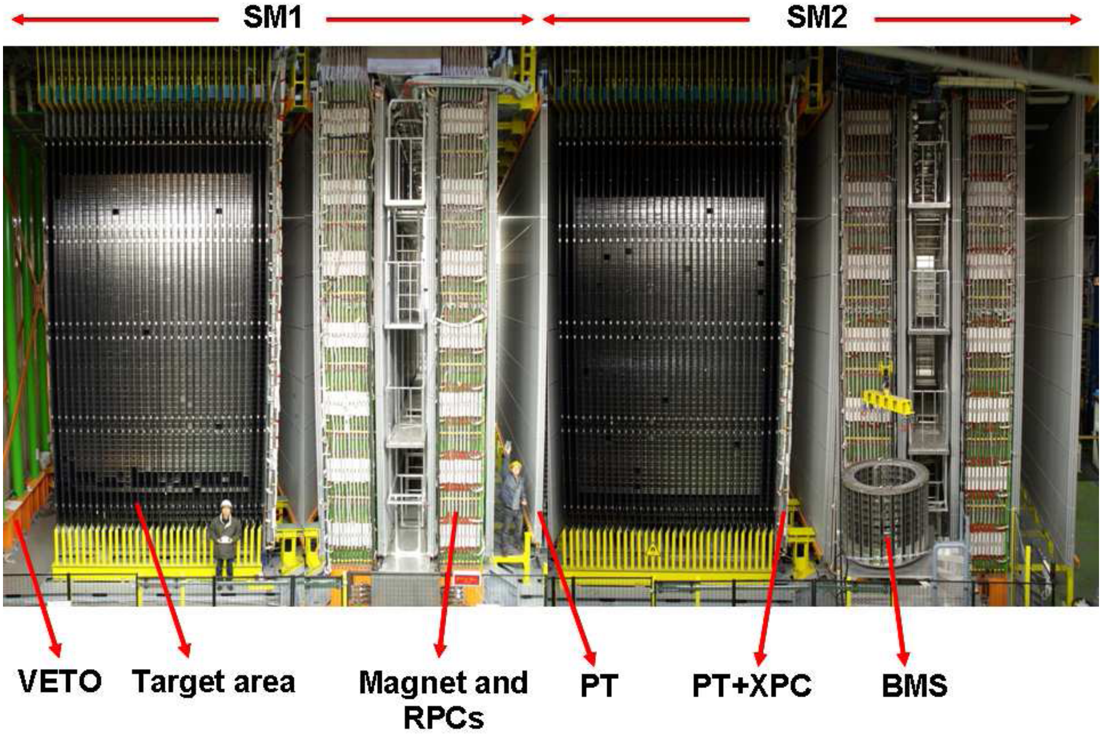

Figure 2.2: View of the OPERA detector [26]. The upper red horizontal lines indicate the position of the two identical supermodules (SM1 and SM2). Arrows show the position of the “target area” (ECC brick walls interleaved with planes of plastic scintillators), the VETO planes, the drift tubes (PT) surrounded by the XPC, the magnets and the RPC installed between the magnet iron slabs. The Brick Manipulator System (BMS) is also visible.

2.2 The OPERA detector

The detector is composed of two identical parts, called supermodules (SM1 and SM2), each consisting of a target section followed by a magnetic spectrometer. In the target, the bricks are arranged in 29 vertical planar structures (“walls”), transverse to the beam direction, interleaved with Target Tracker (TT) walls. Each TT wall consists of a double layered plane of long scintillator strips. The TTs trigger the data acquisition and locate the brick in which the interaction occurred. The target section is followed by a magnetic spectrometer, a large dipolar iron magnet instrumented with Resistive Plate Chambers (RPC). The magnetic field intensity is 1.53 T, directed along the vertical axis, transverse to the neutrino beam axis. The RPC planes are inserted between the iron slabs. They provide the tracking inside the magnet and the range measurement for stopping muons. The deflection of charged particles in the magnet is measured by six stations of vertical drift tubes, the Precision Trackers (PT). In order to remove ambiguities in the reconstruction of particle trajectories, each spectrometer is instrumented with additional RPCs with two crossed strip planes tilted with respect to the horizontal and vertical planes, called XPC. Two glass RPC layers (VETO) are placed in front of the detector, acting as a veto for charged particles originating from the upstream material (mainly muons from interactions in the rock or in the Borexino experiment).

The OPERA detector, shown in Fig. 2.2, has a length of 20 m (z coordinate), is 10 m high (y coordinate) and 10 m wide (x coordinate), for a total weight of about 4 kton.

Each sub-detector and its purpose will be described in more details in the following Sections.

2.2.1 Target

The target is based on the ECC technique, fulfilling the requirements of high granularity and micrometric resolution, necessary to distinguish the τ decay vertex from the primary ν_τ interaction. The excellent emulsion spatial ($\sim 1\ \mu$m) and angular ($\sim 2\ \mu$m) resolutions are ideal for detection of short-lived particles [35]. The use of passive material, combined with high accuracy tracking devices, allows for momentum measurement of charged particles via multiple Coulomb scattering (MCS), for electromagnetic shower and particle identification [36, 37]. Thus, the brick acts as a standalone detector, that can be selectively removed from the target, developed and analyzed after the interaction took place. The brick is made of 57 emulsion films (industrially produced by Fuji) interleaved with 56 lead plates, 1 mm thick. The transverse area is $128 \times 102\,\mathrm{mm}^2$, while the longitudinal size is 79 mm, corresponding to 10 X_0, for a total weight of 8.3 kg. In total, 150000 of such target units were assembled reaching the required overall mass of 1.25 kton.

Each emulsion film is made of two active layers 44 μm thick poured on a 210 μm plastic base. The nuclear emulsions consist of AgBr crystals suspended in a gelatin binder. The passage of charged particles creates perturbations at atomic scale (latent image), amplified by a chemical-physical process called development. The resulting grains of silver atoms of about 0.6 μm diameter are visible with an optical microscope. About 30 grains every 100 μm are left by a minimum ionizing particle. The lead

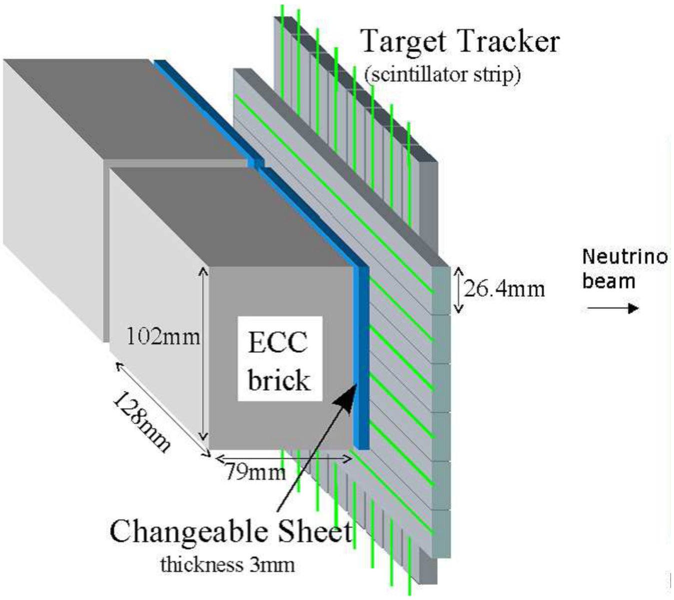

Figure 2.3: Schematic view of the brick with the Changeable Sheets (CS) in the target [26].

contains a low percentage of Calcium ($\sim 0.03\%$) to improve mechanical characteristics, without increasing surface radioactivity [38].

The brick is selected by the electronic on-line detectors, with an accuracy at the cm level. To validate the brick finding result and to facilitate the search of event tracks in the brick with a higher accuracy prediction, two interface emulsion films called Changeable Sheets (CS) are attached downstream of the brick in a separate plastic box [39] (Fig. 2.3). The CS doublet acts as a confirmation of the trigger provided by the Target Tracker. The brick is developed only if the prediction is confirmed, otherwise the CS is replaced and the brick is put back in the target. Fig. 2.4 shows a schematic view of a ν_τ charged current interaction with the decay of the τ lepton as it would appear in an OPERA brick, in the CS and in the scintillator strips (TT).

The bricks were produced by a dedicated fabrication line, the Brick Assembly Machine (BAM), located underground near the OPERA detector to shield emulsions from cosmic ray background. The bricks are mounted into a wall structure: an ultra-light stainless-steel matrix of 51×52 trays. Each target section in SM1 and SM2 consists of 29 filled brick walls ($\sim$75000 bricks/SM), for a mass of about 625 ton/SM. The bricks are moved in and out of the walls using an automated system called Brick Manipulator

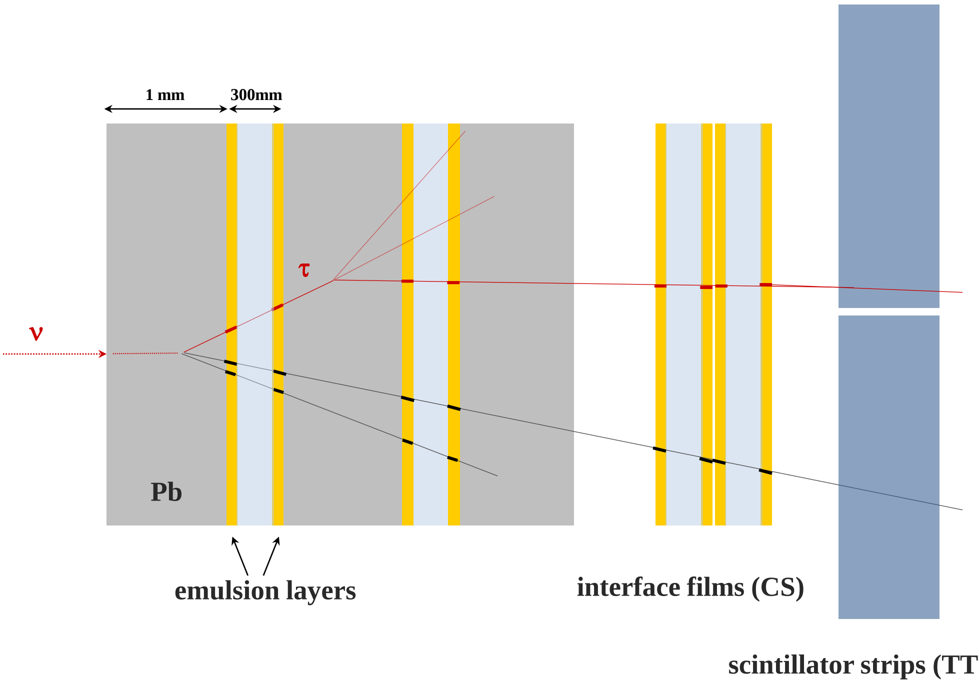

Figure 2.4: Schematic view of a ν_τ charged current interaction and the decay-in-flight of the final state τ lepton as it would appear in an OPERA brick, in the interface emulsion films (CS) and in the scintillator strips (TT) [26].

System (BMS). The BMS filled the target walls with the bricks produced by the BAM and extracts the bricks tagged by TT in real-time mode.

This modular and hybrid structure of the target allows to extract only the bricks actually hit by neutrinos, minimizing the ECC mass reduction during the run and achieving a quasi on-line analysis flow. In one day of data taking, about 20 neutrino interactions are recorded by OPERA and the related bricks are selected. A very fast automatized scanning system is needed to analyze this huge amount of emulsions. The task is accomplished by two different systems, the European one and the Japanese one, in ten laboratories.

2.2.2 Target Tracker

Each brick wall is followed by a Target Tracker (TT) wall [40]. The TT provides real-time detection of the outgoing charged particles, giving “time resolution” to the ECC.

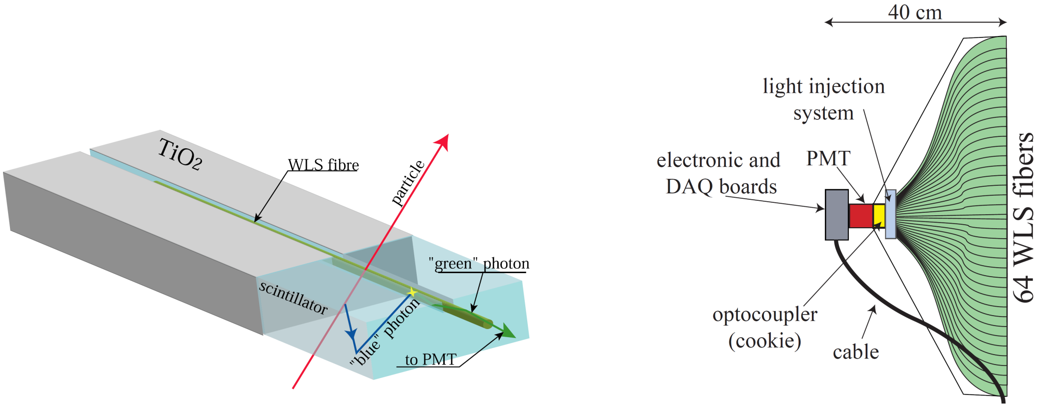

Figure 2.5: Schematic view of a scintillator strip with the WLS fiber (left) and of a strip module end-cap with the front-end electronics and DAQ board (right) [40].

Its main task is to locate the brick in which the neutrino interaction took place and to provide calorimetric measurement of the hadronic shower energy.

A TT wall consists of two scintillator planes, one providing the vertical and the other one providing the horizontal coordinates. Each plane is composed by 256 plastic scintillator strips 6.86 m long, thus covering the $6.7 \times 6.7\,\mathrm{m}^2$ surface defined by the brick wall, with a cross section of $2.63 \times 1.06\,\mathrm{cm}^2$. Along the strip, a 1 mm diameter Wavelength Shifting fiber (WLS) is read on both sides by a multi-anode photomultiplier (PMT), giving a position resolution of $\sim$1 cm (Fig. 2.5). The strips are grouped in four modules, each module is read out with a 64-channel Hamamatsu PMT; 16 PMTs per TT wall are used, as shown in Fig 2.6. With the chosen threshold, equivalent to 1/3 photo-electrons, the mean strip efficiency is higher than 99%.

2.2.3 Veto

Before reaching the OPERA target, CNGS neutrinos may interact in the rock, in the mechanical structures and in the Borexino detector, producing secondary particles able to induce false triggers. In order to reject these events, a VETO system is placed upstream of the detector. The VETO is made of two planes of glass Resistive Plate Chambers (GRPC) of $9.6 \times 9.2\,\mathrm{m}^2$, each one with 32 GRPC units. Each plane is equipped with horizontal and vertical copper strips with a pitch of 2.5 cm.

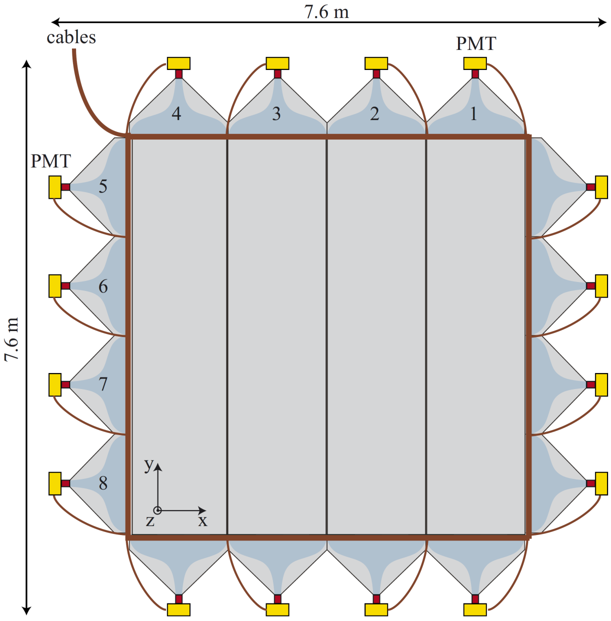

Figure 2.6: Schematic view of a TT wall, formed by one horizontal and one vertical plane. The scintillator strips are grouped in four modules in each plane [40].

2.2.4 Magnetic Muon Spectrometer

Magnet

Each of the two dipolar magnets is made of two vertical walls (arms), connected by a top and a bottom flux return yoke (Fig. 2.7). The walls consist of twelve iron layers 5 cm thick, interleaved with RPC planes (Inner Tracker). The geometry of the OPERA magnets has two advantages with respect e.g. to toroidal geometries. The magnetic field along the arms is much more uniform than in a toroid and it is essentially 1-dim., i.e. the components orthogonal to the vertical directions are nearly zero ($B \equiv |\mathbf{B}| \simeq B_y$) [41]. The magnets are operated at a current of 1600 A, the resulting magnetic field is essentially uniform with an average flux density of $\sim$1.53 T. The field lines are vertical and of opposite orientations in the two magnet arms, where B remains constant within 4%. The transverse size of the dipolar magnet is $10 \times 8.2\,\mathrm{m}^2$, the length is 2.64 m, for an overall weight of 990 ton.

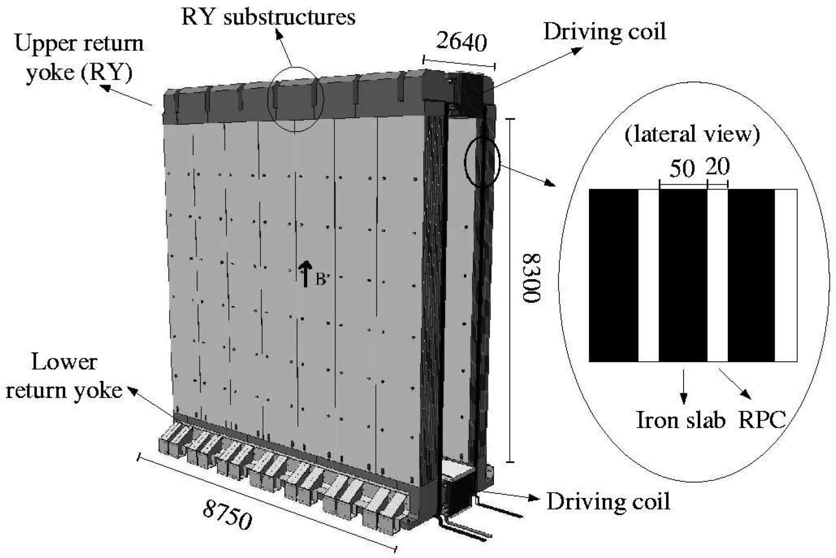

Figure 2.7: Three dimensional view of one OPERA magnet. Units are in mm. The blow-up insert shows the dimensions of three of the twelve layers of an arm [26].

RPC tracking system

Resistive Plate Chamber (RPC) planes are inserted in the 2 cm gaps between the iron slabs of the magnet arms (Inner Tracker), in order to reconstruct tracks inside the magnet and to give calorimetric measurements in combination with the TT [42]. The Inner Trackers are used also to measure the momentum from the range of stopping muons, and to provide the trigger for the Precision Trackers.

Each plane is composed of 3×7 RPCs of $2.91 \times 1.134\,\mathrm{m}^2$ surface covering a $70\,\mathrm{m}^2$ area. Each RPC consists of two electrodes, made of two parallel 2 mm thick bakelite planes kept 2 mm apart; the external surface of the electrodes is painted with graphite and protected with PET insulating films (Fig. 2.8). The 2-D read-out is performed by means of 2.6 cm pitch and 8 m long vertical strips (x coordinate), measuring the coordinate in the bending plane, and 3.5 cm pitch and 8.7 m long horizontal strips (y coordinate). The RPCs are operated in streamer mode at the voltage of 5.7 kV with a current of less than 100 $\mathrm{nA/m^2}$. Charged particles crossing the RPC ionize the gas mixture (based on Argon) producing ions and electrons that are drifted in the electric field to the corresponding plate and induce a signal in the copper strips. RPC layer's typical efficiency is about 95%. The time resolution is 4 ns, while the dead time is 10 ms, still suitable for the low event rate in OPERA. A dedicated trigger board allows

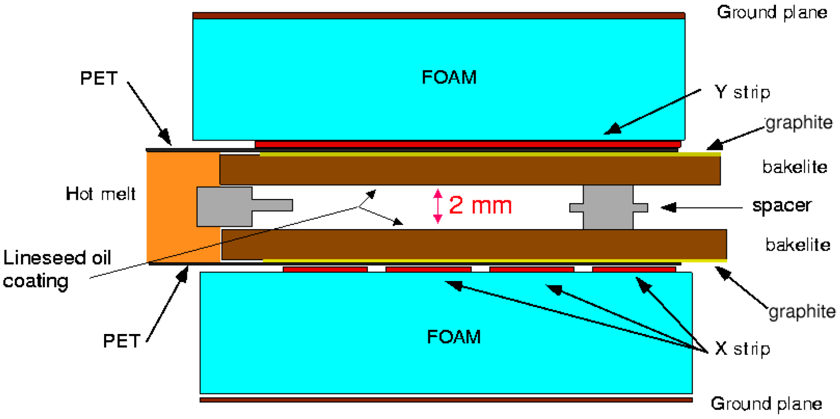

Figure 2.8: Cross-section of a Resistive Plate Chamber with its associated strips for the read-out of the induced signal [26].

for the definition of special triggering conditions between the 11 RPC planes of each spectrometer arm and an external validation signal.

The XPCs are two RPC planes placed outside the iron magnet, downstream of the target section, with the readout strips inclined by ±42.6 °C with respect to the horizontal. Both XPC planes are made of 21 RPCs with a pitch of 2.6 cm in each read-out direction. The XPCs help in resolving ambiguities in particle reconstruction inside the PTs and contribute with the RPC in the calorimetric measurement of hadronic showers.

In addition to the read-out electronics, the XPC and seven RPC layers in each spectrometer are instrumented with dedicated timing boards (TB) used to trigger the Precision Trackers and to give a common stop to their TDCs (Fig. 2.11).

Precision Tracker

The Precision Tracker (PT) is used together with the other parts of the muon spectrometer for muon identification, charge determination and momentum measurement [43]. Muons are deflected by the two magnet arms with opposite field direction, forming an S-shaped trajectory: only one track coordinate (x coordinate) has to be measured precisely. The PT measures the muon track coordinates in the bending plane with high precision. It is made of vertical drift tubes arranged in 12 chambers (PT stations), each covering an area $8 \times 8\,\mathrm{m}^2$. In each SM there are 6 PT stations grouped in 3 pairs. A

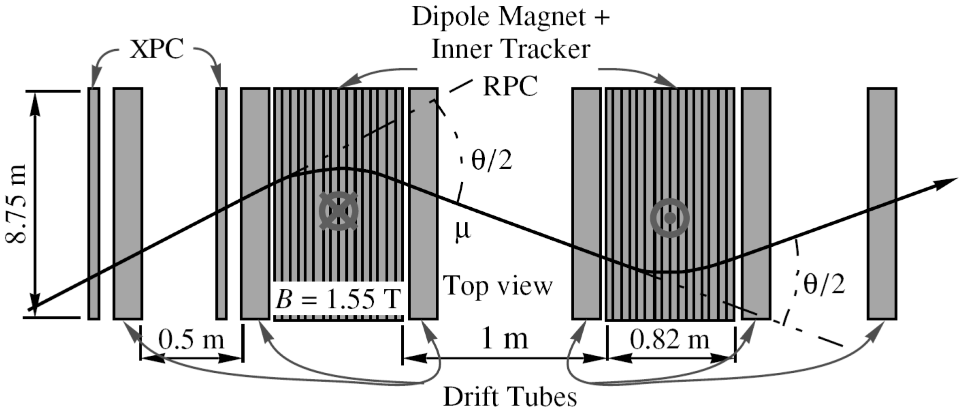

Figure 2.9: Top view of one muon spectrometer (x-z plane), showing the PT and the dipole magnet instrumented with RPC layers (2×11). The drift tube stations are grouped in 3 pairs per magnet arm.

first couple of consecutive PT stations is between the target section and the magnet, a second couple is in between the magnet arms and the third couple is downstream of the magnet (Fig. 2.9).

Each drift tube is 8 m long, with 38 mm outer diameter, 0.85 mm wall thickness and a gold-plated tungsten sense wire of 45 μm diameter. The tubes are filled with a 80% Argon and 20% CO_2 gas mixture, and the anode wire is tensioned at the operating voltage of 2.3 kV. Ionizing particles crossing the tube will produce electrons (ions) which will drift to the anode wire (cathode) with a well known drift velocity (few cm/μs for electrons), thus a radial measurement of the distance from the crossing particle to the wire is performed using the signal of the TDC board connected with each wire. The intrinsic drift time measurement error gives a spatial single tube resolution better than 300 μm (rms). The single tube hit efficiency η has been measured to be larger than 98%, while the single tube track efficiency, i.e. the product of η and the probability ϵ that the hit gives the correct drift radius, is 90% [43].

In order to reach high detection efficiency and good rejection of left-right ambiguities, a track must be measured by several adjacent detector layers. A Monte Carlo study [43] showed that 4 layers give enough redundancy and worked out the optimized staggering between the layers. The OPERA PT station is made of two double layers of 192 tubes, within each one the tubes are packed as closely as possible. The two double layers are shifted against each other by 11 mm (staggering). With this tube

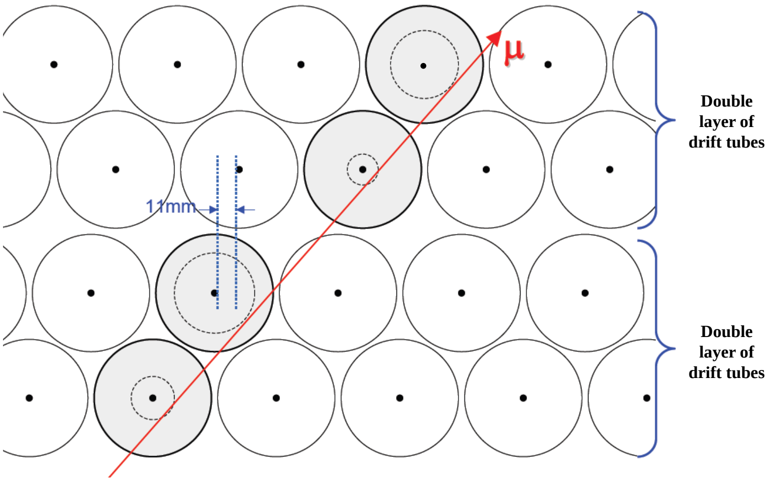

Figure 2.10: The PT station staggering between the two double layers of drift tubes.

arrangement, shown in Fig. 2.10, given the single tube track efficiency of 90% only the 1.5% of the tracks is lost.

Assuming a track measurement on 6 PT stations (track crossing the entire spectrometer), the momentum p of the particle is determined by the total deflection angle θ, the sum of the two deflections $\theta/2$ in each magnet arm (Fig. 2.9). Given the magnet geometry, the magnetic field intensity B and the PT coordinate measurement error, the momentum resolution is $\Delta p/p \leq 0.25$, with a charge misassignment probability of $\sim 1\%$ in the relevant CNGS momentum range [43]. For higher energies (relevant for cosmic ray studies) the performance on the momentum and charge reconstruction will be shown in details in Chapter 4.

The PT trigger system is fed by the RPC/XPC timing boards (Sec. 2.2.4) and has been optimized to collect both beam and cosmic ray muons with high efficiency. The trigger configuration is sensitive to through-going tracks, stopping muons and hadronic showers as well as to cosmic ray tracks. It also provides up-down discrimination from the measurement of the particle time-of-flight. Fig. 2.11 shows the overall trigger scheme for one spectrometer.

The trigger system is made of three identical stations (A, B, C), each managing the read-out of one pair of PT walls. The trigger stations are composed of three independent RPC/XPC planes. Each plane is equipped with timing boards and generates a fast OR signal sent to the corresponding trigger station. As shown in Fig. 2.11, the first PT

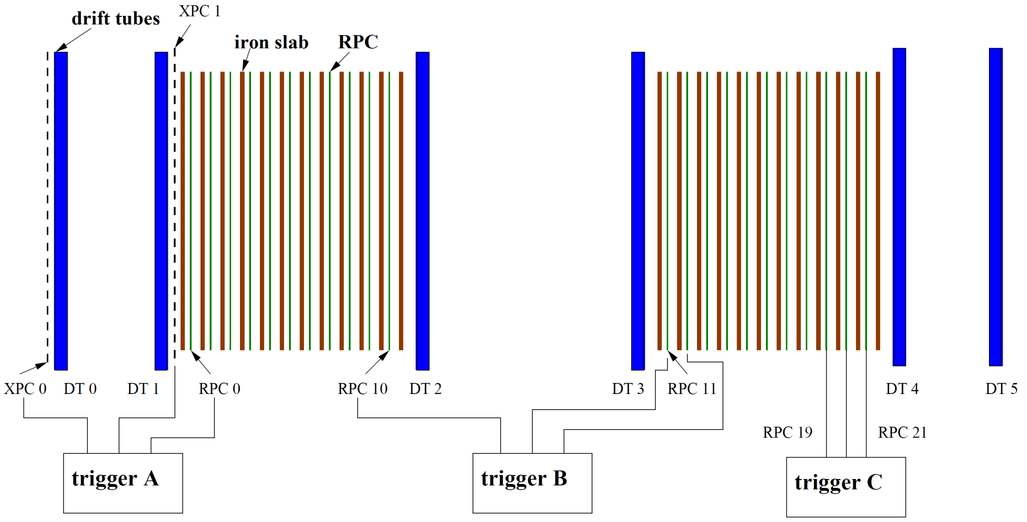

Figure 2.11: Overall trigger scheme for one spectrometer, seen from the top [26].

wall pair of each supermodule (DT0+DT1) is managed by a trigger station (Trigger A) fed by two XPC and one RPC planes. The other PT pairs, managed by Trigger B and Trigger C, receive signals from the closest RPCs. Each station is triggered if a majority of two out of three RPC/XPC planes occurs, with an average rate/station of $\sim$ 1.2 Hz. The optimal solution for both beam and cosmic events at the same time is to put in OR all the three stations of each spectrometer (second level trigger). In this configuration, if a station is triggered, the TDC stop signal is generated for all the PTs and the read-out chain for the corresponding PT data starts. The DAQ rate is at the level of 1.2×3 Hz.

2.3 The Data Acquisition System (DAQ)

Given the low event rate of the experiment (around 20 neutrino events per day), the OPERA data acquisition system [44] makes use of the Ethernet standards for the data transfer at the earlier stage of the read-out chain. The key element of the acquisition is the so-called "controller board" (also referred as sensor). Each sub-detector element is read out by an independent unit composed of a controller motherboard and an Ethernet controller mezzanine. Each sensor is externally seen as a client node on the Ethernet network. This scheme implies the distribution of a global clock mandatory to synchronize the local counters running on each controller board and to increment the acquisition cycle counters. The clock is synchronized with the GPS. A global scheme of the acquisition system is shown in Fig. 2.12. The main requirements to the DAQ system are triggerless operation mode, accurate timestamping locked to the GPS (to correlate off-line events with the CNGS), continuous running capability with low dead time, modular and flexible hardware/software architecture (trigger schemes, on-line and off-line filters, etc).

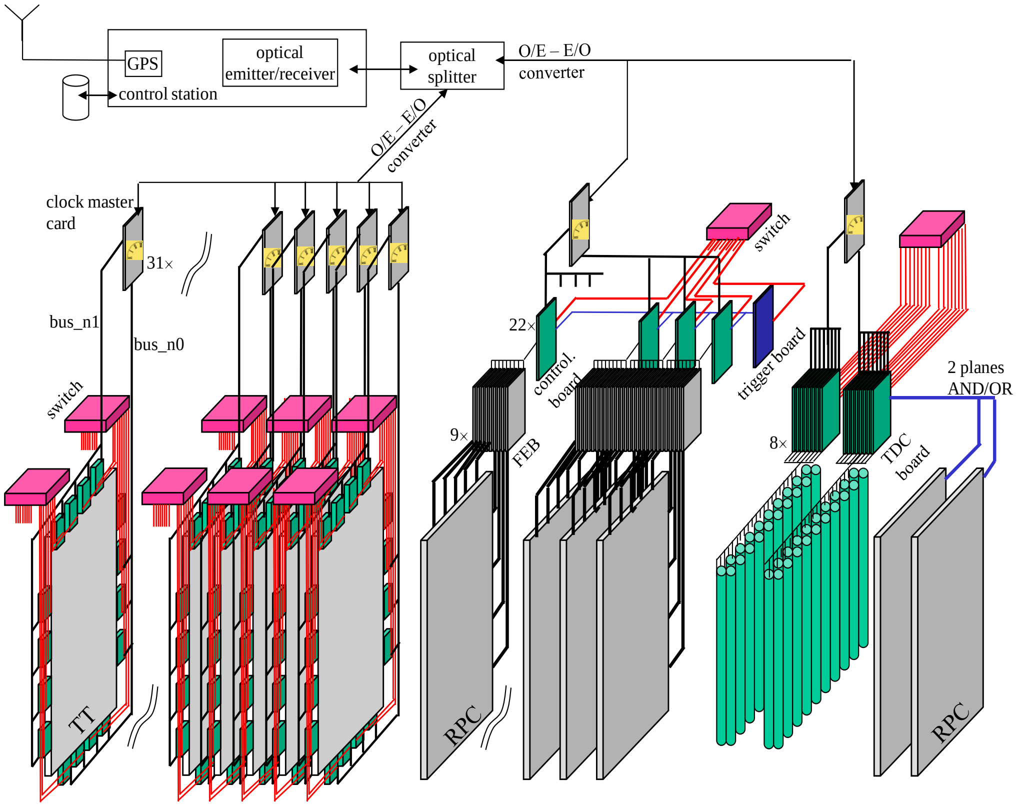

Figure 2.12: Schematic view of the DAQ system [44]. Each sensor (Controller Board) is connected into two different networks, the standard Ethernet network down to the event building workstation and the clock distribution network starting from a GPS control unit.

2.3.1 Global DAQ architecture

The DAQ starts from the controller boards (CB) of each sub-detector. Each of these sensors has an Ethernet controller mezzanine for the commands and the data transfer, a specific Front-End (F/E) controller, a clock unit that receives the global clock synchronized with the GPS and a power supply unit (Fig. 2.13).

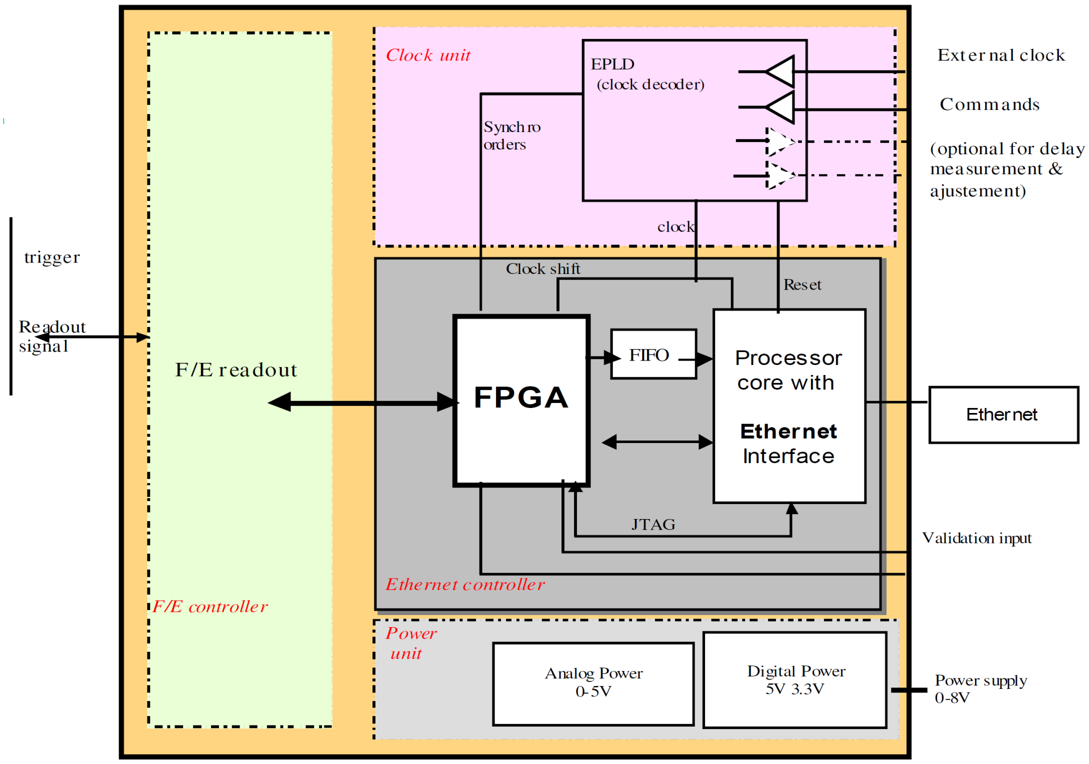

Figure 2.13: Generic controller board (CB) schematics. The CB is composed of an Ethernet controller mezzanine, a specific F/E controller, a clock unit and a power supply unit [26].

The central elements of the DAQ system are mezzanine boards hosting a microprocessor with an Ethernet interface, a sequencer (FPGA) and an external FIFO. The mezzanines are designed to give a common interface between each sub-detector specific front-end electronics and the overall DAQ system, to sort the data to the event builder, to handle monitoring and slow control from the Global Manager through Ethernet. The mezzanine is common to all sensors, while the F/E controllers are specific to each sub-detector: ADC boards for the PMT charge readout in the TT, TDC boards for the Precision Tracker and pattern readout boards for the RPCs. The clock unit receives the global clock and a command data distributed on each node by a “clock master card”. The global clock synchronize local fine time counters giving the precise timestamp to all triggers and is synchronized with the GPS.

The CB is connected into two different networks, sketched in the global scheme of Fig. 2.12. The first one is a standard Ethernet network in which the sensors are collected through a cascade of switches down to the event building workstation (consisting of commercial PCs); the second one is the clock distribution network starting from a GPS control unit.

The Ethernet network collect all the data from the different sub-detectors, send them to the event building workstation and dispatch the commands to the controller boards for configuration, monitoring and slow control. This structure allows to configure the DAQ and the event building by software to the larger extent, the only L0 triggers are defined in the hardware. The higher level triggers are defined by software at the event building workstation level.

The clock distribution system is a specific link between each sensor and the Central Clock unit synchronized on the GPS. A characteristic feature is the bi-directionality of the system which allows the control of the signal reception and the measurement of the propagation time with the acknowledge signals. The Central Clock unit decodes the GPS signal from the external antenna and sends a common clock from a precise oscillator via an optical link. The signal is then converted into electrical format and distributed to the "clock master cards" through M-LVDS bus. Each of these cards deserializes the commands and the clock, and distributes both of them to the clock unit of each controller board through another M-LVDS bus.

2.3.2 Event building

The global event building requires the collection through the Ethernet network of data coming out of all sub-detectors during one acquisition cycle, defined by the Central Clock unit. Each acquisition cycle is timestamped in coincidence with the GPS and recorded on a database in the form of a UTC (Universal Time Coordinated). The incrementation from cycle N to cycle N+1 is forwarded by the clock distribution line to all the nodes, where the propagation delay is corrected by the FPGA. All the nodes begin their new acquisition cycle at the same absolute time with a global accuracy of 10 ns. Each trigger recorded by a sensor (L0 trigger) is timestamped by latching the value of the local fast counter at 100 MHz. The absolute time of an event is reconstructed by $T_{event} = T_{UTC} + T_{fastcounter}$.

The higher level triggers are executed by software (standard C/C++ programs). All hits (L0 triggers) recorded during one acquisition cycle are sent by the sensors to the sub-detector corresponding event builder (1 per each SM for the TT, the RPC and the

PT, and 1 for VETO) which performs a time sorting, searches for coincidences within a sliding and adjustable gate, applies L1 filters and buffers the data before transmission to the Global Manager. With an overview of all detectors, the Manager performs the overall event building after L2 filtering and records the events.

2.3.3 UTC time synchronization

The events recorded by the OPERA DAQ are correlated off-line with the CNGS beam by comparing their coordinated universal time (UTC timestamp) with the one of the proton extraction from the SPS. The UTC time of each proton extraction is recorded in the CNGS database and is accessed by the OPERA off-line software.

In the external laboratory of LNGS a double ESAT19 GPS system disciplined with Rubidium oscillators provides the UTC timing signal to all the underground experiments. The LNGS timing signal is sent every ms through a system of optical fibers to the underground experiments. OPERA developed a customized slave clock based on a high stability quartz oscillator, which is completely compatible with the LNGS timing format and it is used to dispatch the timing to all the DAQ nodes of the experiment with a 10 ns period.

Taking into account all the calibrations, the time synchronization accuracy between the CERN beam GPS tagging and the OPERA timing system is about 100 ns. This accuracy is largely sufficient to correlate the events with the beam. As mentioned in Sec. 2.1, the CNGS timing structure is such that, for each CNGS cycle, protons are extracted from the SPS in two spills lasting 10.5 μs each and separated by 50 ms. The off-line program correlating the events with the beam subtracts from the OPERA UTC timestamps all the delays due to the particle time-of-flight and the calibration of the various components of the chain and selects events where the difference between the OPERA and CNGS timestamps is within a window of 20 μs.

2.4 Operation flow during the data taking

When the DAQ system triggers events contained in the CNGS time window (so-called “on-time” events), the electronic detector digits are used by the Brick Finding (BF) algorithm to indicate the candidate brick. The track digits are fitted by a linear and by a Kalman filter, and the BF provides a probability map on the brick walls, selecting the first three candidate bricks. The most probable brick is extracted by the BMS and the CS is detached and developed underground. The CS emulsion doublet is then scanned and analyzed. This step is a fast validation feedback of the BF result and allows to improve the prediction from the cm range of the TT to the sub-mm range in the CS. In case of a negative result from the CS analysis, the brick is equipped with a new CS box and sent back to the detector. A second brick is then extracted according to the probability map, if needed also a third one. If the event is confirmed in the CS by means of tracks that match the electronic detector signal, the brick is transported to the external lab and stored for 12 hours in a cosmic ray pit to accumulate high energetic cosmic ray tracks for alignment. The brick is finally developed and sent to one of the various scanning laboratories in Europe and Japan. The CS is not exposed to cosmic rays, thus the third function of the CS is to act as a veto for tracks found in the brick.

The bricks extracted are not replaced by new bricks; in five years of data taking, with the nominal event rate, the OPERA detector target mass will be reduced by a 20% factor.

Chapter 3

Monte Carlo simulation

The Monte Carlo simulation is a fundamental tool in underground muon physics, where many measurements are of indirect nature. Most of the observables depend on physics input not completely known. The energy of the primary "beam" is not fixed and some of the hadronic collision properties are not available in the fragmentation region above a few TeVs. Given the large number of coupled degrees of freedom, the Monte Carlo prediction is essential to disentangle some particular dependencies.

The code package treating the cascade development, the so-called *shower propagation code*, can implement different hadronic interaction models, referred as *event generators*. Currently one of the most used shower propagation code is CORSIKA [45], a general-purpose Monte Carlo code created by the KASKADE group. The event generators are sub-packages that can be easily inserted in an existing shower simulation program. The software interface allows the implementation without altering the general structure of the shower propagation code. The use of a single air shower code with different hadronic interaction models allows mutual comparison between the models.

The full Monte Carlo chain, necessary for the cross-check between experimental and simulated data, consists of several steps. It requires a detailed simulation of all physical processes occurring during the shower development and requires a correct treatment of energy losses and stochastic processes of TeV muons in the rock overburden. Finally, a detector simulation is needed to reproduce Monte Carlo data in the same format of experimental data. In the following Sections, the Monte Carlo simulations used for the analysis presented in this thesis will be examined.

3.1 Theoretical framework

High energy hadronic interactions are dominated by the inelastic cross section with the production of a large number of particles (multiparticle production). Most events consist of particles with small transverse momentum p_t with respect to the collision axis (*soft* production), while a small fraction of events results in central collisions between elementary constituents and produce particles at large p_t (*hard* production). QCD is able to compute the properties of hard interactions. Here the momentum transfer between the constituents is large enough (and the running coupling constant is small enough) to apply the ordinary perturbative theory. On the other hand, soft multiparticle production is characterized by small momentum transfer and one is forced to build models and adopt alternative non-perturbative approaches. Several models have been developed during the years: here we remind the Dual Parton Model (DPM) [55], developed at Orsay in 1979, and the Quark Gluon String model (QGS) [56], developed at ITEP (Moscow) during the same years. These two models, equivalent in many aspects, incorporate partonic ideas and QCD concepts (as the confinement) into an unitarization scheme to include hard and soft components into the same framework. The lack of a detailed theoretical description of soft hadronic physics is coupled with the lack of experimental data for these processes. The knowledge of the properties of high energy hadronic interactions mainly derives from experiments at accelerators or colliders. Here best studied is the central rapidity region ($|\eta| < 2.5$), populated by particles hard scattered in the collisions. In the (target or projectile) fragmentation regions particles produced at small angles escape into the beam pipe and hence they are not observed. The point is that, for the development of a cosmic ray shower, particles produced in the fragmentation region are the most important since they are the ones that carry the energy down the atmosphere and produce the "bulk" of secondary cosmic rays observed at the surface. In fact, most of the primary collisions are peripherals, with large impact parameters and consequently small momentum transfer. It seems clear that the modeling of high energy hadronic interactions for cosmic ray studies has to deal with different problems:

- In cosmic ray interactions, part of the center-of-mass energy for hadron-hadron collisions extends above the actual possibilities of collider machines. Most recent experimental data extends up to $\sqrt{s} = 7$ TeV at the LHC [57, 58]. Thus one is forced to extrapolate these measurements into regions not yet covered by collider data. The kinematic regions of interest for cosmic ray physics (and underground muon physics) is the one of projectile fragmentation (Sec. 1.2.1); here data from colliders extends up $\eta \sim 5$ (at $\sqrt{s} = 0.9$ TeV [16]). Very important will be the outcome of the TOTEM and LHCf experiments designed to study the particle production in the fragmentation region at high energies [46, 47].

- Part of cosmic ray collisions in atmosphere are nucleus-nucleus collisions. In this case, the data from fixed target experiments extends only up to few GeV/nucleus is the laboratory frame.

We understand now why interaction models constitute a major contribution to systematic uncertainties in cosmic ray physics.

A general feature of high energy hadronic interactions is the rise with the center-of-mass energy $\sqrt{s}$ of many of the exclusive and inclusive variables which characterize these reactions. The average global transverse momentum $\langle p_t \rangle$ grows logarithmically with the energy, from $\langle p_t \rangle = 350$ MeV/c at $\sqrt{s} = 63$ GeV (ISR) to $\langle p_t \rangle = 500$ MeV/c at $\sqrt{s} = 1.8$ TeV (Tevatron).

3.2 Hadronic interaction models

During the last thirty years many event generators had been developed to describe and simulate high energy interactions and particle production. Some of these models focus mainly on the high and ultra-high energy regime, while others focus on the well explored low energy domain, in an effort to describe this regime more accurately, and some others attempt to cover the entire energy range. In general two models are being used, one that treats the low energy domain from about 0.1 GeV up to 100 GeV-10 TeV, and one that covers the region beyond. These models and the corresponding program packages were designed partly for Monte Carlo based air shower simulations but also for accelerator and collider data interpretation and predictions.

At the low energy end the information is taken from experimental data acquired in accelerator and in collider experiments. Going to the higher energies, a fundamental self-consistent theory of interactions and particle production is lacking, and thus a number of mathematical models had been developed over the years to describe these phenomena.

We can recognize two approaches in building hadronic interaction generators by anchoring predictions with experimental data:

- accelerator data can be used to tune and check generators built on the basis of physically inspired models (as DPM or QGS). These generators contain a detailed description of the interaction processes, starting from elementary collisions between partons inside the projectile and target. The requirement is that these generators must reproduce the properties of hadronic interactions in kinematic regions where data already exist.

- an alternative (and less realistic) approach is to build a generator directly from the parameterizations of the most important features of hadronic interactions, extrapolating them in kinematic regions not yet explored, well beyond collider capabilities. Most of the properties of the interactions at low energy (where data exist) are obtained "by construction". This treatment of the hadronic interactions is approximate since the extrapolation to higher energies is subject to large uncertainties and many of the correlations existing between final state particles may be lost.

The second category is represented by the so-called *phenomenological models*, developed after the observation of the relevant properties of high energy collisions in early accelerator experiments ($E \leq 30$ GeV). In these models, the physics variables are sampled from distributions tuned to reproduce the ones measured at accelerators.

An example of this kind of models is HDPM [60], a phenomenological generator inspired by the Dual Parton Model inserted into CORSIKA as the default generator. HDPM is based on detailed parameterizations of *pp* collider data for particle production. It is adapted to handle hadron-nucleus interaction and energies well beyond collider capabilities. The underlain physical picture of this generator is the formation and subsequent fragmentation of two colour strings stretched between projectile and target valence quarks. The fragmentation and hadronization processes occur around the two jets along the primary quark directions. The generator do not use any hadronization model for the production of final states particles but simply parameterizes the particle production in each one of the two opposite jets on the basis of collider results.

In the following Section, a model belonging to the first category is presented.

3.2.1 QCD inspired models

Several of the modern high energy interaction and particle production models or event generators are quite similar. They are based on the same physical assumptions, the Gribov-Regge theory [61] and the exchange of *pomerons*. A pomeron is a hypothetical exchange particle, which in its mathematical definition is the pole of a partial wave in scattering processes.

They treat soft interactions by the exchange of one or several pomerons, handle elastic scattering alike but differ in the treatment of inelastic processes. The latter are handled by cutting pomerons, thus producing two color strings per pomeron which subsequently fragment into color-neutral hadrons. Nucleus-nucleus collisions are treated by tracking the participating partons in the projectile as well as in the target particle. The parameters and distributions (amplitudes) used in the different models are chosen such that they describe well the accessible accelerator and collider data to the highest energies and give good fits to the experimental results. Beyond they are used as extrapolations with corresponding uncertainties.

Two generators based on the two introduced interaction models are DPMJET, based on the DPM model, and QGSJET, based on the QGS model. One of the underlying common constituents of these models is the topological expansion of QCD. As suggested by t'Hooft and Veneziano, soft QCD phenomena can be quantitatively described considering a "generalized" QCD with a large number of colours N_c and flavours N_f such that $N_c/N_f = \text{const}$. The quantity $g_s^2 N_c$ plays the rule of an effective running coupling constant. This trick allows to compute the diagram contribution to soft processes in the limit $N_c \to \infty$, and then going back to $N_c = 3$ for physical applications. The interesting feature of this approach is that higher order diagrams with complicated topologies are suppressed in the cross section computation by $1/N_c^2$. Each diagram involves multiple exchanges of pomerons in the t-channel. The pomeron is treated as a quasi-particle with the vacuum quantum numbers and can be seen as a mathematical realizations of the colour and gluon field stretched between the interacting partons. The dominant contribution to the elastic scattering is a single pomeron, which has the topology of a cylinder. The correct prescriptions for the computation of the weights of each diagrams of the topological expansion is obtained considering that there is a one-to-one correspondence between these graphs and those in Reggeon Field Theory (RFT). This theory, proposed by Gribov [61], allows to evaluate diagrams involving several *reggeons* and pomerons, which in this theory are quasi-particles which mediate the soft scattering phenomena. Each physical particle belongs to a Regge "trajectory" in the angular momentum-mass plane, of the form

$$\alpha_k(m_l^2) = \alpha_k(0) + \alpha_k^{'}(0) m_l^2 = l \tag{3.1}$$

where the resonance masses m_l corresponds to integer values of l, the total angular momentum. The pomeron corresponds to the Regge trajectory with the maximum intercept $\alpha(t = 0)$. The computations of the relative contribution of each graph to the total discontinuity in the l complex plane is performed by means the so called Abramovski-Gribov-Kancheli (AGK) rules. These rules provide the prescriptions to evaluate the discontinuity of a graph "cutting" the pomerons. Each "cut" pomeron gives rise to a pair of string stretched between valence and sea quark of the interacting particles. This operation allows to compute the discontinuity of a graph for $t = 0$, and hence the total cross section according to the optical theorem.

The resulting soft total cross section is of the form

$$\sigma_{soft} = g^2 s^{\alpha(0)-1} \tag{3.2}$$

where g is the effective nucleon-pomeron coupling constant. From the choice of the intercept $\alpha(0)$ depends the high energy regimes of the models. An intercept $\alpha(0)$ exactly equal to 1 (*critical* pomeron) predicts a rising cross section with the energy only due the the minijet component. On the contrary, intercepts $\alpha(0) > 1$ predicts a soft component still present at high energies.

The input cross section for semi-hard production (minijets) is directly provided by the QCD improved parton model

$$\sigma_{hard} = \sum_{i,j} \int_0^1 dx_1 \int_0^1 dx_2 \int dt \frac{1}{1+\delta_{ij}} \frac{d\sigma^{ij}_{QCD}}{dt} f_i(x_1, q^2) f_j(x_2, q^2) \Theta(p_t - p_t^{thr}) \tag{3.3}$$

where the sum runs over all the flavours and $f(x, q^2)$ are the parton distribution functions (PDF).

The soft and hard components are different manifestation of the same process: the difference is that the hard component can be quantitatively computed by perturbative QCD. Therefore the choice of the “boundary” of the two regimes is very difficult to compute. Both the two processes (as well as the diffractive component) are treated together in these models in an unitarization scheme. Moreover, the value of the p_t^{thr} cut-off is chosen in such a way that at no energy and for no PDF the hard cross section is larger than the total cross section. This is to avoid unphysical rises of the minijet cross section over the total one.

The behaviour of PDFs at small values of x is crucial in high energy regimes, since it determines the contribution of the semi-hard component. After the results of the HERA experiment, we know that the singularities are of the type $1/\alpha$ with α between 1.35 and 1.5. At present, Monte Carlo generators uses different PDFs and this may lead to large discrepancies between the transverse structure of the final states, which are dominated by minijets at high energies.

DPMJET

DPMJET is a model to handle particle production in hadron-hadron, hadron-nucleus and nucleus-nucleus collisions [59].

DPMJET is based on the two component DPM (the hard and soft components). Soft processes are described by a supercritical pomeron which, in the version used in this thesis (DPMJET-II.4), has an intercept $\alpha(0) = 1.045$. For hard processes hard pomerons are introduced. High mass diffractive processes are described by triple pomeron exchanges, while the low mass diffractive component is modeled outside the DPM formalism. The fragmentation of the strings, generated by the cutted pomerons, is treated using the JETSET/PYTHIA Monte Carlo routines.

DPMJET contains a detailed description of nuclear interactions (the *direct* interaction mentioned above). The number of nucleon-nucleon interactions is evaluated from the Glauber formalism. The intra-nuclear cascade of secondary particles inside the nuclei is taken into account introducing the Formation Zone Intra-nuclear Cascade (FZIC) concept: a naive treatment of the cascade of created secondaries inside the nucleus may lead to overestimate the overall multiplicities of created secondaries. In fact, for high energy secondaries the relativistic time dilatation inside the target nucleus may result in the generation of secondaries when they are outside the nucleus, thus not contributing to the increasing of the multiplicity.

Moreover, the model takes into account the nuclear excitation energy, which are sampled from Fermi distributions at zero temperature, nuclear fragmentation and evaporation, high energy fission and break-up of light nuclei. DPMJET includes the production of mini-jets and charmed mesons, which can decay and generate prompt muons. DPMJET (from version II.3) uses the GRV-LO and CTEQ4 parton distributions; this allow the extension of the model up to energies $\sqrt{s} = 2000$ TeV.

FLUKA

FLUKA is a FORTRAN based Monte Carlo hadronic event generator, originally intended to describe inelastic interactions at laboratory energies up to several hundreds of GeV [48]. Different interaction sub-models are being used within this package to handle the collisions in the domain below, around and above the nuclear resonances. In recent years FLUKA had been generalized and can now be used to simulate hadronic and electromagnetic cascades.

FLUKA can handle the interaction and propagation in matter of about 60 different particles, among which photons and electrons from 1 keV to thousands of TeV, neutrinos, muons of any energy and hadrons of energies up to 20 TeV (up to 10 PeV by linking FLUKA with the DPMJET code) and all the corresponding antiparticles, neutrons down to thermal energies and heavy ions.

The hadronic interaction models are based on resonance production and decay below a few GeV, and on the Dual Parton Model above (see Sec. 3.1). For hadron-nucleus interactions at momenta below 3-5 GeV/c an Intra-Nuclear Cascade model (GINC) is used, while the high energy collisions are treated with the Gribov-Glauber multiple collision mechanism [15]. FLUKA can also simulate photonuclear interactions. Ion initiated nuclear interactions are treated through interfaces to external event generators. For neutrons with energy less than 20 MeV down to thermal energies FLUKA uses its own neutron cross section library, derived from recent data.

3.3 Cosmic ray event generation

Two conflicting requirements have to be fulfilled in the exploitation of Monte Carlo codes and event generators. On one hand, we need a reliable tool to control the data quality, to validate the analysis software, to evaluate the detector capabilities and unfolding. In this context, a fast simulation tool is needed. On the other hand, if we want to test theoretical hypotheses and eventually infer physical parameters, a full simulation taking into account all physical phenomena is needed. Thus, in this context, a shower propagation code should compute the first interaction point of primary cosmic rays on the basis of the input cross sections, describe collisions occurring in atmosphere using different models, propagate the electromagnetic and hadronic components of the shower considering the actual mean free path of particles. The complexity of the simulation requires long computing time: the statistics is strongly limited by the slow data processing.

We interfaced the official OPERA software with three atmospheric muon generators, each of them corresponding to different needs and to different levels of the analysis. The first one is a parameterized generator, the other two are full shower simulations. The generators' description and pertinence are presented in the following Sections.

3.3.1 Parameterized generator

A parameterized generator is a fast tool for the cross-check with experimental data. It is not predictive of physical behaviors, but it is very useful for data comparison, for the validation of the reconstruction chain and the evaluation of detector performance and resolutions.

The generator package developed for OPERA (*OpMult*) is embedded in the general software framework (*OpRelease*) that will be presented in Sec. 3.4: it is based on a parameterization implemented for the MACRO experiment [50], obtained from a previous full Monte Carlo simulation. OpMult generates multiple muon events directly at the level of Gran Sasso underground Hall C. It allows to choose the primary composition, i.e. the flux for each of the 5 components into which the primary spectrum is usually divided (H, He, CNO, Mg, Fe), among 7 different models. For the analysis here presented, a simulation using the MACRO fit model was produced [51]. Together with the chemical composition, some other parameters are asked as a input for the simulation: the muon charge ratio (here set $R_\mu = 1.4$), the transverse momentum distribution of muon parents and the minimum muon multiplicity into OPERA volume.

The algorithm philosophy is the following:

- each primary type and its energy are sampled according to the composition model;
- the arrival direction is randomly generated, and the corresponding amount of rock overburden is computed (from the Gran Sasso topographical map);
- given the primary type and energy, the direction and the rock, the probability to have N muons at underground level is extracted from tables obtained by a full Monte Carlo simulation, the same used to derive the primary composition model (in this way self-consistency is ensured);
- the residual energy for each muon is computed from a parameterized (phenomenological) function [63];
- the lateral dispersion of each muon with respect to the shower axis is again parameterized according to the full Monte Carlo simulation results; in this way, some correlations are lost (e.g. lateral dispersion versus number of underground muons).

A detailed Gran Sasso rock map $h(\vartheta, \varphi)$ (Fig. 3.1) has been derived from the elevation map over the underground Hall C, provided by the Italian geodetic institute (IGM) in DTM format (Fig. 3.2). The result of the algorithm is a list of muon events impinging on the underground OPERA volume, whose multiplicity follows probability distribution extracted from a detailed shower simulation.

The self-consistency on the predicted muon flux underground is ensured since the composition model and the probability tables were obtained using the same hadronic interaction model. This means that the systematic error on the primary composition and on the interaction model cancel and the Monte Carlo generator predicts the correct muon flux in the underground Laboratory.

In addition to the cross-check with the experimental data and to the validation of the analysis software, the parameterized generator is used to unfold the experimental data using the charge misidentification probability.

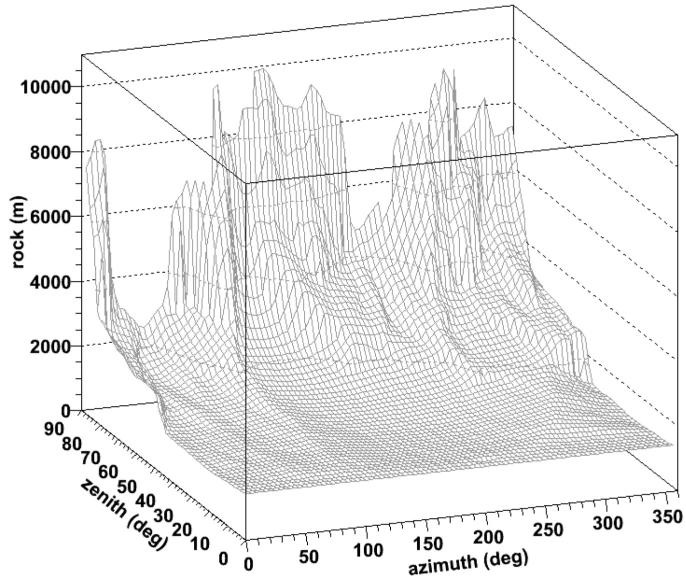

Figure 3.1: Gran Sasso rock map $h(\vartheta, \varphi)$, centered in the OPERA reference frame. The azimuth φ increases counter-clockwise from the $\varphi = 0°$ CNGS direction. The zenith ϑ increases from the vertical direction $\vartheta = 0°$ to the horizontal $\vartheta = 90°$.

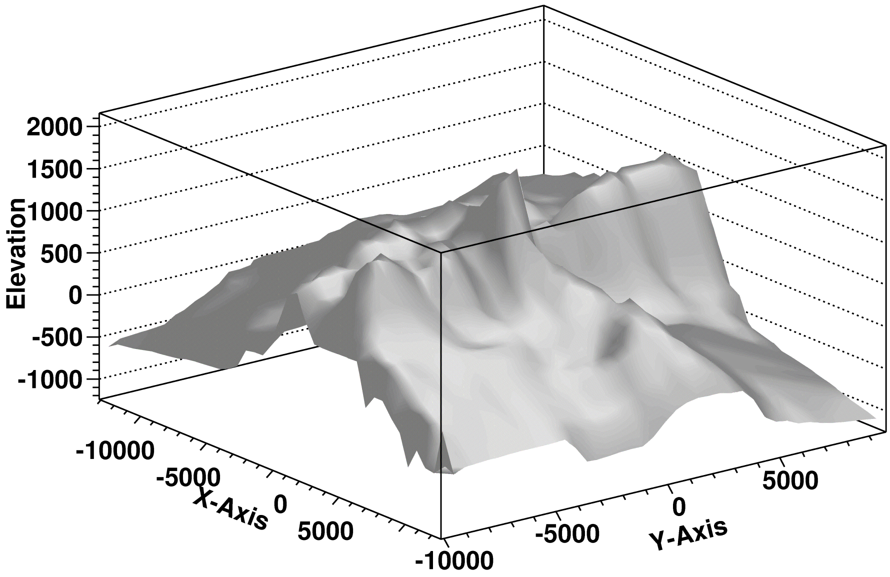

Figure 3.2: Gran Sasso elevation map, centered on the underground Hall C. The system origin $(0, 0, 0)$ is the OPERA reference system origin. All units are in meters.

3.3.2 FLUKA

FLUKA [48] is a general purpose tool for calculations of particle transport and interactions with matter, covering an extended range of applications. Different models are implemented for different energy regions, to ensure the maximum consistency, and results are checked against experimental data at single interaction level. Thus the results of complex cases, as well as properties and scaling laws, arise naturally from the underlying physical models and predictions are provided where no experimental data are directly available.

In recent years, a new package was developed in the FLUKA framework to simulate cosmic ray cascades [49]. The FLUKA shower propagation code can use the original FLUKA hadronic interaction model or independent models like DPMJET. Atmospheric profile and mountain overburden are accurately described by the detailed FLUKA geometry.

The production used for the analysis presented in this thesis is a full air shower simulation, in which the primary composition model refers to Ref. [62] and the hadronic interaction model is FLUKA. Since the flux is steeply falling with energy, the Monte Carlo production was segmented. To obtain as much statistics in the high energy region as in the low energy region, the bands with higher primary energy have longer live-times.

Fundamental parameters of the simulation are the threshold energies down to which the particles in the atmosphere must be followed: the CPU time required to follow particles of ever decreasing threshold energies quickly diverges. Since this work concerns the study of underground muons, the cut of $E_\mu^{min} = 1$ TeV in the atmosphere is set, since 1 TeV is the minimum muon energy on surface for surviving at Gran Sasso depth.

The FLUKA production is used for the surface muon energy estimation and to provide a link between the underground variables and the primary cosmic ray parameters. Fig. 3.3 shows the ratio of the parent energy over the primary energy (energy/nucleon) (x_F-like distribution) separately for pions and kaons. The mean values of the distributions are $\langle x \rangle_\pi = 0.208$ and $\langle x \rangle_K = 0.212$.

Fig. 3.4 shows the fraction of the primary energy (energy/nucleon) taken by muons, separately for single and multiple muons at the underground level (not only in the OPERA detector). The muon energy fraction is computed for proton primaries and for all primaries heavier than protons. The behaviour in the two composition cases is similar: the selection of high multiplicity events artificially bias the x_F distribution of muon parents towards smaller values. In Chapter 5 we will see how this reflects on the muon charge ratio R_μ.

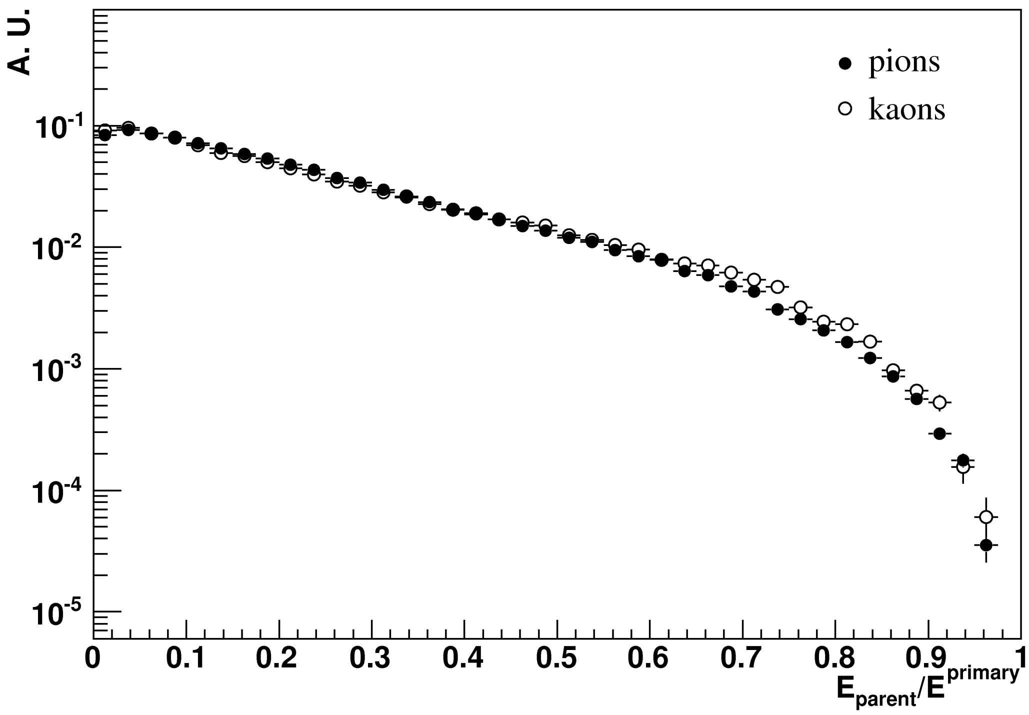

Figure 3.3: The ratio of the parent energy over the primary energy (energy/nucleon) separately for pions and kaons.

3.3.3 HEMAS

HEMAS[1] [52] was originally designed as a fast tool for the production and propagation of air showers. It allows the calculation of hadronic and muonic components of air showers above 500 GeV and electromagnetic shower size above 500 KeV. HEMAS implements a detailed shower simulation, in which the user can select two different interaction models: the native HEMAS model and DPMJET.

For the charge ratio analysis, we adapted a MACRO production (1999), valid up to the horizontal direction. The shower propagation code is the HEMAS-DPM version v0.7-2 [53], in which the DPMJET code for hadron-nucleus interactions is embedded into the general HEMAS structure [52]. Muon propagation through the rock was performed with the PROPMU package [63], based on FLUKA and interfaced with cosmic event generators.

For nuclei initiated showers ($A > 1$), the direct interaction option is used. Dif-

---

[1] **H**adronic, **E**lectromagnetic and **M**uonic components in **A**ir **S**howers

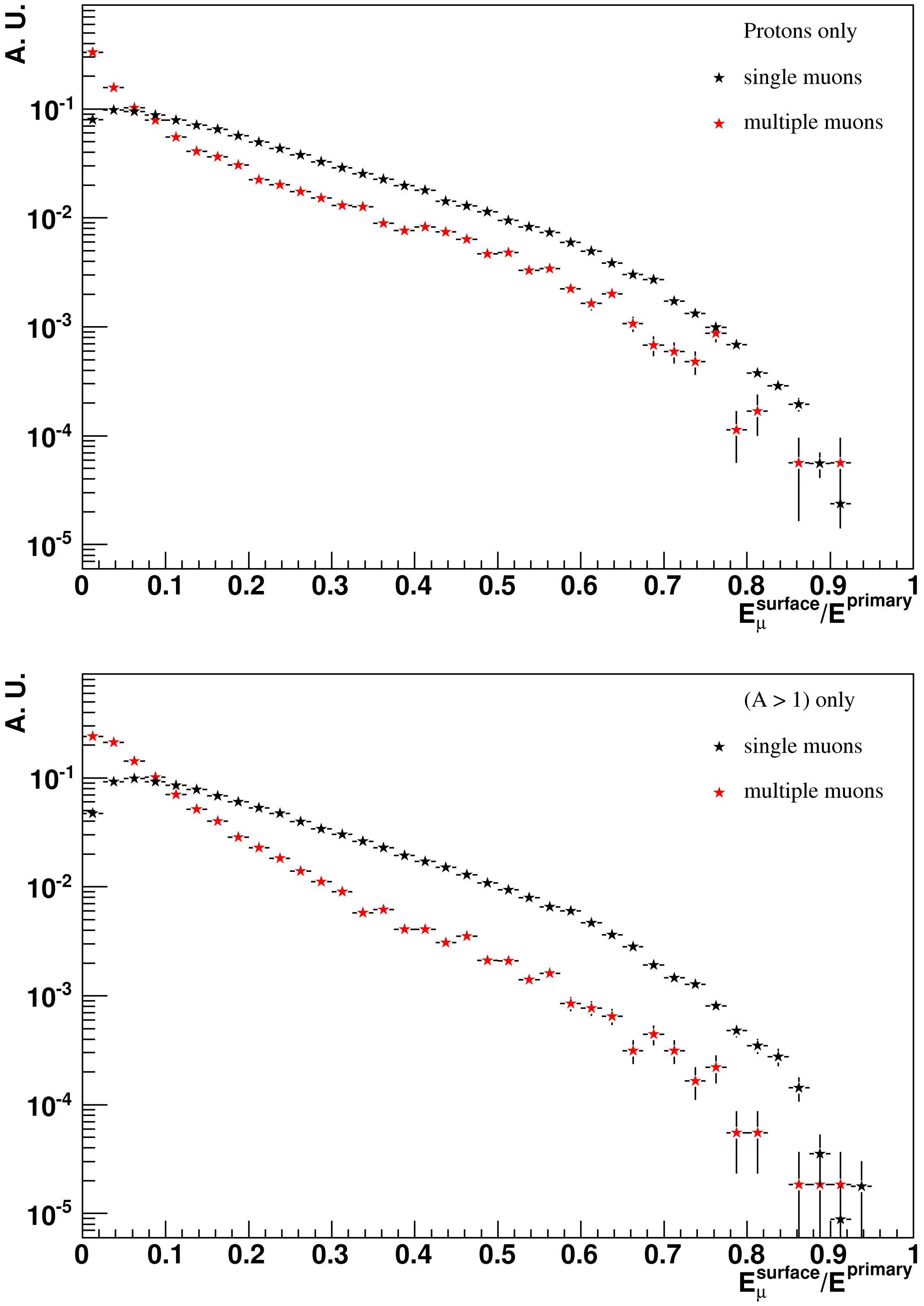

Figure 3.4: The fraction of the primary energy (energy/nucleon) taken by muons, separately for single and multiple muons at the underground Gran Sasso Laboratory level. The muon energy fraction is computed for proton primaries and for all primaries heavier than protons.

ferently from the simplified superposition model (Sec. 1.2.2), this option simulates the nuclear interaction without approximating it to a set of nucleon-nucleus interactions, but it takes into account all the nuclear processes involving a nucleus-nucleus interaction.

HEMAS neglects the muon energy loss in atmosphere, since this contribution is negligible for muons detected underground. In HEMAS the atmospheric profile can be chosen. Here we use a parameterization of the atmosphere at the Gran Sasso location in Central Italy.

At the beginning of the Monte Carlo chain, a composition model is set as a input; the MACRO fit model [51] was chosen for this simulation. The primary nuclei are divided in 5 mass groups ($A = 1, 4, 14, 24, 56$), for each elemental group the energy spectrum is parameterized as follows:

$$\phi_A(E) = K_1(A)E^{-\gamma_1(A)} \qquad \text{for} \quad E < E_{cut}(A) \tag{3.4}$$

$$\phi_A(E) = K_2(A)E^{-\gamma_2(A)} \qquad \text{for} \quad E > E_{cut}(A) \tag{3.5}$$

where the mass dependent parameter $E_{cut}(A)$ is the energy cut-off at the knee and $K_2 = K_1 E_{cut}^{\gamma_2-\gamma_1}$. The model parameters, reported in Tab. 3.1, satisfy the condition that $\sum \phi_A(E)$ gives the observed all particle spectrum of Eq. 1.2.

For the same reasons explained in the previous Section, the production for each mass group has been performed in six angular windows and five contiguous energy bands.

Mass Group	K_1 (m^{-2}s^{-1}sr^{-1}GeV$^{\gamma_1-1}$)	γ_1	$E_{cut}(GeV)$	γ_2
p	1.2 $\times 10^4$	2.67	2.2 $\times 10^5$	2.78
He	1.3 $\times 10^3$	2.47	4.4 $\times 10^5$	3.13
CNO	3.9 $\times 10^2$	2.42	1.5 $\times 10^6$	3.58
Mg	4.5 $\times 10^2$	2.48	2.6 $\times 10^6$	3.31
Fe	2.4 $\times 10^3$	2.67	5.6 $\times 10^6$	2.46

Table 3.1: Parameters of the composition model used for the simulation [51].

In each zenith angle window, extracted the event zenith and azimuth (ϑ, φ), the minimum rock depth h_{min} is computed from the Gran Sasso map. The rock determines the minimum energy threshold E_μ^{min}: a muon with energy E_μ^{min} has a probability $< 10^{-5}$ to survive reaching the depth h_{min}. The program then defines the threshold for the primary energy/nucleon, E_P^{min}, corresponding to twice the minimum muon energy.

The probability that a primary nucleus with energy/nucleon lower than E_P^{min} generates a muon with energy greater than E_μ^{min} is negligible.

The output of the described simulation chain consists in a list of events at the detector level distributed over an infinite area. Each one of these events has to be properly inserted ("folded") into the apparatus simulator in order to reproduce the detector effects. To maximize the generation efficiency and optimize the computing resources, the sampling procedure uses a variance reduction method developed in Ref. [64], based on the concept of "reciprocal geometry".

The HEMAS simulation was used to study the feasibility of the muon charge ratio measurement and to evaluate the OPERA physics potential [54]. It was used to build the analysis chain and to propose the optimal PT trigger condition implemented after this study, shown in the previous Chapter in Sec. 2.2.4. HEMAS is well suited for cosmic ray studies, however the hadronic interaction model is quite obsolete (1990) and not maintained anymore.

3.4 Detector simulation

The software framework of the OPERA experiment (OpRelease) is articulated in program packages, written in C++ code and based on ROOT[2] classes [66]. It is managed by the Concurrent Versions System (CVS[3]) and stored on the OPERA CVS repository at CERN. The OpRelease software has been built into the CMT[4] environment, the Configuration Management Tool, that handles system configuration, dependencies and compilation. OpRelease is a complete framework embodying geometry description (OpGeom), data format (OpRData) and external tools (OpMath and CMT interfaces to non-OPERA software package, like ROOT, CLHEP and others). Some event generators are packages as well: the beam neutrino interaction generator (OpNegn), the atmospheric neutrino generator (OpNuAtm), likewise the cosmic ray muon generator described in the previous Sec. 3.3.1, OpMult. HEMAS and FLUKA full generators are external to OpRelease, their output is converted into the same data format (OpRData) of the internal generators' output. The full simulation chain starts from this common point.

The OPERA detector simulation is included in this general structure and split in two packages, OpSim and OpDigit. OpSim reproduces the detector apparatus and the particle propagation inside it with the concurrent creation of track *hits* in the various

---

[2] http://root.cern.ch/

[3] http://cvs.web.cern.ch/cvs/

[4] http://www.cmtsite.org/

sub-detectors. OpSim is based on the ROOT Virtual Monte Carlo (VMC): a generalized Monte Carlo allows the user to choose the transport generator between GEANT 3.21[5] and Geant4[6]. A configuration file (datacard) can be modified by the user to setup data input/output and the real Monte Carlo used together with its options. Here the propagation cuts, the physics processes and the active volumes are defined.

For the analysis presented in this thesis, the GEANT 3.21 generator is used, asking the whole OPERA active volume, the magnetic field map mode in the spectrometers, and all the relevant physical processes like delta-ray production and catastrophic energy losses.

The output of OpSim feeds OpDigit: it applies the detector response to the hits left by the particles during the propagation, creating detector *digits*. At this level, each sub-detector efficiency is implemented in the Monte Carlo simulation. To make the TT detector description as much realistic as possible the cross-talk has also been included, i.e. the possibility that the signal deposited in one TT strip is recorded on the nearest-neighbour photomultiplier channels. The RPC simulation takes into account the different width of the horizontal and vertical sets of read-out strips, thus a slightly different efficiency is implemented. Nine RPC planes are also used to generate a fast trigger signal for the drift tubes (Sec. 2.2.4). For PT hits, the drift time is smeared according to a resolution function. The time information of the RPC trigger digits are used to generate a trigger time. The signal propagation delays of all the corresponding cables are considered for a realistic simulation of the trigger time delay. If no trigger is generated in a spectrometer, no drift tube data are saved.

The effect of the OPERA acceptance is visible in Fig. 3.5, where the angular distributions of muons impinging on Hall C and muons reconstructed in the OPERA detector are compared.

---

[5] http://wwwasd.web.cern.ch/wwwasd/geant/index.html

[6] http://geant4.web.cern.ch/geant4/

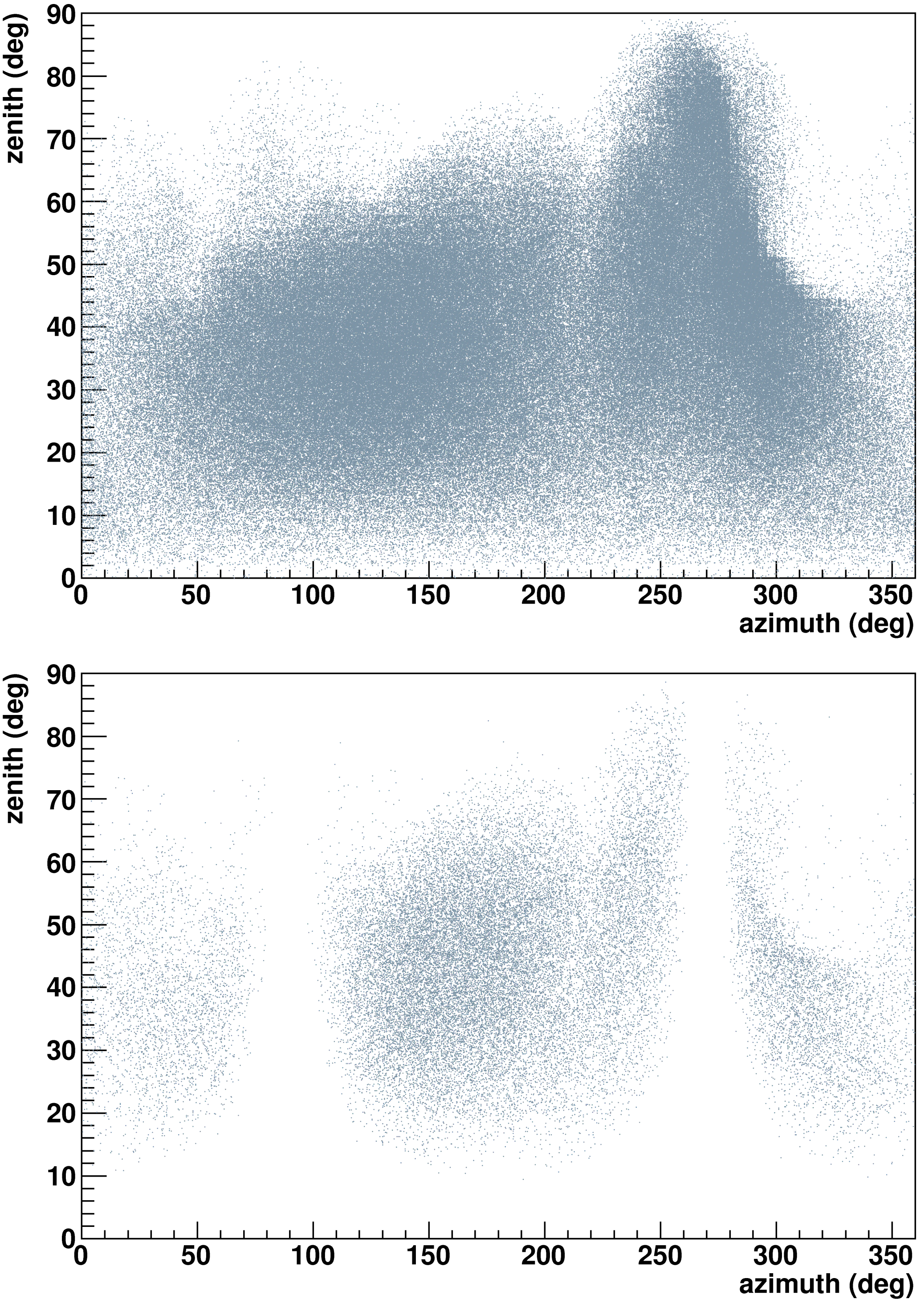

Figure 3.5: Angular distributions of muons impinging on Hall C (top) and muons reconstructed in the OPERA detector (bottom).

Chapter 4

Cosmic ray muons in OPERA

For the analysis presented in this thesis we exploited the OPERA capability as a cosmic ray detector. While the primary physics goal of the OPERA experiment is to observe neutrino oscillation, the large depth under the Gran Sasso rock overburden and the instrumented dipolar magnets allow it to sample high energy and charge-separated cosmic ray muons.

OPERA is a beam experiment and was optimized accordingly: structure, geometry, DAQ and triggers. The detector design depends on the physics objectives: OPERA has a modular structure along the horizontal beam direction. As we said in this thesis the detector was used differently from what it was conceived for; this is particularly true for the PT system which was configured to reconstruct and measure particles traveling along the CNGS direction. In general cosmic ray induced events impinge on the detector with large angles with respect to the CNGS direction. The OPERA geometry is not optimized for this event topology. The detector acceptance is reduced for vertical tracks, contrarily to what happens to experiments with an horizontal geometry.

Since the reconstruction software strategy is also modelled on the experiment design and physics goal, the beam event reconstruction code is optimized to follow a single long track (the muon escaping from the neutrino-interaction region) along the z-axis. The cosmic ray event topology is completely different: cosmic ray muons come from all the directions, they are not generated within the target and a fraction of them ($\sim 5\%$ in OPERA) is composed by muon bundles.

The OPERA standard software for beam event reconstruction was complemented with a set of dedicated software tools developed for cosmic ray events. Once the event is tagged as "off-beam", i.e. is not contained in the CNGS spill window (see Sec. 2.3.3), it is classified as *cosmic* and processed in a dedicated way.

In this Chapter the reconstruction of cosmic ray induced events is described.

4.1 Cosmic event reconstruction in the electronic detectors

The OPERA reference frame (Fig. 4.2) is defined to have the z-axis along the Hall C longitudinal direction (from north to south), y perpendicular to the floor pointing toward the zenith and x describing a right-handed frame. In this coordinate system, the zenith direction ϑ is defined by the angle with the y-axis, the azimuth direction φ by the angle with the z-axis, increasing counter-clockwise. Vertical direction corresponds to $\vartheta = 0$, while $\varphi = 0$ is the CNGS beam direction. Event reconstruction is performed separately in the two projected views T_{xz} and T_{yz}.

The reconstruction software is made of packages with specific tasks. The main algorithm steps are summarized according to their name in the code:

- CrossTalk: the package removes the cross-talk digits from the event digit list. TT digits due to adjacent-channel effects in the PMT matrix are subtracted according to a probability map.

- Alignment: the package, running only on experimental data, corrects the digit coordinates according to roto-translations between the OPERA reference frame and the actual positions of each sub-detector. Details are shown in Sec. 4.3.

- Pattern/CosmicPattern: the track finding strategy is selected according to the "on-time" flag, defined in Sec. 2.3.3. In case of beam events, the related pattern recognition based on a *cellular automaton* algorithm is executed. If the event is classified as "off-beam", i.e. as cosmic, it is processed by the CosmicPattern package. This is based on a hybrid strategy: a global method individuates at first the event direction, then a local method in the reduced feature space finalizes the pattern recognition.

- DTubeReco: a dedicated track finding and fitting inside the drift tube system is performed, guided by global track informations.

- Merging3D: the 2-D independent tracks in the T_{xz} and T_{yz} views are merged together to build a three dimensional event.

- Tracking: as the track finding, the track fitting is different for beam and cosmic events. For on-time events, a Kalman filter [67] is applied, while for high energy cosmic muons a simple linear fitting is executed.

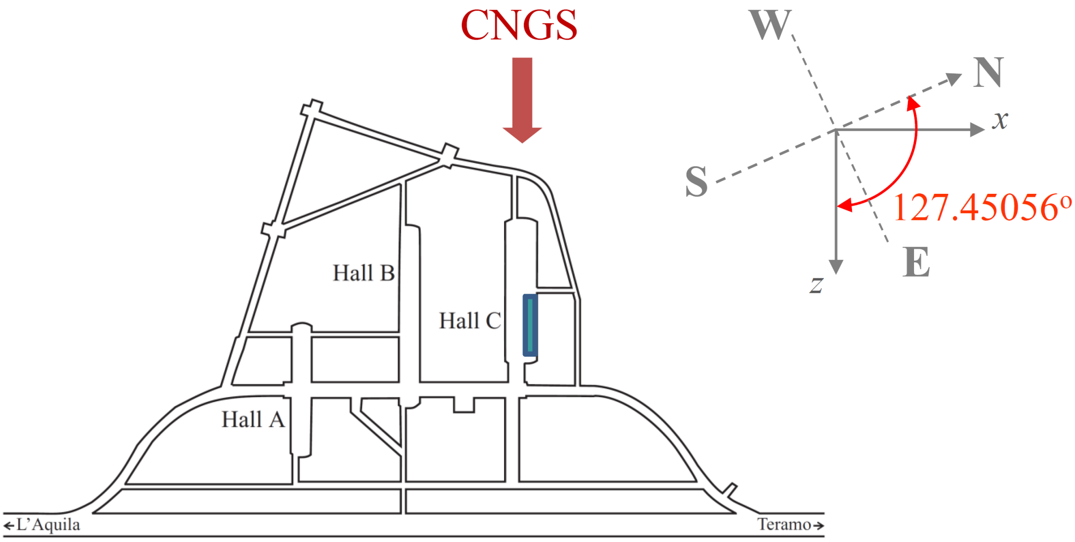

Figure 4.1: OPERA is installed in the Hall C of the underground Gran Sasso Laboratory. The CNGS beam direction and the detector orientation are shown.

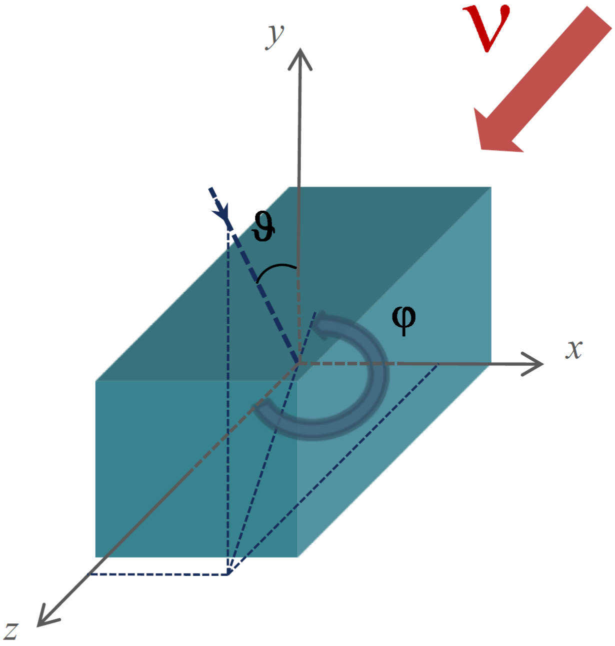

Figure 4.2: The OPERA detector orientation, with the definition of azimuth and zenith in the OPERA reference frame. The coordinate origin is at the center of the detector volume. The azimuth increases counter-clockwise from the CNGS direction ($\varphi = 0$).

In the following Sections, the steps forming the reconstruction chain are described in details.

4.1.1 Track finding

The algorithm philosophy is based on the a-priori knowledge of cosmic event topology, i.e. single tracks or bundle of almost parallel tracks passing through the whole apparatus. The pattern recognition is a combination of two strategies tailored on these characteristics: the bundle direction is individuated by a global method, the Hough transform, reducing by one degree of freedom the feature space. Then a local method, the pivot point technique, is applied on *slices* cut according to the event slope, keeping the combinatorial under control. This hybrid approach is optimized for multiple muon event reconstruction.

The Hough transform [68] is a feature extraction method used to find tracks in digitized images. It does not examine the granular structure of the events and is therefore insensitive to possible sub-detector inefficiencies and background noise digits.

The function of the Hough transform is to recognize a certain shape (in the OPERA case a line) in two-dimensional images finding clusters in the parameter space. For cosmic event reconstruction in OPERA, the linear transform is used to find straight tracks in the digitized detector readout, i.e. in each set of (x, z) and (y, z) event digit coordinates.

Hough transform identifies global patterns in the coordinate space (T_{xz} or T_{yz}) by using the identification of local patterns (ideally a point) in the transformed feature space. Since the conventional feature space (m, b) defined by the slope m and the intercept b is unbounded, it is preferable to choose a different pair of parameters, defined in Fig. 4.3. The parameter ρ is the minimum distance between the line and the coordinate origin while ψ is the angle between the distance vector and the z-axis. The parameterization of a straight line follows:

$$\rho = z \cos\psi + x \sin\psi \tag{4.1}$$

The (ρ, ψ) space is referred to as the Hough space.

Alternate planes of TTs or RPCs give either (x_i, z_i) or (y_i, z_i) coordinates, while the vertical PT digits give only the (x_i, z_i) coordinates. In each projected view T_{xz} and T_{yz} a Hough space is constructed transforming the detector digit coordinates into parameter curves. If the digit coordinates form a straight line, the curves in the Hough space cross at a particular value converging to a peak, as in Fig. 4.4. The peak values

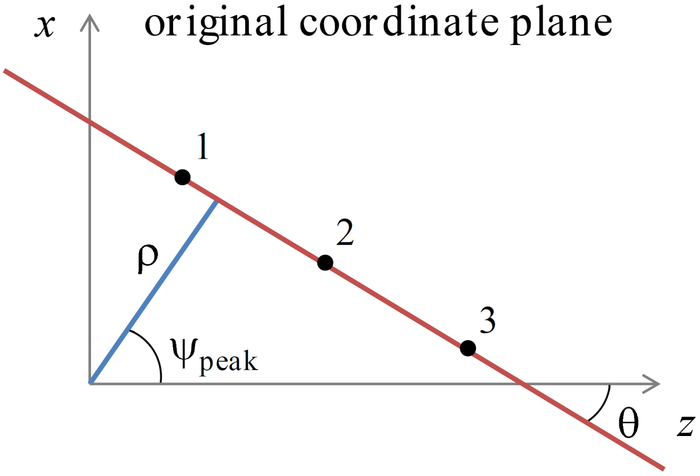

Figure 4.3: Definition of the parameters (ρ, ψ) in the pattern space.

$(\rho_{peak}, \psi_{peak})$ yield the track parameters. The signature of a 3-D straight track is the presence of a localized peak in both Hough spaces.

In case of single as well as of multi-muon bundles, the peak position in ψ is always well recognized, while for multiple or very noisy events the ρ information may be not reliable. Thus, the Hough transform is used to define the event direction, inverting Eq. 4.1:

$$\theta_{slice} = -\arctan(1/\tan\psi_{peak}) \tag{4.2}$$

where $m = \tan\theta_{slice}$ is the usual track slope (see Fig. 4.3). The direction information is used to subdivide the 2-D view in slices 25 cm wide having slant θ_{slice}. In each slice a local method based on interpolation is applied. The digits within the slice are processed separately to search for a track “seed” defined by a couple of external pivot points. If a seed is found, all the other digits in the corresponding projected view are linked to the selected track according to pre-defined tolerances. The eventual track candidate has $N \geq 4$ aligned digits.

The result of the track finding algorithm is a list of digits for each of the n_μ tracks contained in the event, where n_μ is the multiplicity in each projection plane. In the subsequent algorithms, presented in the following sections, the two event multiplicities in T_{xz} and T_{yz} are compared and the 2-D tracks are merged, in order to have a 3-D event

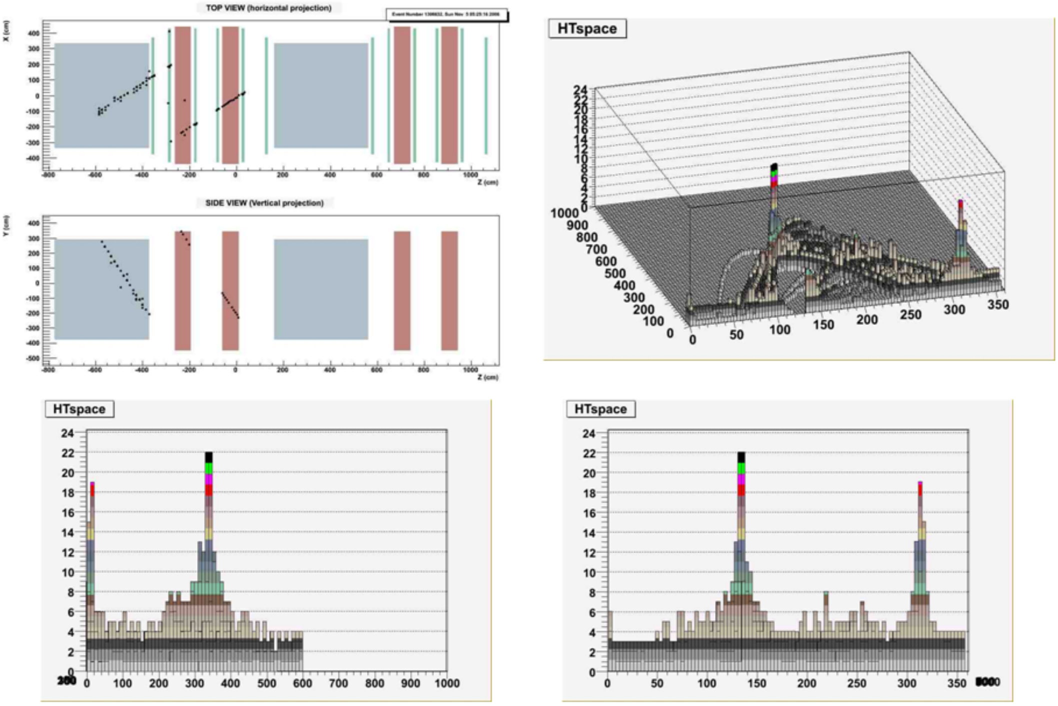

Figure 4.4: Example of a real muon pair event reconstructed with the Hough transform method. On the upper left panel, the event display is shown, in which the double-muon event is seen in the two projections T_{xz} and T_{yz}. On the upper right panel, the Hough space relative to one view, i.e. the feature space (ρ, ψ), is constructed, and the patterns of the two tracks are recognized by the histogram peaks in the bottom panels.

multiplicity. Then the digit positions associated with a track are fitted to determine the real track trajectory.

4.1.2 Track fitting in the Precision Tracker

A preliminary list of PT digits is provided by the general track finding algorithm using only the wire positions. The drift time information is treated independently and fitted by a dedicated software package, DTubeReco. The reconstruction procedures are detailed in [70]. The tracks in T_{xz} coming out from CosmicPattern are used to "guide" track finding in the PT system.

An iterative procedure reconstructs straight tracks fitting the best tangent line over all circles and simultaneously generates the time-to-distance relation (r-t relation), updated at each iteration [69]. The r-t relation converts the measured drift time into a spatial distance. In the following the reconstruction in the Precision Tracker is presented.

Pattern recognition

The PT pattern recognition fulfills two important functions. On the one hand it performs the pre-selection of PT digit candidates belonging to a track, on the other hand it delivers the start values for the track fit. The DTubeReco algorithm uses only the N drift tube digits which lie in a corridor 32 cm wide, defined by the general track parameters in T_{xz}, similarly to the CosmicPattern slice. The N drift times t can be converted into distances $r_i(t)$ between the track and the fired wire by using the r-t relation. This radius $r_i(t)$ of a circle around the sense wire is an unsigned quantity and does not determine on which side the particle passed the wire. The pattern recognition has to select the best sample of digit candidates, define the signs to resolve the right-left ambiguities and define the start angle and the start distance to the origin.

For the calibration of r-t relation and resolution function, used as a weight in the track fit, a PT system prototype was built at sea level, in order to collect enough (~ 5000) straight tracks [43, 69].

For track reconstruction with drift tubes the distance from the track to the wire is used. Thus it is convenient to describe the particle track with the Hesse form:

$$d_0 = z \sin\phi - x \cos\phi \tag{4.3}$$

The Hesse parameterization is very similar to the Hough one. Here d_0 is the track distance of the closest approach to the origin and ϕ the angle between track and z-axis

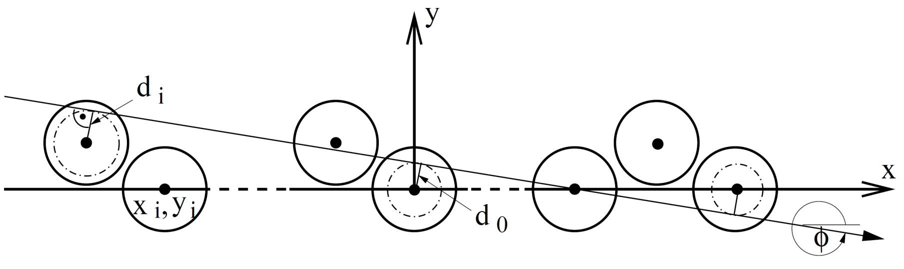

Figure 4.5: Track description using the Hesse form and definition of the parameters in the used coordinate system.

as defined in Fig. 4.5. The distance of closest approach to the anode wire d_i is then calculated by

$$d_i = d_0 - z_i \sin\phi + x_i \cos\phi \tag{4.4}$$

The index i describes the wire number i with the coordinates z_i and x_i. In the pattern recognition scheme the two tubes with the maximum distance between each other in one event will be used (Fig. 4.6). Now four possibilities exist to fit tangents (t_1 to t_4) to the radii r_1 and r_2. The tangent minimizing the χ^2 expression, defined by the N digits, will be selected

$$\chi^2 = \sum_{i=1}^{N} \frac{(r_i - d_i)^2}{\sigma^2} \tag{4.5}$$

where σ is the mean resolution, which is assumed to be the same for all tubes in the pattern recognition. For the first iteration σ is set to 1000 μm. The minimal χ^2 of the selected tangent has to be lower than a predefined maximal value (for the calibration, values between 100 and 500 were used). For higher values the whole event will be rejected. The origin of such events can be noise or cross-talk. If a valid tangent is found, the start parameters $d_{0\,\mathrm{start}}$ and ϕ_{start} are available for the track fit.

Track fitting

The initial parameter $\vec{q}_{\mathrm{start}}$ for the track fit, given by the pattern recognition, is

$$\vec{q}_0 = \vec{q}_{\mathrm{start}} = \begin{pmatrix} d_{0\,\mathrm{start}} \\ \phi_{\mathrm{start}} \end{pmatrix} \tag{4.6}$$

The track fit for the drift tube modules is described in details in [69]. The distances $d_{m,i}$ (calculated from the measured drift times) from the pattern recognition form a

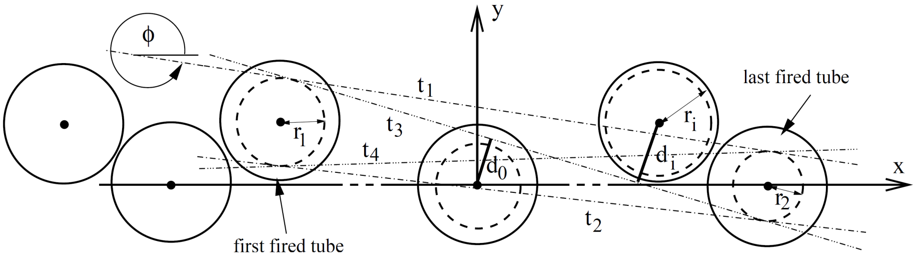

Figure 4.6: Example of the four tangents to the radii r_1 and r_2. The tangent, minimizing Eq. 4.5, is the best description of the true track.

vector $\vec{d}_m$ with dimension N. The measurement uncertainties σ_i for each used wire are collected in the resolution function, binned in time or space respectively. The squared values of this function are on the main diagonal of the $N \times N$ covariance matrix $\mathbf{V}$. The track will be described by the N dimensional vector $\vec{d}_t(\vec{q})$. The parameter $\vec{q}$ results from the fit of $\vec{d}_t(\vec{q})$ to $\vec{d}_m$. Using the least square method, the parameter $\vec{q}$ minimizes the expression

$$\chi^2 = \left[\vec{d}_m - \vec{d}_t(\vec{q})\right]^T \mathbf{W} \left[\vec{d}_m - \vec{d}_t(\vec{q})\right] \tag{4.7}$$

The weight matrix $\mathbf{W}$ is the inverse covariance matrix of the measured coordinates:

$$\mathbf{W} = \mathbf{V}^{-1} \tag{4.8}$$

Minimizing the χ^2 as a function of $\vec{q}$ yields the change of parameter $\Delta\vec{q}$, providing a better approximation for the successive iteration. The procedure is repeated until at the n^{th} iteration the end condition

$$\Delta\chi^2 = \chi^2_{n-1} - \chi^2_n < \Delta\chi^2_{min} \tag{4.9}$$

is fulfilled. For the fit described here a $\Delta\chi^2_{min} = 10^{-7}$ was used. The procedure converges usually after three iterations. After that the signs of $d_{m,i}$, determined by the pattern recognition, are changed if they are opposite to the signs of $d_{t,i}$. This procedure is repeated until no sign changes appear anymore (solution of left/right ambiguity). Digits with random time signals, due to noise or cross-talk, are removed if the χ^2 distribution is too large. The whole procedure is repeated, starting with the $\vec{q}_0$ from the pattern recognition, until $\chi^2 \leq \chi^2_{max}$. Finally, if still enough tubes N are left over for the reconstruction ($\geq N_{min} = 4$), the vector $\vec{q}_n$ of the last iteration contains the track parameters with the best track description. If not, the whole event is rejected.

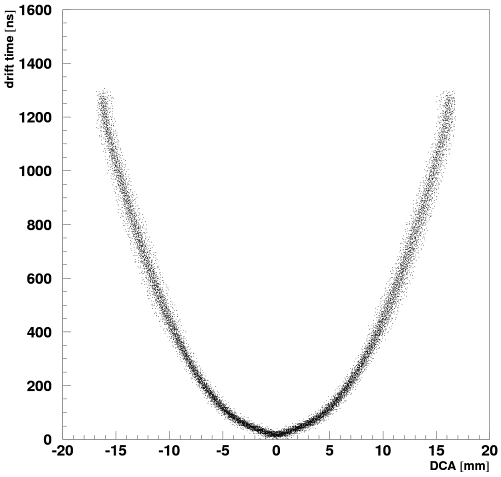

Figure 4.7: Correlation between drift times and distances, called r-t relation [43]. The measured drift time (t_D) on the y-axis corresponds to the fitted distance $d_t(t_D)$, i.e. the distance of the track from the wire, on the abscissa. The sign of the distance $d_t(t_D)$ refers to the side on which the track crossed the tube.

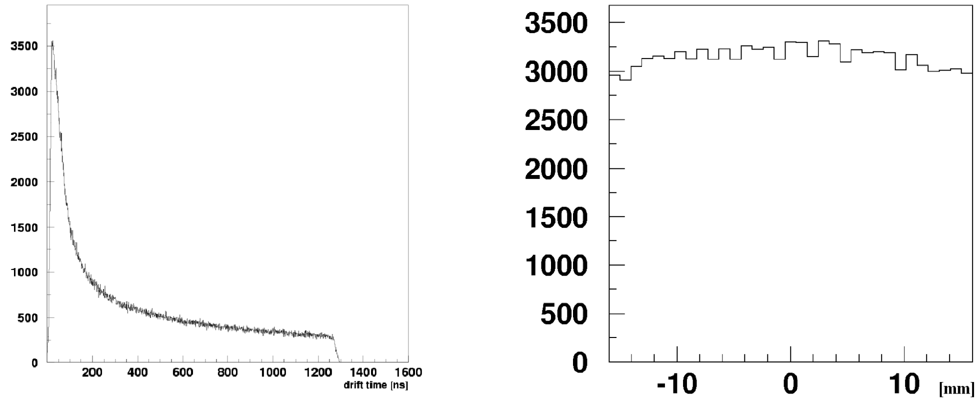

Figure 4.8: Distribution of the measured TDC times (left) [43]. The maximal drift time is 1.3 μs. On the right side the distribution of the fitted distances is shown [69].

The calibration of the r-t relation and the resolution function $\sigma(t_D)$ is based on the residual distribution $\epsilon(t_D)$ in each drift time bin, defined as the difference between the fitted drift distance d_t and the measured one d_m

$$\epsilon(t_D) \equiv d_t - d_m \tag{4.10}$$

At the end of the iterative procedure, the *r*-*t* relation and the resolution function are given. Fig. 4.7 shows the correlation between the fitted drift distances $d_t(t_D)$ and the drift times t_D. The mean values of the $d_t(t_D)$ distributions of both branches form the *r*-*t* relation. If the calibration is correct, the application of the *r*-*t* relation on the TDC times gives a flat distribution for the fitted distances, as shown in Fig. 4.8.

The resolution function $\sigma(t_D)$ is based on the RMS value of the residual distribution $\epsilon(t_D)$ in each time bin. Fig. 4.9 shows the function $\sigma(t_D)$ interpolated and smoothed by a cubic spline, while Fig. 4.10 shows the overall residual distribution. The RMS value yields the mean spatial resolution of the PT system: $\sigma_x \simeq 250\,\mu$m.

Track reconstruction in the PT stations

The drift tube fitting procedure just described is applied in each PT station pair: as explained in Sec. 2.2.4, two consecutive stations each made of 4 layers of drift tubes are placed outside the magnetic field at a mutual distance of about 1 m (Fig. 4.17). Since cosmic ray tracks can have very large angles with respect to the horizontal plane, for geometrical reasons many of them traverse only one single station of a pair and we refer to them as *singlets*, otherwise we call them *doublets*. The PT reconstruction deals in the first case with 4 layers of PT digits closely packed, in the second case with 8 layers, being the digit sets separated by about 1 m.

Due to the different lever arm the angular resolution for singlets is worse than for doublets. A simple geometrical evaluation, considering the mean spatial resolution $\sigma_x \simeq 250\,\mu$m, gives a mean angular resolution $\sigma_\phi \sim 1.6$ mrad over a lever arm $l = 16$ cm for singlets and $\sigma_\phi \sim 0.25$ mrad over a lever arm $l \sim 1$ m for doublets.

The angular resolution for singlets and doublets separately is computed from experimental and Monte Carlo data. For the cross-check presented from now on, we processed a parameterized event generation (Sec. 3.3.1) with the whole chain of the detector simulation (MC1 production hereafter). The output was finally reconstructed with the same packages used for experimental data.

Transforming the Hesse angle in the conventional angle ϕ between the particle direction and the z-axis, where $\tan\phi$ is the slope in the xz-plane,

$$\phi = \arctan(1/\tan\phi_{Hesse}) \tag{4.11}$$

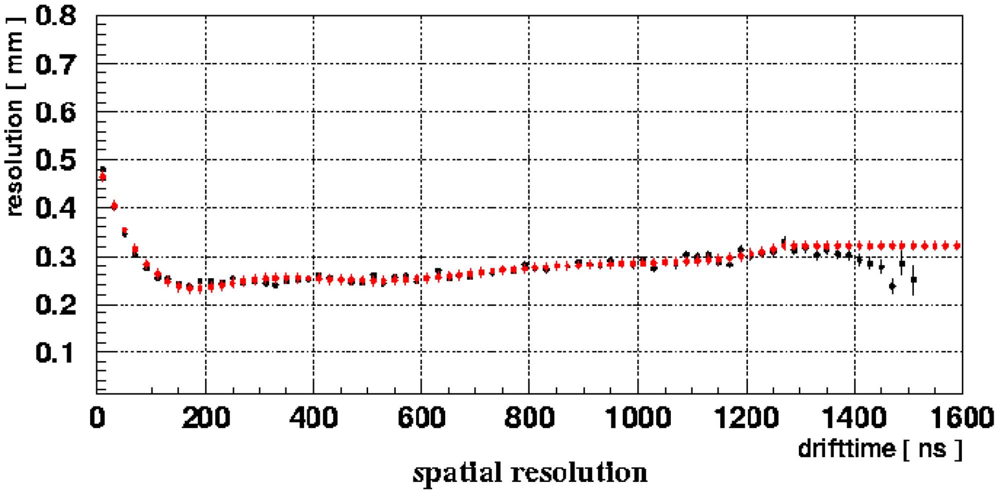

Figure 4.9: Resolution function (black squares) dependent on the drift time, fitted with cubic splines (red diamonds) [69].

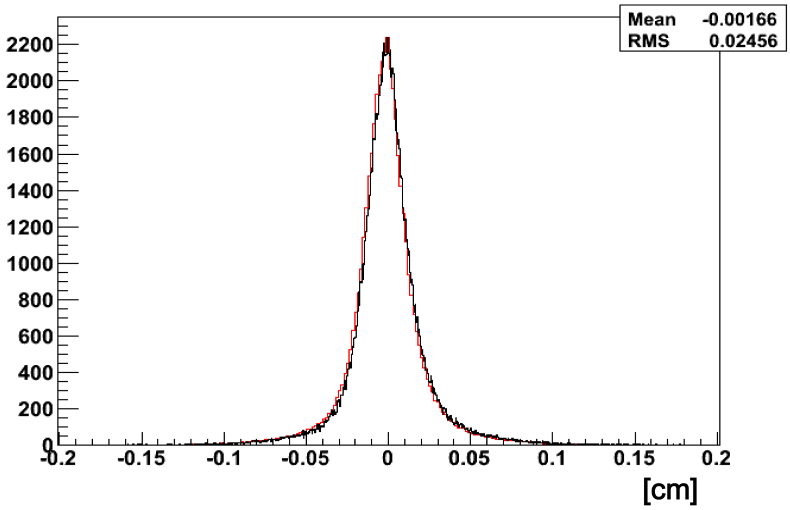

Figure 4.10: Distribution of the residuals for all the reconstructed drift distances (black line: experimental data, red line: Monte Carlo simulation). The RMS value yields the mean spatial resolution [70].

the functional dependence of σ_ϕ on ϕ, shown in Fig. 4.11, has been parameterized for experimental data in the range $\tan|\phi| = (0, 3)$:

$$\begin{aligned} \sigma_\phi^{singlet}(\text{mrad}) &= 1.77 - 0.52 \tan|\phi| \\ \sigma_\phi^{doublet}(\text{mrad}) &= 0.18 - 0.07 \tan|\phi| \end{aligned} \tag{4.12}$$

For tracks parallel to the z-axis ($\phi = 0$) it is $\sigma_\phi \sim 1.8$ mrad for singlets and ~ 0.18 mrad for doublets. Since for tilted tracks the number of fired tubes and their mutual distances are larger than for tracks with $\phi = 0$, the fit is better constrained and thus the error on the slope decreases.

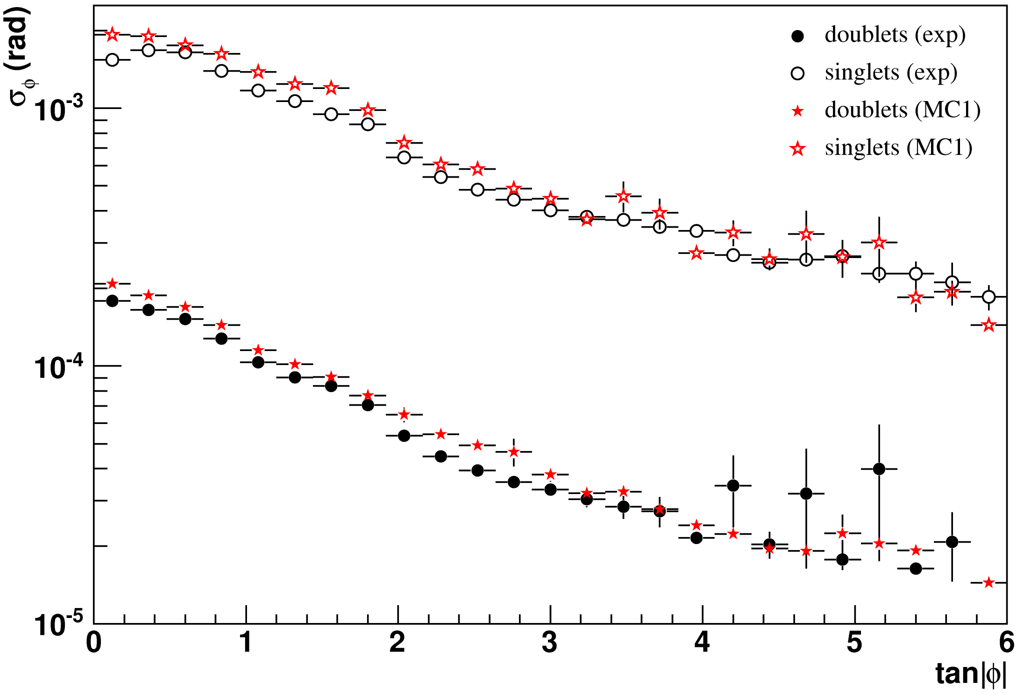

Figure 4.11: Angular resolution σ_ϕ as a function of $\tan|\phi|$ for experimental and MC1 data. The samples of singlets and doublets are separated, and experimental data in the range $\tan|\phi| = (0, 3)$ are fitted by Eq. 4.12.

The angular resolution σ_ϕ shown in Fig. 4.11 allows to compare the behaviour of experimental and MC1 data. The drift tube fit on experimental data gives systematically a better resolution than the MC1 data fit. We emphasize, however, that in the muon charge ratio analysis each track is treated with its own angular resolution, taken

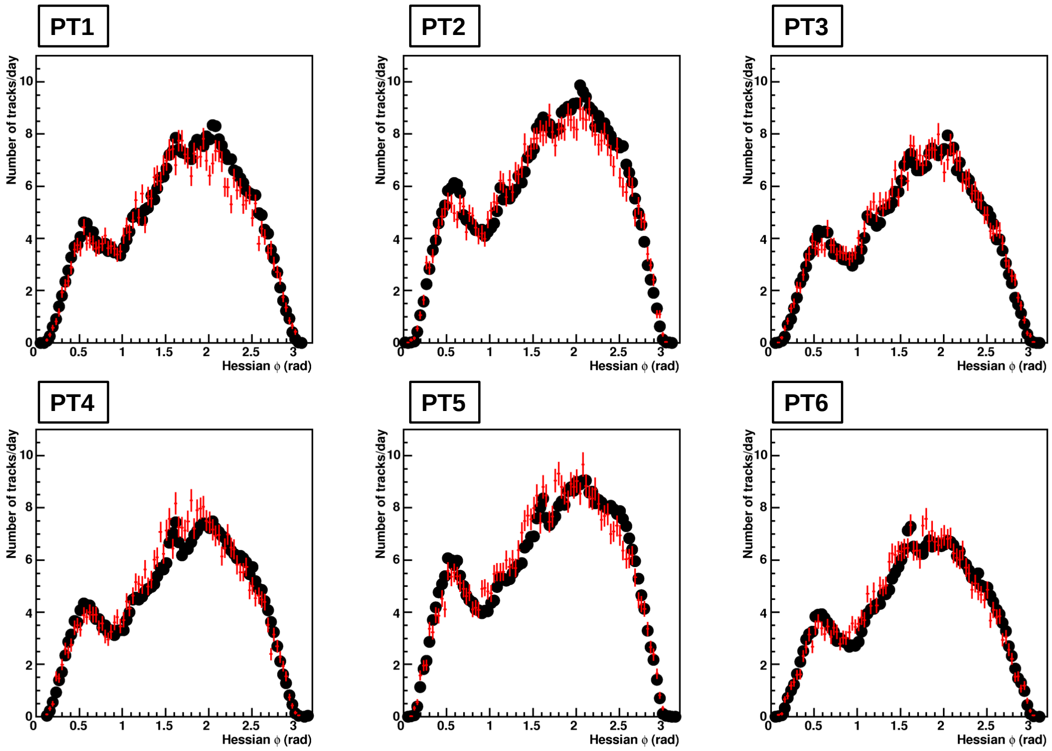

Figure 4.12: Hessian angle distribution in each PT station, for experimental data (black points) and MC1 (red line). The top plots refer to the three stations in the first spectrometer, the bottom plots refer to the second spectrometer.

from the covariance matrix. The parameterization given in Eq 4.12, based on the mean σ_ϕ value in each $\tan|\phi|$ bin, is not used to assign a value to each track, but simply to understand the PT measurement performance.

The results of the PT reconstruction algorithm applied both on experimental and on MC1 data are compared. Fig. 4.12 shows the ϕ_{Hesse} angle distribution in each PT station. In the associated σ_ϕ distributions in Fig. 4.13 the two samples of the singlets and the doublets are clearly visible. The small difference between the MC1 and the experimental distribution, seen also in Fig. 4.11, shows a slight systematics. In the next Chapter, we will show how the analysis presented in this thesis can overcome this effect. The MC1 was extensively used to check and validate the reconstruction chain and it will be used in the next Chapter for the computation of the charge mis-assignment

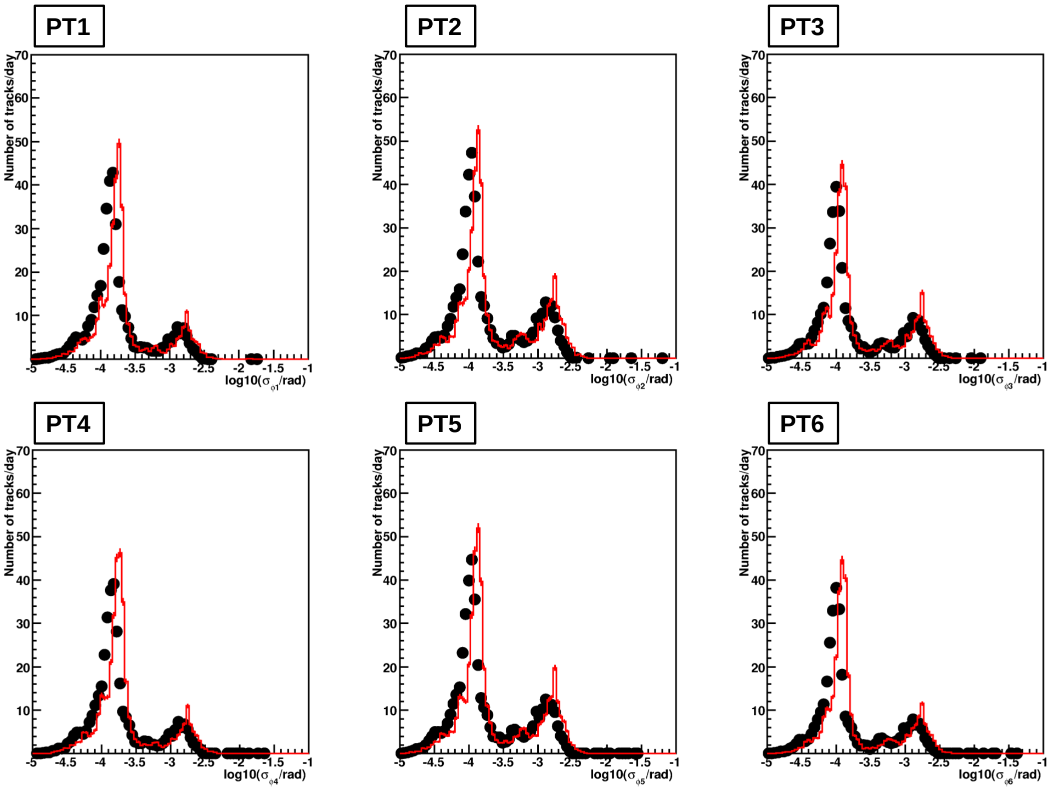

Figure 4.13: Angular resolution σ_ϕ distribution in each PT station, for experimental data (black points) and MC1 (red line). The top plots refer to the three stations in the first spectrometer, the bottom plots refer to the second spectrometer. The two peaks represent the distributions of singlets and doublets resolution.

probability. In the final part of this analysis, however, it will be completely dropped, since we use a procedure based only on the experimental data.

The two samples of singlets and doublets are separated in Fig. 4.14, where the number of PT digits per PT station is positive for doublets and negative for singlets.

4.1.3 Muon tracking algorithm

Before proceeding with the overall track fitting, the 2-D independent tracks in the T_{xz} and T_{yz} views are merged together to build a three-dimensional event. The Merging3D package orders the 2-D tracks according to the overall length and selects the possible associations. If the difference between the z (the common coordinate) for the two track

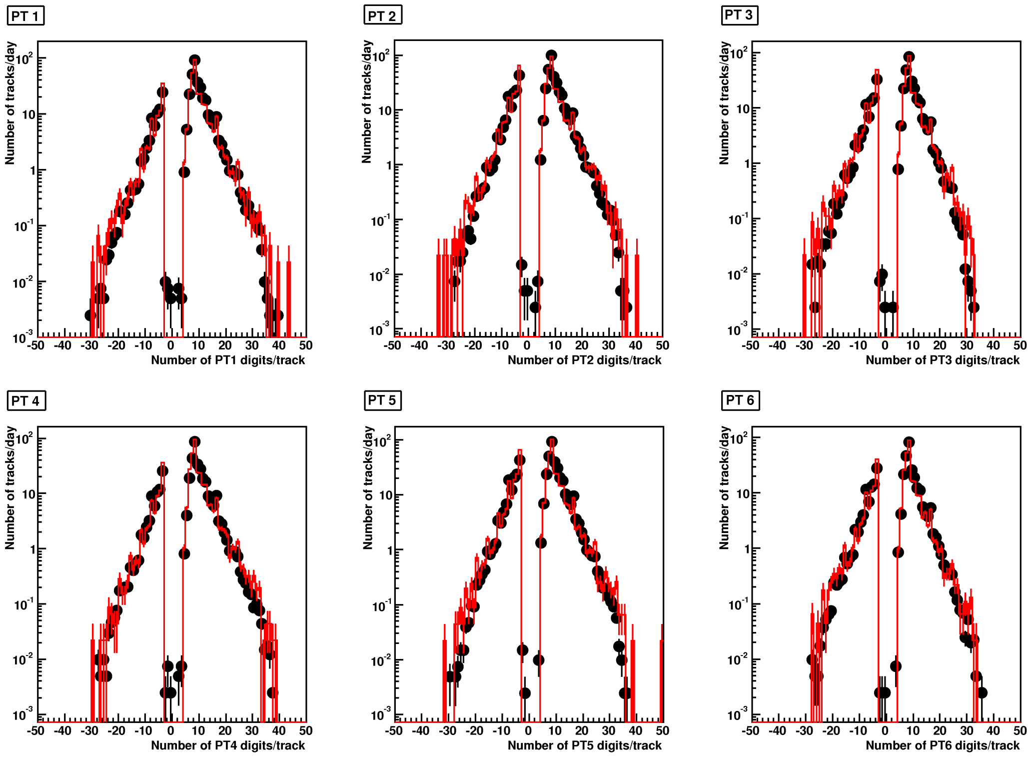

Figure 4.14: Number of PT digits per track in each PT station, for experimental data (black points) and MC1 (red line). The sign convention divides the distributions of singlets ($N_{PT} < 0$) and doublets ($N_{PT} > 0$).

ends satisfies the association criteria, the merging is finalized. In case of ambiguities, when the multiplicity in at least one view is greater than one, the 2-D tracks with the minimum Δz, defined as

$$\Delta z = |z_x^{first} - z_y^{first}| + |z_x^{last} - z_y^{last}| \tag{4.13}$$

are merged together.

Finally, for cosmic events, the tracking is performed only on 3-D tracks. A linear fit is applied both in the bending and in the not-bending view: since cosmic ray muons are high energy particles (the underground average muon energy is $\sim$ 270 GeV [72, 71]), the magnetic deflection is small enough to have practically no impact on the overall track direction. The resulting slopes in xz and in yz are used to extract the azimuth φ and zenith ϑ informations.

Using the MC1 simulation we estimated an angular resolution better than 1° both in the ϑ and φ directions, for single as well as for multiple track events (Fig. 4.15).

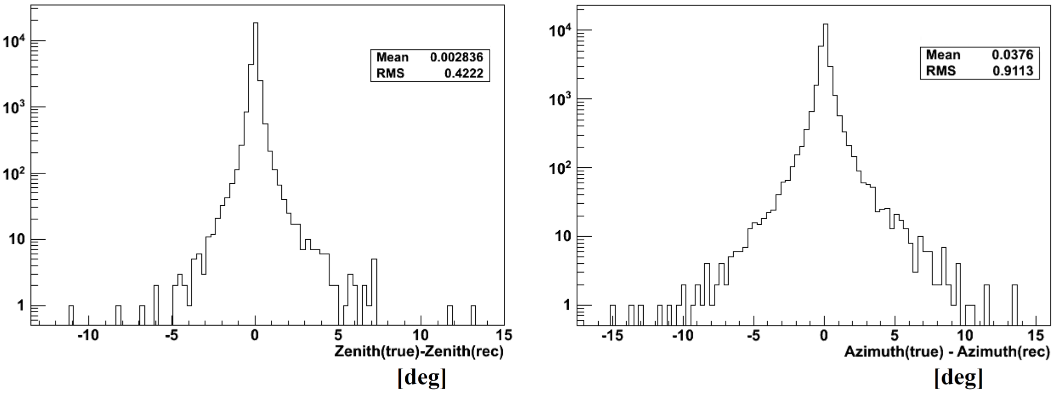

Figure 4.15: Angular resolution obtained with the OPERA cosmic reconstruction. The RMS of both the distributions in ϑ and φ is lower than 1°.

At the end of the tracking phase, a *flag* associated to the reconstruction quality is assigned to each event. The flag definition is based on

- a minimum number of digits/track, $N_{digit} > 7$ in both projections, in order to have a valid slope measurement;
- the fraction f of the track digits over the total number of event digits, $f > 0.4$, to recognize noisy events;
- a parallelism condition if the multiplicity is greater than one. The angular difference in track direction $|\theta_i - \theta_j|$ for each muon pair i, j is required to be less than 3.5° in both projections (the tolerance value was estimated with Monte Carlo).

Events fulfilling all the requirements in both projections are flagged as "good quality" events.

A final algorithm computes the rock overburden for each (ϑ, φ) direction. A detailed Gran Sasso rock map $h(\vartheta, \varphi)$ has been derived from the elevation map over the underground Hall C, provided by the Italian geodetic institute (IGM) in DTM format (Sec. 3.3.1). The comparison between experimental and MC1 "good quality" tracks is shown in Fig. 4.16, where the main global distributions are presented. The tiny difference between experimental and MC1 data for the zenith and azimuth distributions is due

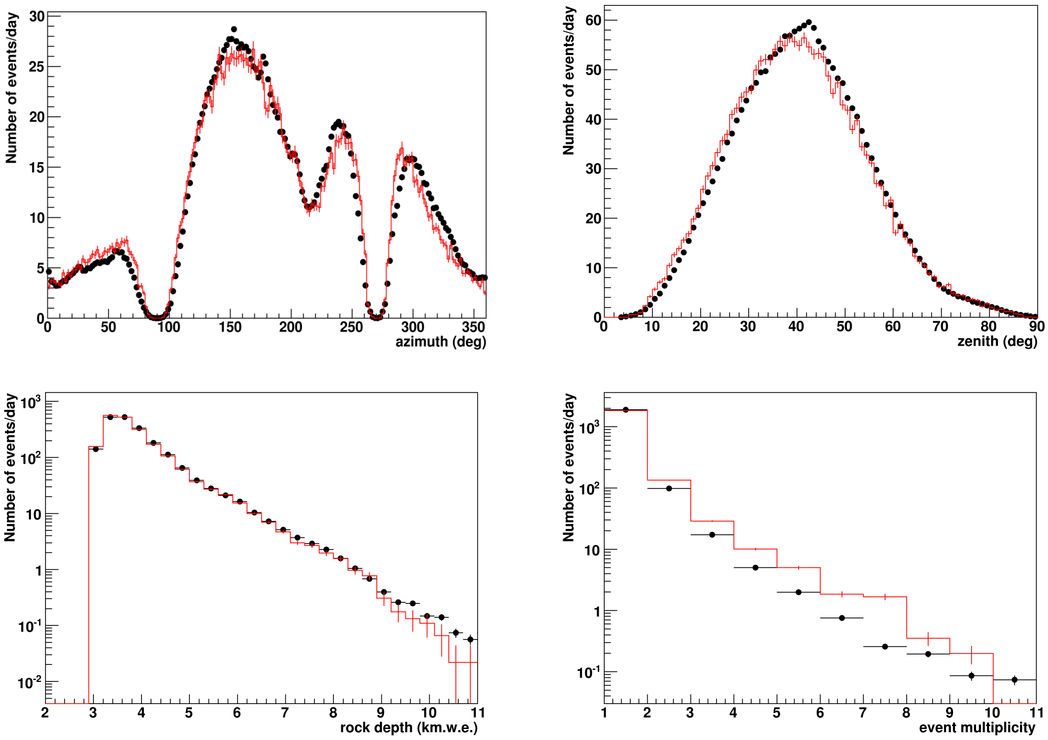

Figure 4.16: Global event variable distributions for experimental (black points) and MC1 (red line) data. On the upper left plot, the azimuth angle φ; on the upper right, the zenith angle ϑ; on the bottom left the rock depth and on the bottom right the event multiplicity.

to the fact that MC1 data were produced using the map centered in the Hall B, since we adapted to our purposes the Monte Carlo for the MACRO experiment. OPERA data, taken in Hall C, show a mismatch within 5% with respect to MC1, consistent with the mismatch between the two rock maps in Hall B and C. The mismatch between data and MC1 in the multiplicity distribution shown in the bottom right panel will be detailed in the following Section.

The overall agreement between the distributions validates the Monte Carlo simulation and highlights the good capability of OPERA as a cosmic ray detector.

XZ view	$n_\mu = 1$	$n_\mu = 2$	$n_\mu = 3$	$n_\mu = 4$	$n_\mu \geq 5$
YZ view					
$n_\mu = 1$	89.9	0.7	0.03	<0.01	<0.01
$n_\mu = 2$	0.3	6.1	0.3	0.02	<0.01
$n_\mu = 3$	<0.01	0.2	1.2	0.1	0.01
$n_\mu = 4$	<0.01	<0.01	0.08	0.3	0.09
$n_\mu \geq 5$	<0.01	<0.01	0.02	0.08	0.5

Table 4.1: Fraction of event multiplicities reconstructed in the two projected views.

Event multiplicity

The peculiarity of the OPERA detector reconstruction is that multi-muon events are taken into account. An event is defined as multi-muon if the 3-D track multiplicity is greater than one. The reconstruction flag classifies the parallelism among the tracks. Track directions are averaged for multiple muon events: all the tracks belonging to a bundle have the same azimuth, zenith and thus rock depth. Tab. 4.1 shows the fraction of events for each multiplicity in both projections. The "off-diagonal" values are symmetrically distributed.

The 3-D event multiplicity distribution shown in Fig. 4.16 for experimental and MC1 "good quality" events reveals the good performance of the reconstruction scheme, designed on purpose toward this kind of topologies. However the event multiplicity reconstruction strongly depends on the subdetector granularity. Close tracks in a TT view will be reconstructed as two separate tracks if the digit clustering is small enough. We found that detector simulation did not perfectly reproduce the correct number of digits for high multiplicity events.

4.2 Charge and momentum measurement

The momentum measurement and the charge determination are performed using the deflection of charged particles in the magnetic field (Fig. 4.17). In this Section we describe the main steps used to extract charge and momentum from PT track fitting information.

From now on we refer to ϕ as the angle between the particle direction and the z-axis. The deflection $\Delta\phi$ is the difference between the two angles measured by the PT stations at each side of the magnet arm. In order to increase the statistics we decided to consider both singlets and doublets concurring to the ϕ measurement: the percentage

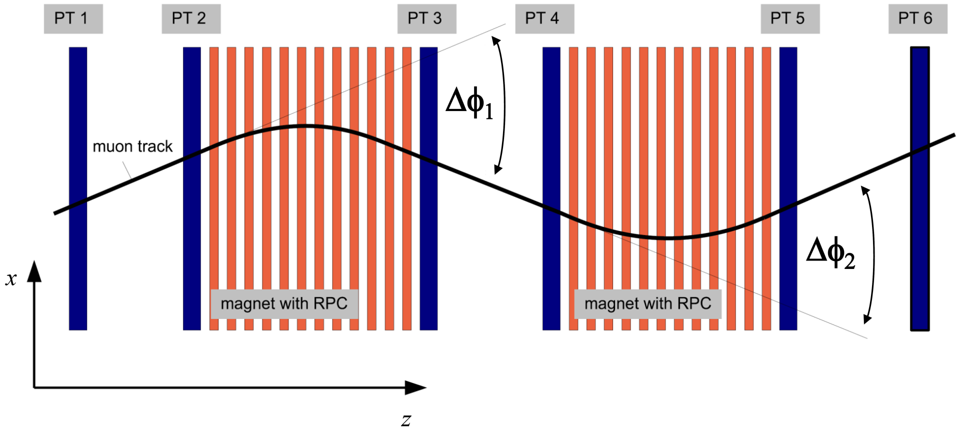

Figure 4.17: Schematic view of a charged particle crossing one spectrometer. The six PT stations are shown in blue; the 24 iron slabs (12 per arm) interleaved with 22 RPC planes are shown in red. Each spectrometer arm provides a measurement of charge/momentum using the deflection $\Delta\phi_i$, provided the track is reconstructed in at least one station (or station doublet) at each side of the arm.

of cases in which both angles are reconstructed from doublets is ~55% of the total, ~9% are from singlets and the remaining 36% are from mixed configurations, i.e. cases where one angle is reconstructed from a doublet and the other angle from a singlet.

We define a naming convention: the 6 possible ϕ angles are named from 1 to 6, starting from the first PT pair of SM1. The 4 possible deflection angles are named from 1 to 4, where

$$\begin{aligned}\Delta\phi_1 &\equiv \phi_2 - \phi_1\\ \Delta\phi_2 &\equiv \phi_3 - \phi_2\\ \Delta\phi_3 &\equiv \phi_5 - \phi_4\\ \Delta\phi_4 &\equiv \phi_6 - \phi_5 \end{aligned} \tag{4.14}$$

Thus the first spectrometer, with $\phi_{i=1,2,3}$, can provide the two $\Delta\phi_1$ and $\Delta\phi_2$ measurements (Fig. 4.17); similarly the second spectrometer, with $\phi_{i=4,5,6}$, can provide the two $\Delta\phi_3$ and $\Delta\phi_4$ measurements.

To measure the charge and the momentum of a particle at least one $\Delta\phi$ angle is needed (for tracks parallel to the z-axis there can be up to 4 independent angles).

For each reconstructed $\Delta\phi_i$ the track momentum is computed following the procedure detailed in [70]. The radius of curvature is estimated using the standard formula

$$r_i = \frac{p_i}{e\bar{B}} = \frac{p_i\, l}{eBd} \tag{4.15}$$

where $\bar{B} = B\, d/l$ is the effective magnetic field in the magnetized iron arm with thickness $d = 0.6$ m and total length $l = 0.82$ m (including RPC gaps). A constant magnetic field $B = 1.53$ T is considered. Traversing the iron arm, the particle loses part of its energy and the momentum p_i varies with the longitudinal coordinate z

$$p_i = p_i(z) = p_{0i} - \frac{z}{c}\frac{\mathrm{d}E}{\mathrm{d}z} \tag{4.16}$$

where p_i is the instantaneous momentum and p_{0i} is the initial particle momentum. The ionization energy loss dE/dz, which depends logarithmically on the muon momentum, is computed using the momentum estimate $p_i = 0.3B\, d/\Delta\phi_i$. The infinitesimal angular deflection is then

$$\delta\phi_i = \frac{\mathrm{d}z}{r_i} = \frac{\mathrm{d}z\, e\bar{B}}{p_{0i} - z(\mathrm{d}E/\mathrm{d}z)} \tag{4.17}$$

Integrating Eq. 4.17 over the total arm length l, the deflection in the magnet arm $\Delta\phi_i$ is given

$$\Delta\phi_i = \int_0^l \frac{e\bar{B}}{p_{0i} - z(\mathrm{d}E/\mathrm{d}z)}\mathrm{d}z = -\frac{e\bar{B}}{(\mathrm{d}E/\mathrm{d}z)} \ln\left(1 - \frac{l(\mathrm{d}E/\mathrm{d}z)}{p_{0i}}\right) \tag{4.18}$$

Inverting Eq (4.18) the particle momentum transverse to the magnetic field direction $p_{xz} \equiv \sqrt{p_x^2 + p_z^2}$ follows

$$(p_i)_{xz} = \frac{l(dE/dz)}{1 - \exp[\Delta\phi_i(\mathrm{d}E/\mathrm{d}z)/e\bar{B}]} \tag{4.19}$$

The total particle momentum is given by

$$p_i = (p_i)_{xz}\sqrt{1 + \frac{s_{yz}^2}{1 + s_{xz}^2}} \tag{4.20}$$

where s_{yz} and s_{xz} are the track slopes in the T_{yz} and T_{xz} views.

The muon charge is determined from the sign of the $\Delta\phi_i$ angle, accounting for the particle arrival direction and the field orientation in the arm. A muon crossing the whole spectrometer is deflected with opposite bending in each arm of the dipolar magnet: for a positive muon moving in the beam direction, the standard magnet polarity is such that $\Delta\phi_1 < 0$ and $\Delta\phi_2 > 0$, likewise for SM2. If the particle moves in the reverse direction or the magnet polarity is changed, the sign is inverted.

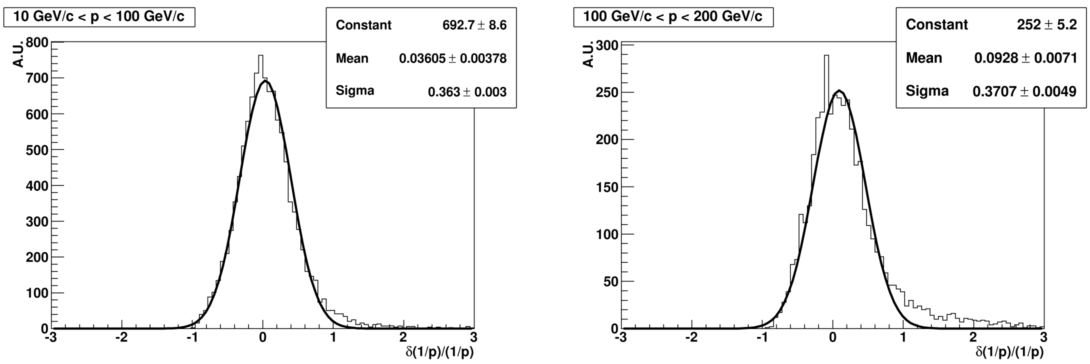

Figure 4.18: Momentum resolution distribution in two true momentum ranges. The Gaussian fit yields the mean resolution σ in the selected momentum range, $(10 < p < 100)$ GeV/c and $(100 < p < 200)$ GeV/c.

In case of more than one $\Delta\phi$ information, each deflection angle was weighted according to its measurement accuracy:

$$w_i = \frac{1}{\sigma_j^2 + \sigma_k^2} \tag{4.21}$$

where j and k are the indices of the relative $\phi_{j,k}$ giving $\Delta\phi_i = \phi_j - \phi_k$. The final muon momentum and charge are computed as the weighted average of the independent measurements:

$$\begin{aligned} p &= \frac{\sum_{i=1}^{4} w_i p_i}{\sum_{i=1}^{4} w_i} \\ q &= \frac{\sum_{i=1}^{4} w_i q_i}{\sum_{i=1}^{4} w_i} \end{aligned} \tag{4.22}$$

Considering tracks with $\phi = 0$ and the Multiple Coulomb Scattering (MCS) within one magnet arm the total uncertainty on $\Delta\phi$ is

$$\sigma_{\Delta\phi} = \sqrt{\sigma_{\phi_1}^2 + \sigma_{\phi_2}^2 + \left(\frac{0.0136}{p}\right)^2 \frac{d}{X_0}} \tag{4.23}$$

where $X_0 = 0.0176$ m is the iron radiation length and p is expressed in GeV/c. Since the deflection due to the magnetic field is

$$\Delta\phi_B = \frac{0.3B\,d}{p} \tag{4.24}$$

the requirement $\Delta\phi_B/\sigma_{\Delta\phi} > 1$ provides an estimate for the maximum detectable momentum, $p_{max} \simeq 1$ TeV for doublets, $p_{max} \simeq 150$ GeV for singlets and $p_{max} \simeq 260$ GeV for mixed configurations.

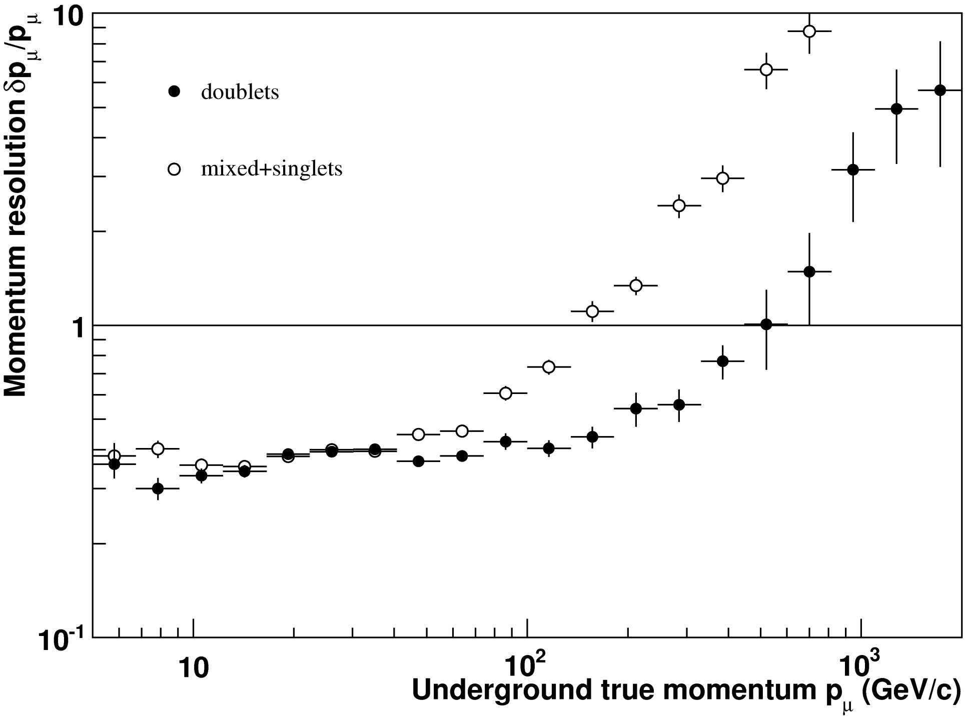

Figure 4.19: Momentum resolution as a function of the true MC momentum. Black points are doublets, white points are singlets and mixed configurations together.

Using the Monte Carlo simulation MC1, the momentum resolution is computed for all the angles. In Fig. 4.18 the resolution distribution $\delta(1/p)/(1/p)$ is shown for two true momentum ranges, $(10 < p < 100)$ GeV/c and $(100 < p < 200)$ GeV/c. Fig. 4.19 shows the resolution $\delta p/p$ as a function of the true MC momentum for doublets and for singlets/mixed separately. In this plot, the value where the resolution curve crosses the line $\delta p/p = 1$ identifies the maximum detectable momentum: $p_{max} \sim 500$ GeV for doublets and $p_{max} \sim 150$ GeV for singlets and mixed configurations.

For muon momenta $p \ll p_{max}$ the measurement error can be neglected and the only contributions to the $\Delta\phi$ uncertainty come from the MCS. In this ideal case the ratio $\Delta\phi_B/\Delta\phi_{MCS} \sim 3.5$ corresponds to a charge-misidentification η (defined as the fraction of tracks reconstructed with wrong charge sign) below 10^{-3}. Actually there are other effects which spoil the resolution and therefore the charge identification capability, as detailed in the next Chapter.

The performances of the momentum reconstruction in OPERA are evaluated with the MC1 production. In Fig. 4.20 the deflection $\Delta\phi$ as a function of the true MC momentum is shown. The linear behaviour is respected until the angular resolution is reached. Around ~ 1 mrad $\Delta\phi$ starts approaching $\sigma_{\Delta\phi}$, thus the deflection information saturates. This effect is visible also in Fig. 4.21, where the reconstructed momentum is plotted as a function of the true momentum. The mean value in each bin is superposed to the population distribution. The linear correlation is respected in the range (0.5, 2.8) in logarithmic scale, corresponding to the range (3, 700) GeV/c. Similarly to what happens in Fig. 4.20, around 1 TeV/c the PT resolution flattens the reconstructed momenta. Below 3 GeV/c, the algorithm philosophy is not optimized and the reconstructed momentum is overestimated.

In the next Chapter a set of quality cuts is presented and applied in order to have a cleaner sample of charge- and momentum-reconstructed muons.

4.3 Alignment of the PT system

The measurement of the muon charge is strongly affected by the alignment precision of the PT system. Misalignment effects have “global” or “local” contributions. To correct for global effects, which are the dominant ones, each station is treated as an independent rigid body and relative rotations and translations of one station with respect to the others are searched for. The local misalignment contribution takes into account possible distortions or bendings within each station.

A first alignment campaign was carried out with a theodolite to measure the position of the PT walls in the OPERA coordinate system.

Since the underground cosmic ray muon energies are on average much larger than the CNGS event energies, for the muon charge ratio analysis we need a more refined alignment in order to not spoil the detector resolution and to not introduce systematic affects. Thus cosmic ray muon tracks were used to test and align the PT system. The alignment procedure was carried out in two steps a) PT stations forming a doublet were aligned with the whole data sample, since the space in between has no magnetic field and tracks do not suffer any deflection; b) each doublet (pair) treated as a unit, separated by the iron magnet arm, was aligned using special runs with the magnetic field switched off. In Appendix A the alignment method using cosmic ray tracks is explained in details.

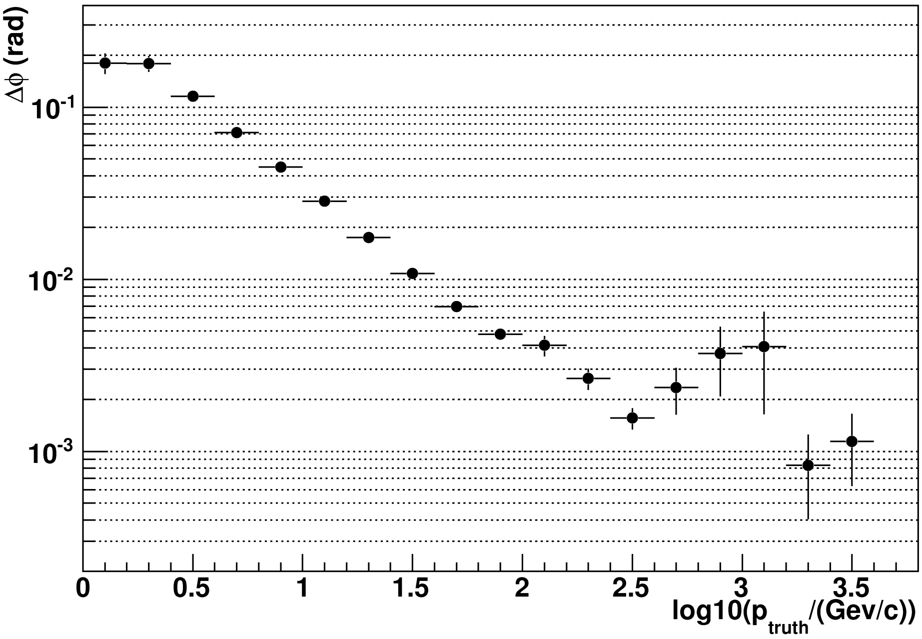

Figure 4.20: Reconstructed $\Delta\phi$ versus true muon momentum obtained with MC1. The linear correlation is respected until the angular resolution is reached. Around $\Delta\phi \sim 1$ mrad the saturation effect starts, i.e. $\Delta\phi \rightarrow \sigma_{\Delta\phi}$.

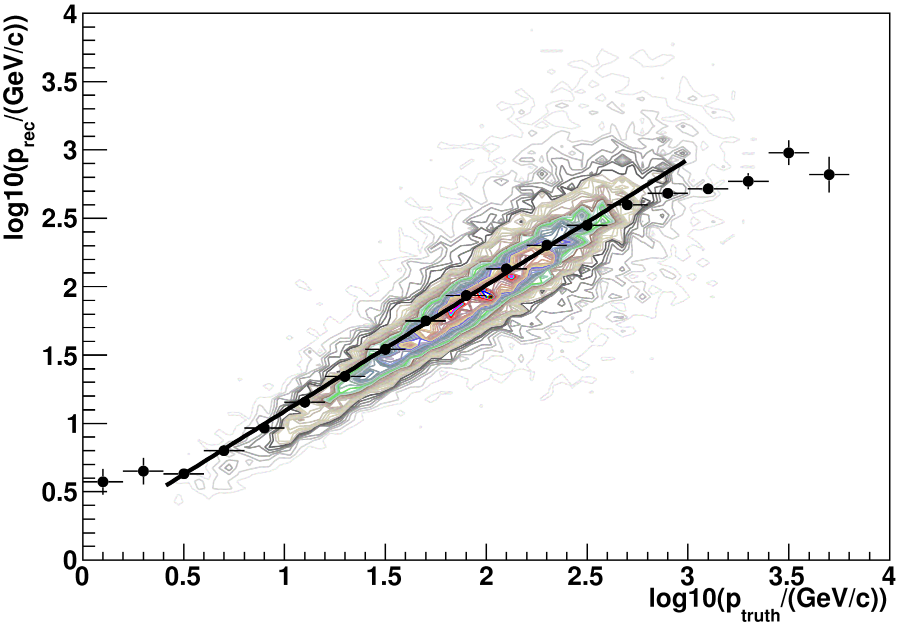

Figure 4.21: Reconstructed as a function of true muon momentum obtained with MC1. The linear correlation is respected in the range (0.5, 2.8) in logarithmic scale, corresponding to the range (3, 700) GeV/c. Around 1 TeV/c the PT resolution flattens the reconstructed momenta. Below 3 GeV/c, the algorithm philosophy is not optimized and the reconstructed momentum is overestimated.

The *intra-doublet* alignment is performed applying the reconstruction described in Sec. 4.1.2 in each PT station individually. For each muon, the track reconstructed in one PT station is projected and compared to the track reconstructed in the other PT station. Fitting the residuals between the two PT stations as a function of the track angle ϕ the translation parameters between the two stations are obtained (App. A). Once each PT doublet is aligned, it can be treated as a rigid body. The *doublet-doublet* alignment is performed similarly to the *intra-doublet* alignment, but applying the PT standard reconstruction.

This procedure allowed aligning two PT stations within a doublet with a spatial accuracy of ∼0.1 mm and an angular accuracy of ∼0.1 mrad, and to align two doublets with an angular accuracy of 0.2 mrad.

Local effects, such as bendings or distortions, contribute at the second order level and due to the present limited statistics have not been corrected for. However in Sec. 5.4 we provide an estimate of the systematic uncertainty on R_μ introduced by these effects.

Chapter 5

Measurement of the Charge Ratio

The atmospheric muon charge ratio R_μ is an important indicator of both cosmic ray and particle physics items: as discussed in Chapter 1, the charge ratio at sea level is mainly a convolution of primary composition aspects and high energy hadronic interaction effects. The two aspects are correlated and the poor knowledge of one of these subjects determines a source of uncertainty on the other one.

The interpretation of indirect measurements which are used to determine the features of primary cosmic rays, such as spectra and composition, depends on the choice of the hadronic interaction model adopted in the description of the atmospheric shower development. But, as previously pointed out, muons observed by deep underground experiments are the decay products of mesons originating mostly in kinematic regions (high rapidity and high $\sqrt{s}$) not completely covered by existing accelerator data. On the other side, neither the primary cosmic ray composition is well known at very high energy, where heavier elements are expected to become important. Thus, drawing a conclusion on favored interaction models is biased by the input "particle beam".

It is therefore crucial to find physical observables which are primarily sensitive to the assumed interaction model rather than to the energy spectra and chemical composition of primary cosmic rays.

In this Chapter, we try to disentangle the two dependencies in the analysis of the muon charge ratio.

5.1 Data analysis

The results here presented are based on data recorded during the CNGS Physics Runs 2008 (from June 18th until November 3rd, 2008), 2009 (from June 1st until November 23rd, 2009) and 2010 (from April 29th until November 22nd, 2010). The OPERA detector ran with the standard magnet polarity, i.e. with the magnetic field directed along the upward vertical direction in the first arm of both spectrometers, and in the opposite direction in the second arm. A sample of cosmic ray muons was collected with the magnetic field switched off in order to improve the alignment between PT stations and to evaluate systematic uncertainties. A limited data sample (9 days at the end of the 2008 Run and 7 days during the 2010 Run) was obtained inverting the magnet polarity to cross-check the charge reconstruction.

The data set is segmented after the last trigger level in “extraction periods” of about 12 hours each. The final requirement to store events in persistent data model is a minimum number of digits in both the projection views:

$$(N_{digit})_{xz} \geq 5 \quad \& \quad (N_{digit})_{yz} \geq 5$$

This request has no impact on the muon reconstruction efficiency. The fraction of events with only 4 aligned digits in both projections due to actual cosmic muons is negligible. On the other hand, this cut reduces the fraction of events with very few sparse digits due to noise. Fig. 5.1 shows the distributions of the number of digits/track in the PT sub-detectors, for events flagged as “good reconstructed” (Sec. 4.1.3).

The selection of good data quality extractions is done on the basis of the following distributions:

- for each extraction j the average rate of muons/hour $\langle N_\mu \rangle_j$ and the average numbers of TT, RPC and PT digits/track $\langle N_{RPC} \rangle_j$, $\langle N_{TT} \rangle_j$ and $\langle N_{PT_{i,i=1,\ldots,6}} \rangle_j$ are computed;
- all these averaged values are collected in the overall Physics Run distributions, shown in Fig. 5.2;
- the mean $\langle N_k \rangle_{Run}$ and $\mathrm{RMS}(N_k)_{Run}$ values are extracted from each distribution k;
- the selection cut requires:

$$|\langle N_k \rangle_j - \langle N_k \rangle_{Run}| \leq 3\,\mathrm{RMS}(N_k)_{Run} \quad \text{for each } k.$$

Extractions with at least one value out of 3 RMS from the mean value are rejected.

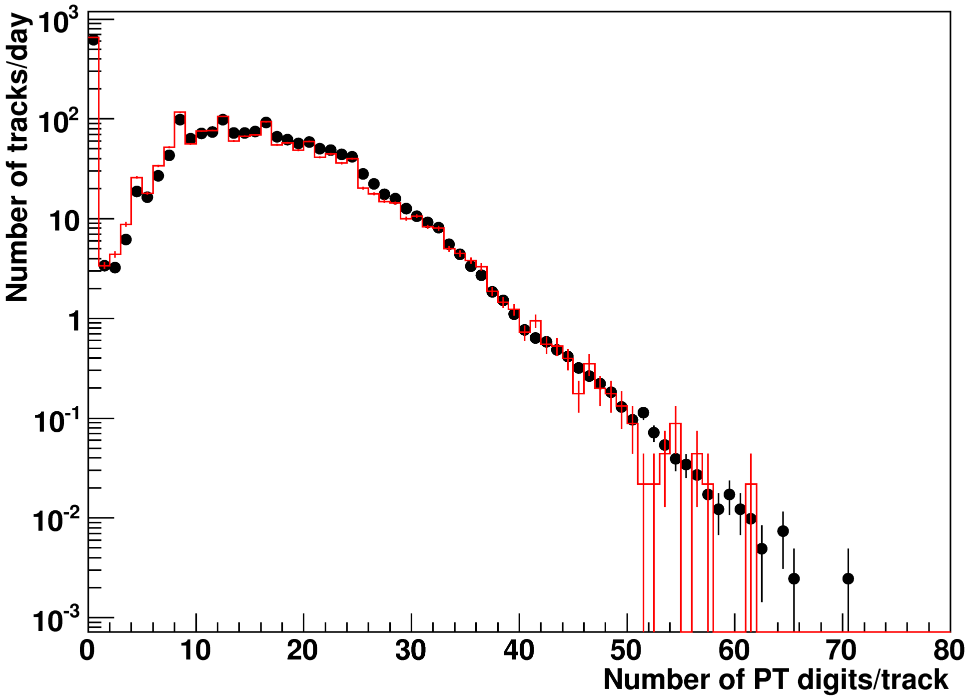

Figure 5.1: Distributions of the number of PT digits/track for experimental (black dots) and MC1 (red line) data. The overall shape of the distributions validates the Monte Carlo simulation.

The selection cut is defined on the global distributions themselves, shown in Fig. 5.2. This procedure is done for each Physics Run separately to take into account possible differences in the detector configuration at the beginning of each new Run. The overall distributions for the three years of data taking are superimposed in Fig. 5.2, showing the stability of the detector performances.

After this selection, only periods of data taking where all the main detector subsystems ran in stable conditions are considered. The total number of selected events and the corresponding days of livetime are shown in Tab. 5.1.

Data are then merged together, given the comparable values of the distributions considered. Fig. 5.3 shows the average rate of events/hour in each extraction, for the three Runs separately. Before merging the three years data, the PT alignment in each Run was checked with the procedure described in Sec. 4.3. We found a small difference in the alignment between 2008 and 2009, while 2009 and 2010 are compatible within

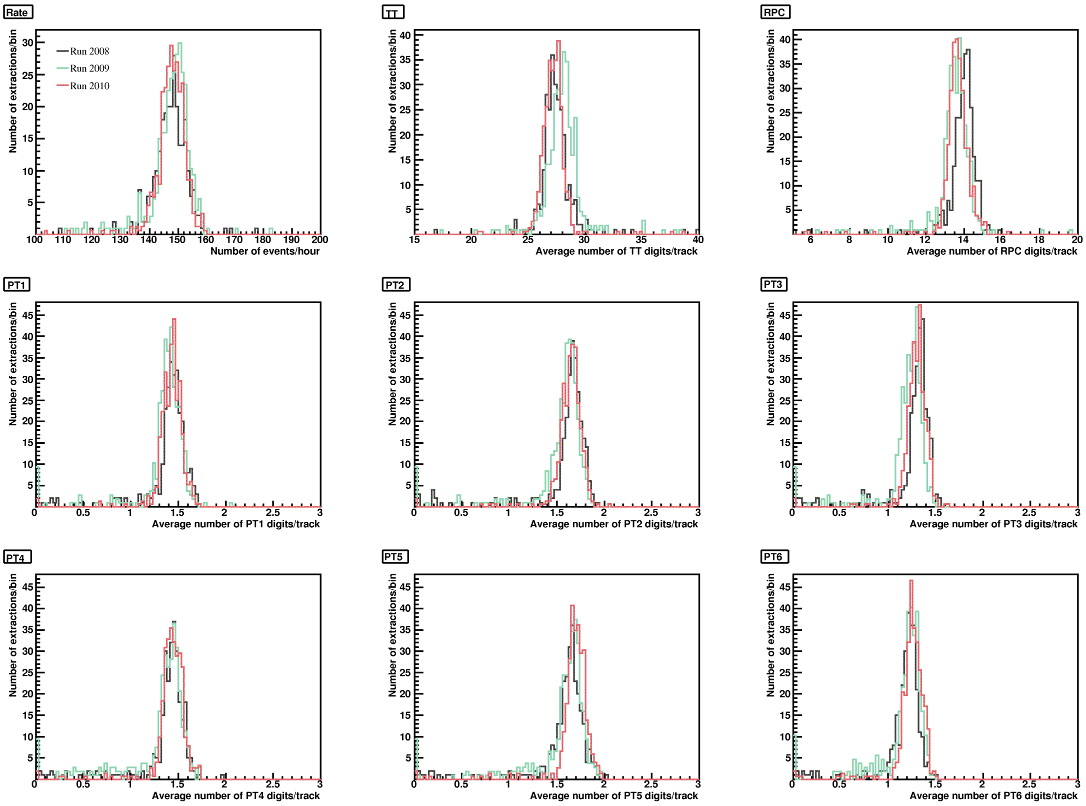

Figure 5.2: Global distribution of the averaged variables in each extraction: muon rate in the extraction (top left), average number of TT, RPC digits/track and PT digits/track in each station pair.

the alignment errors. A possible explanation is the earthquake of April 6th, 2009 in L' Aquila region. The tiny *intra-doublet* displacement in z (below 1 mm) was corrected for 2009 and 2010 data together, before going on with the reconstruction chain.

Applying the livetime normalization the ratio between OPERA data and MC1 prediction is

$$\frac{\mathrm{Rate}_{\mathrm{OPERA}}}{\mathrm{Rate}_{\mathrm{MC1}}} = (96.3 \pm 0.3)\% \tag{5.1}$$

The difference from unity can be ascribed to the livetime estimation, given the extraction selection over periods of 12 hours. Once the extraction is tagged as “good data quality”, the actual length is computed using the event timing information, but even a small percentage of dead time during the extraction (e.g. a sub-detector switched off for a short period due to an intervention), not recognizable by the overall selection,

	events	livetime (days)	rate (events/day)
Run 2008	403038	113.42	3554
Run 2009	434214	121.05	3588
Run 2010	616805	172.65	3574
Total	1454057	407.12	3572

Table 5.1: Total number of events contained in the selected extractions, corresponding days of livetime and average daily rate, for each Physics Runs.

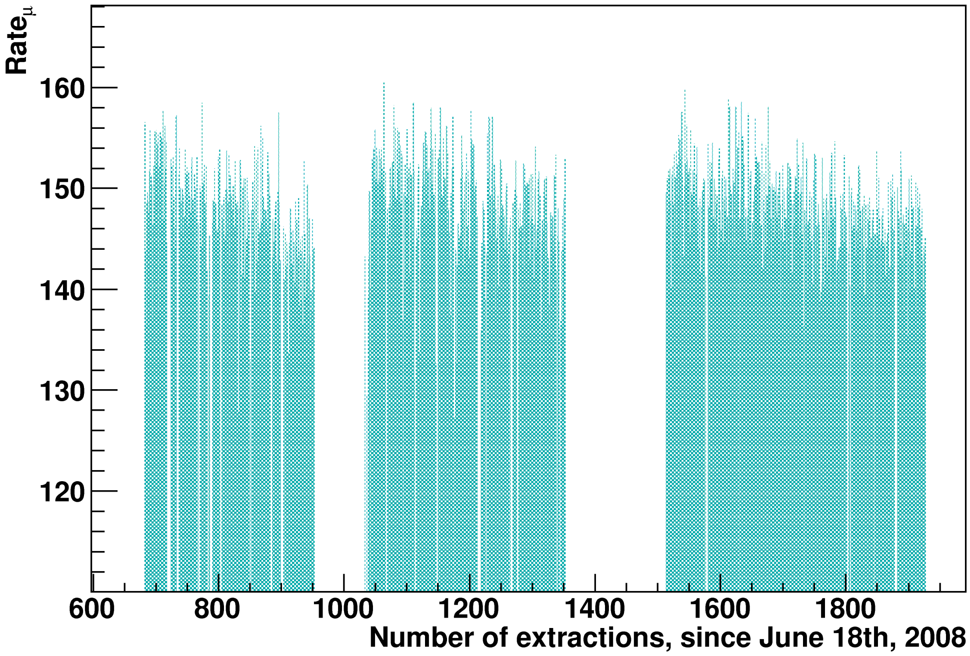

Figure 5.3: Average event rate, expressed in events/hour, in each extraction period (∼ 12 hours). The three years 2008, 2009 and 2010 are separated by the CNGS shutdown. The empty columns within a Run refer to the extractions removed by the selection procedure.

can lead up to the ratio OPERA/MC1. Moreover, the systematic errors related to the primary flux and the hadronic interaction model cancels (see Sec. 3.3.1).

5.2 Quality cuts

A set of data quality cuts was applied to isolate a clean sample of charge reconstructed muon events.

Acceptance cut At least one reconstructed $\Delta\phi$ angle is required for each event. Since the spectrometer section is about one third of the total detector volume, this cut reduces of approximately the same quantity the event statistics. At this level, experimental and MC1 data show a different reduction rate: due to requirements in the PT reconstruction algorithm, some types of experimental events not simulated by MC1 are rejected. These are particularly noisy events, or events with sparse digits.

$$\begin{aligned}\left(\frac{\mathrm{Rate}_{spect}}{\mathrm{Rate}_{all}}\right)_{\mathrm{OPERA}} &= (28.5 \pm 0.1)\% \\ \left(\frac{\mathrm{Rate}_{spect}}{\mathrm{Rate}_{all}}\right)_{\mathrm{MC1}} &= (33.0 \pm 0.2)\% \qquad (5.2)\end{aligned}$$

The absolute ratio in the spectrometer, when livetime is taken into account, is

$$\frac{(\mathrm{Rate}_{spect})_{\mathrm{OPERA}}}{(\mathrm{Rate}_{spect})_{\mathrm{MC1}}} = (83.4 \pm 0.3)\% \qquad (5.3)$$

Clean PT cut The events with a large number of PT digits potentially dangerous for the muon charge determination are removed. This typically occurs when some drift tubes are fired by secondary particles (δ-rays, showers etc.) and the best χ^2 track could result from a fake tube configuration. In order to evaluate the maximum number of fired tubes/track allowed by geometrical considerations a special version of MC1 switching off delta ray and secondary particle production was run. By naming M and N the number of fired tubes from Monte Carlo simulation and experimental data, respectively, we derived the functional form $M = M(\phi)$, a sixth-degree polynomial shown in Fig. 5.4. $M(\phi)$ was used to rescale the experimental distribution N as $N^{'} = N - M(\phi)$ (Fig. 5.5).

We considered only tracks with $N^{'} < 3\sigma$ (one-sided cut), where σ is the standard deviation of the Gaussian fit to $N^{'}$ for geometrical MC1. We verified by visual inspection that events rejected by the latter cut are characterized by a large number of additional fired tubes in the neighborhood of the correct ones.

Deflection cut A further cut was applied on the $\Delta\phi$ angle. Events having a $\Delta\phi$ smaller or compatible with the experimental resolution were rejected. On the basis

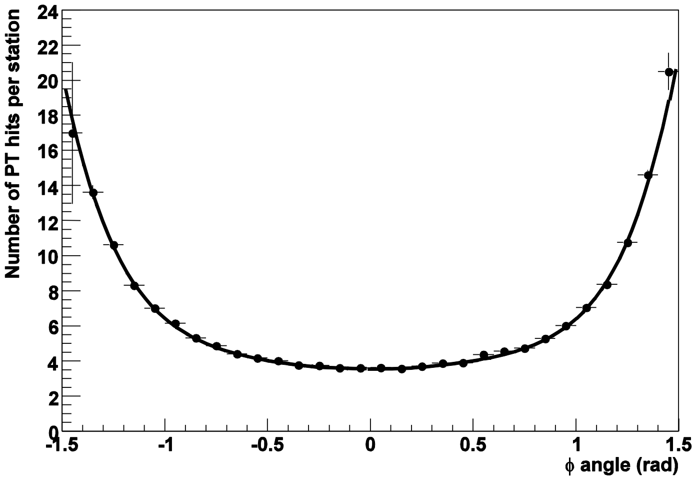

Figure 5.4: The geometrical dependence $M = M(\phi)$ of the number of fired tubes/station on the ϕ angle, obtained by a special MC1 simulation with delta ray and secondary particle production switched off. A sixth-degree polynomial fit is superposed.

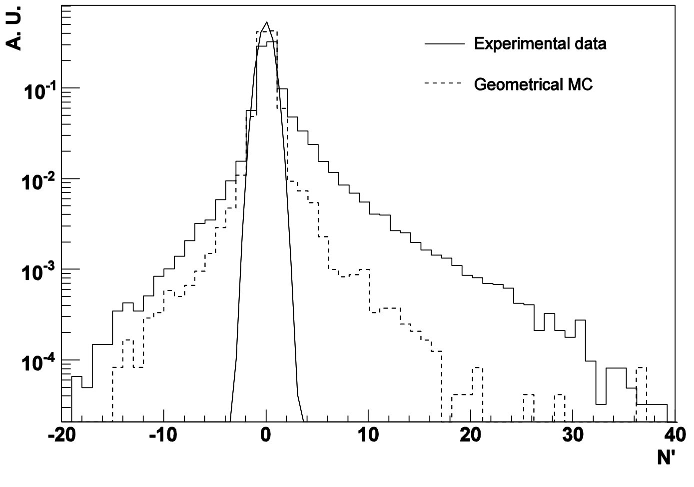

Figure 5.5: Cut on the number of fired PT tubes/station. The rescaled distributions $N^{'} = N - M(\phi)$ for experimental and geometrical MC1 data are shown. A 3σ cut of the Gaussian fit to MC1 events is applied to the rescaled data (see text).

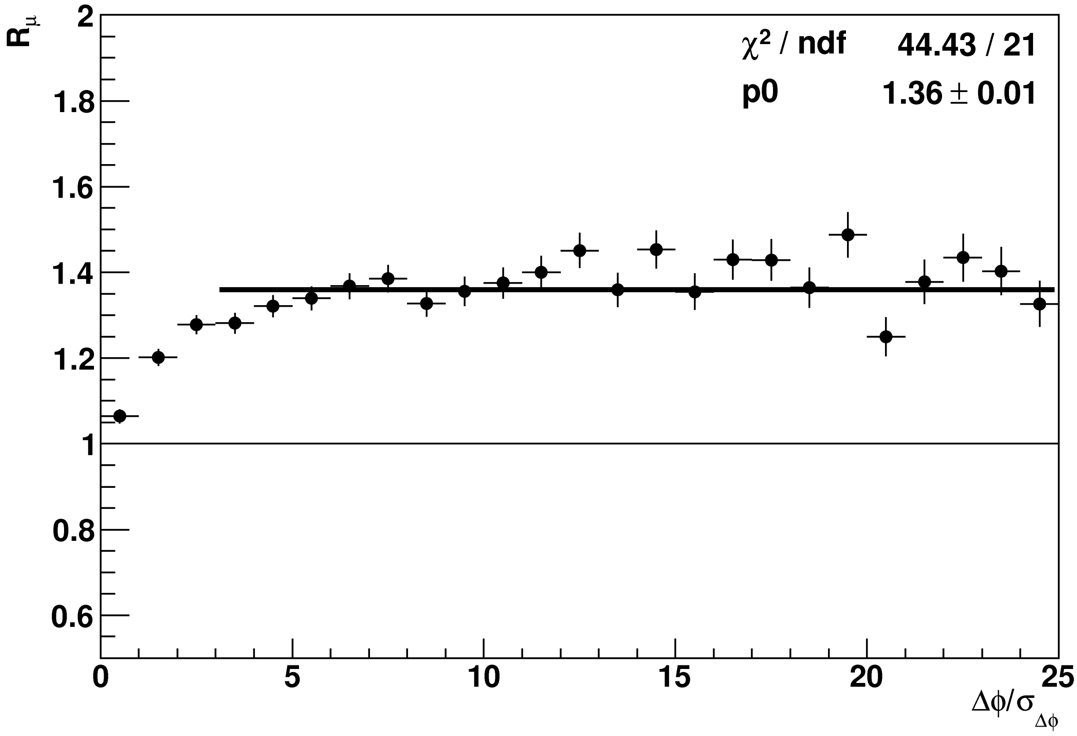

Figure 5.6: Dependence of the measured charge ratio R_μ on the deflection angle expressed in units of experimental resolutions. A cut at $\Delta\phi/\sigma_{\Delta\phi} > 3$ was applied in the data analysis. Note that the fitted value $R_\mu = 1.36 \pm 0.01$ was obtained with the bins indicated in the plot (the first 3 bins have not been used).

of the plot shown in Fig. 5.6 where as expected for small deflection values $R_\mu \to 1$, only events with $\Delta\phi/\sigma_{\Delta\phi} > 3$ were selected. The effect of this cut is visible in Fig. 5.7 in which the $\Delta\phi$ distribution is shown before and after its application. In these plots, experimental data (black points) are plotted with the corresponding Monte Carlo distributions split in the two regions corresponding to positive particles ($q_{true} > 0$) and negative particles ($q_{true} < 0$). The charge-misidentification η corresponds to the overlapping region of the two distributions. Averaged over all the event samples η is reduced from 0.080±0.002 to 0.030±0.001 by this cut. Fig. 5.8 shows the charge misidentification η as a function of the muon momentum, before and after the application of the deflection cut.

The robustness of the deflection cut was tested varying the minimum number of $\sigma_{\Delta\phi}$. The muon charge ratio was computed for different cuts, up to $\Delta\phi/\sigma_{\Delta\phi} > 6$,

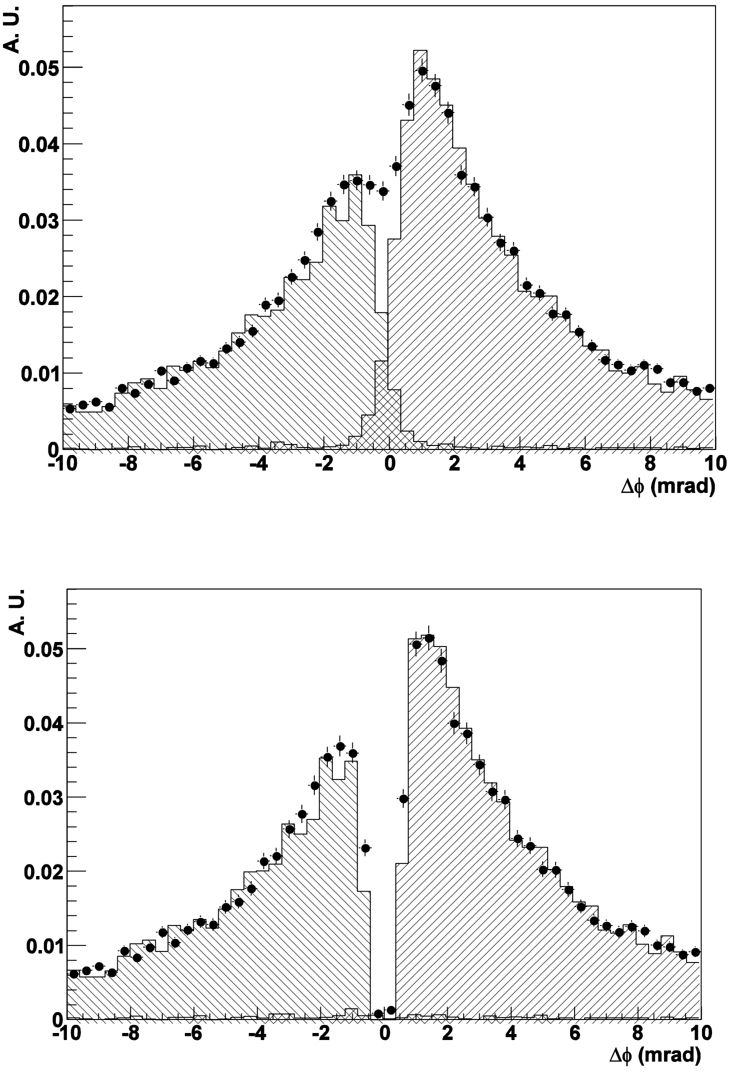

Figure 5.7: Effect of the deflection cut on $\Delta\phi$ distributions reconstructed exclusively from doublets (shown in the range -10 ÷ 10 mrad). On the top panel the distribution before the cut is shown, where the two peaks corresponding to μ^+ and μ^- are already clearly visible. Black points correspond to experimental data, hatched histograms to Monte Carlo simulations, split in the two components $q_{true} > 0$ and $q_{true} < 0$. The same distributions are shown on the bottom panel after the application of the deflection cut $\Delta\phi/\sigma_{\Delta\phi} > 3$. The overlapping region of the two hatched histograms corresponds to the charge-misidentified tracks.

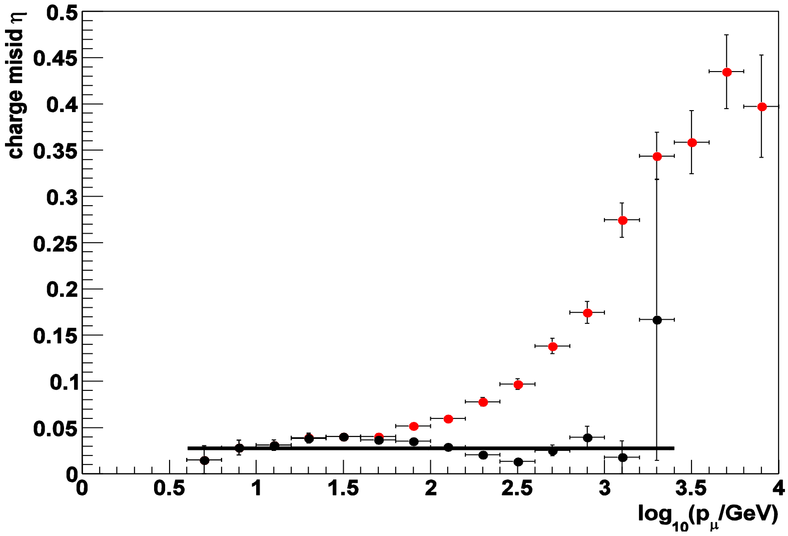

Figure 5.8: Dependence of the charge misidentification on the momentum, with (black points) and without (red points) the deflection cut, obtained from MC1 simulation.

obtaining results compatible within the statistical errors. The cut is directly related to the charge misidentification η that corrects for the charge dilution; thus the charge ratio corrected by η is independent of the chosen cut value.

The source of events with large $\Delta\phi$ angles and reconstructed with wrong charge-sign was investigated. A visual scan of Monte Carlo events confirms the hypothesis that they are due to secondary particles in the neighborhood of the true muon track: if the two tracks are very close, it may happen that the track reconstructed with the best χ^2 is the wrong one. A further selection $\Delta\phi < 100$ mrad was used to reject these fake tracks, with a small impact on the statistics. This last selection affects the sample with $p_\mu \lesssim 5$ GeV/c.

Tab. 5.2 lists the number of events remaining at each stage of the selection process. Note that data and MC1 event rates are absolute (given in day^{-1}) and not normalized one to the other. Also note that the *clean PT* cut has a stronger impact on data reduction and that the effect on the experimental data is different from that of Monte Carlo. This was expected since the percentage of events with PT digits not related to the muon track is intrinsically larger in the experimental data. The *clean PT* cut was tuned in order to be left with a clean data sample at the expense of a considerable loss

	Data			MC1		
	evt/day	f_1	f_2	evt/day	f_1	f_2
Acceptance	1019	100.0%	-	1222	100.0%	-
Clean PT	536	52.5%	-	959	78.5%	-
Deflection	411	40.3%	76.7%	708	58.0%	73.8%
Single μ	398	39.1%	96.9%	673	55.1%	95.1%
Multiple μ	13	1.3%	3.1%	35	2.9%	4.9%

Table 5.2: Progressive reduction of the number of events per day after each selection cut, for data (left) and for MC1 (right). The effect of data reduction is also shown by reporting the fraction of events referred to the original sample (f_1) and to the previous cut (f_2). The total number of experimental events surviving the cuts is 167296.

of statistics.

The progressive effect of the quality cuts on the underground muon momentum spectrum for experimental and for MC1 data is shown in Fig. 5.9. The reduction selects a cleaner sample over a narrower momentum range.

5.3 Underground muon charge ratio

The muon charge ratio was computed separately for single muon events (i.e. event multiplicity $n_\mu = 1$) and multiple muon events ($n_\mu > 1$). Multiple muon events are selected by requiring a muon multiplicity ≥ 2 in both views, with tracks identified and unambiguously merged in 3D space. The underground muon multiplicity selects different primary ranges. For $n_\mu \geq 2$, the average primary cosmic ray energy and chemical composition are different from the typical values of primaries producing single muons underground. Multiple muon bundles originate on average from heavier and more energetic primaries. For primaries heavier than protons the positive charge excess is reduced and so is the muon charge ratio [73]. In this way we can test the dilution of R_μ due to the neutron enhancement in the primary nuclei. A smaller R_μ value is also expected due to kinematical considerations. The selection of high multiplicity events artificially bias the x_F distribution of muon parents towards smaller values, where the charge ratio is smaller (see Sec. 3.3.2). Hence we aslo expect an R_μ reduction from this additional effect.

The measurement R_μ^{meas} has to be unfolded taking into account the charge misidentification probability η. Due to the migration between the positive and the negative charge bins, a large misidentification decreases the R_μ^{meas} value. In general, the mea-

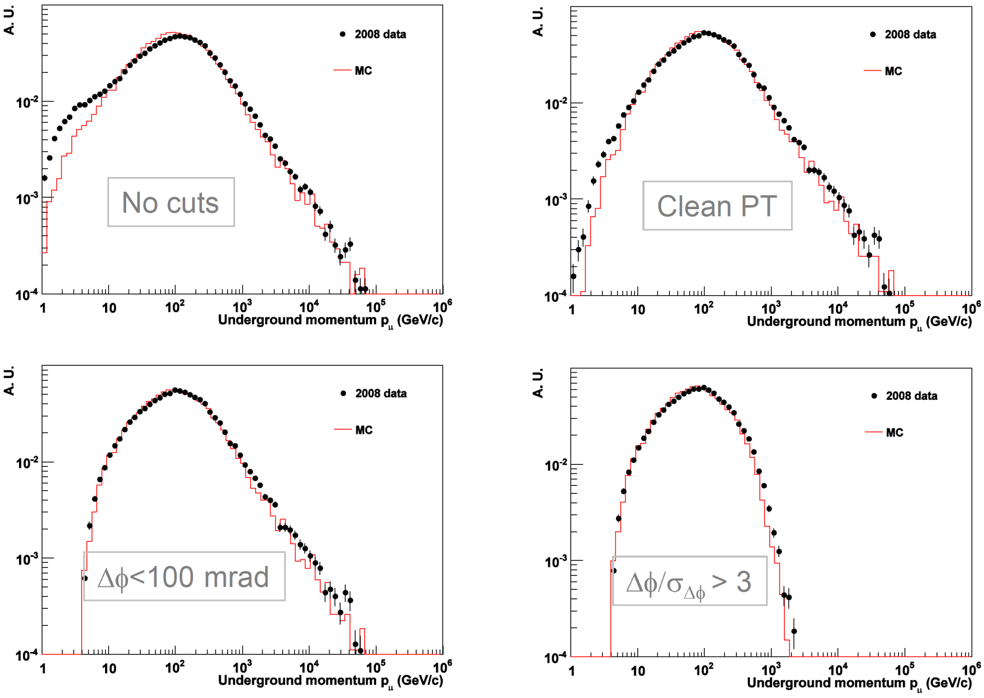

Figure 5.9: Measured muon momentum spectrum at each stage of the selection cuts for experimental data (black points) and MC1 (red line), normalized one to the other. The top left panel shows the spectrum before the cuts, the top right the effect of the *clean PT* cut, the bottom left the low momentum reduction due to the cut $\Delta\phi < 100$ mrad (effective for $p_\mu \lesssim 5$ GeV/c) and the bottom right the effect of the *deflection* cut, suppressing momenta above ∼1000 GeV/c.

sured value R_μ^{meas} is always lower than the "true" value.

We evaluated the charge misidentification η using the MC1. We compute the number of muons with the wrong charge sign over the total number of charge reconstructed muons

$$\eta = \frac{N_{wrong}}{N_{total}} \tag{5.4}$$

In the following Sec. 5.3.1 the unfolding procedure is presented.

5.3.1 Unfolding procedure

Let us call m^{ij} the number of muons with charge i reconstructed with charge j. The total number of *true* positive and negative muons is therefore:

$$\begin{aligned} M^+ &= m^{++} + m^{+-} \\ M^- &= m^{--} + m^{-+} \end{aligned}$$

On the other hand, the total number of *reconstructed* positive and negative muons is:

$$\begin{aligned} \hat{M}^+ &= m^{++} + m^{-+} \\ \hat{M}^- &= m^{--} + m^{+-} \end{aligned}$$

Let us define the charge-misidentification η as:

$$\begin{aligned} \eta^{+-} &= \frac{m^{+-}}{M^+} \\ \eta^{-+} &= \frac{m^{-+}}{M^-} \end{aligned} \tag{5.5}$$

Using a matrix notation, we can express the relationship between $\mathbf{M}$ and $\hat{\mathbf{M}}$ as:

$$\hat{\mathbf{M}} = \mathbf{H}\mathbf{M} \tag{5.6}$$

where

$$\mathbf{H} = \left(\begin{array}{cc} 1-\eta^{+-} & \eta^{-+} \\ \eta^{+-} & 1-\eta^{-+} \end{array} \right) \tag{5.7}$$

Inverting this relation, one has the number of “true” positive and negative muons:

$$\mathbf{M} = \mathbf{H}^{-1}\hat{\mathbf{M}} \tag{5.8}$$

where

$$\mathbf{H}^{-1} = \frac{1}{1-\eta^{+-}-\eta^{-+}} \left(\begin{array}{cc} 1-\eta^{-+} & -\eta^{-+} \\ -\eta^{+-} & 1-\eta^{+-} \end{array} \right) \tag{5.9}$$

The two η values η^{+-} and η^{-+} are obtained from the MC1 simulation. We found that, within the statistical accuracy of the simulation, $\eta^{+-} = \eta^{-+} = \eta$ as one would expect from a charge-symmetric detector. This simplifies the expressions which, in terms of the ratio R, becomes

$$\begin{aligned} R &= \frac{M^+}{M^-} = \frac{(1-\eta)\hat{M}^+ - \eta\hat{M}^-}{-\eta\hat{M}^+ + (1-\eta)\hat{M}^-} = \\ &= \frac{(1-\eta)\hat{R} - \eta}{-\eta\hat{R} + (1-\eta)} \end{aligned} \tag{5.10}$$

where $\hat{R} = \hat{M}^+/\hat{M}^-$.

If $\hat{R}$ is computed with the same Monte Carlo events used to evaluate η, one would obtain the same "true" R value of the starting data sample. If $\hat{R}$ is computed with the experimental reconstructed data, then R is the unfolded experimental value in Eq. 5.12.

The error δR is obtained propagating the errors on $\hat{R}$ and η over Eq. 5.10:

$$\delta R = \frac{\sqrt{(1-2\eta)^2(\delta\hat{R})^2 + (\hat{R}^2-1)^2(\delta\eta)^2}}{[\eta\hat{R} - (1-\eta)]^2} \tag{5.11}$$

It may be pointed out that we did not use any regularization scheme in the unfolding, i.e. statistical fluctuations on $\hat{R}$ are not damped in Eq. 5.10 in order to prevent unphysical spikes in the unfolded R value. This is acceptable in our case since the collected statistics on $\hat{M}^+$ and $\hat{M}^-$ is large enough.

5.3.2 Computation of R_μ

The muon charge is reconstructed and the total number of positive and negative muons surviving the cuts is computed. Tab. 5.3 refers to single muon events where the number of positive and negative muons, their ratio, the charge-misidentification η and the unfolded charge ratio are reported. The η value, defined as the fraction of tracks reconstructed with wrong charge sign, was extracted from the Monte Carlo simulation MC1. Once η is known, the unfolded charge ratio is obtained according to the formula (5.10), i.e.

$$R_\mu^{unf} = \frac{(1-\eta)R_\mu^{meas} - \eta}{-\eta R_\mu^{meas} + (1-\eta)} \tag{5.12}$$

The single muon sample was subdivided into three classes: tracks reconstructed exclusively as doublets, tracks reconstructed exclusively as singlets and as mixed. We verified that the fraction of these classes for experimental data and for Monte Carlo simulation are compatible: 54.8% (doublets), 9.0% (singlets) and 36.2% (mixed) for OPERA data to be compared with 52.5%, 10.0% and 37.5% for Monte Carlo simulation (the errors are $\lesssim 0.5\%$). The final charge ratio value for single muon events, integrated over all the classes, is:

$$R_\mu^{unf}(n_\mu = 1) = 1.403 \pm 0.008 \tag{5.13}$$

where $\eta = (3.0 \pm 0.1)\%$, averaged over all the event samples.

The same procedure was applied to multiple muon events. We selected events with $n_\mu > 1$ and reconstructed the charge of muons crossing the spectrometer section. Events were classified in this category provided that more than one muon was reconstructed

	N_{μ^+}	N_{μ^-}	R_μ^{meas}	η	R_μ^{unf}
Doublets	52210	37279	1.405 ± 0.010	0.0165 ± 0.0012	1.417 ± 0.010
Mixed	33502	24626	1.360 ± 0.011	0.0403 ± 0.0022	1.398 ± 0.013
Singlets	8094	6390	1.27 ± 0.02	0.064 ± 0.005	1.31 ± 0.03

Table 5.3: Final statistics for the underground muon charge ratio. Results are given separately for the three classes of events defined in the text. Errors are statistical only.

n_μ	$\langle A\rangle$	$\langle E/A\rangle_{primary}$	H fraction	N_p/N_n	R_μ^{unf}
=1	3.35±0.09	(19.4±0.1) TeV	0.667±0.007	4.99±0.05	1.403±0.008
>1	8.5±0.3	(77±1) TeV	0.352±0.012	2.09±0.07	1.18±0.03

Table 5.4: Primary cosmic ray information for single and multiple muon events (see text). Reported numbers were obtained with MC2 and with the composition model fitted in [74]. Only statistical errors are quoted. Systematic uncertainties related to the composition model dominate and can be inferred from the cited reference ($\delta\langle A\rangle \simeq 1$). In the last column the measured (and unfolded) charge ratios are given.

in the detector even though only one charge was measured. In other words, the muon multiplicity is used to "tag" events generated by heavier and more energetic primaries. In case of more than one track per event is charge-reconstructed, the charged tracks are treated as all the other ones, i.e. as belonging to independent events.

The charge ratio is $R_\mu^{meas}(n_\mu > 1) = 3451/2957 = 1.17 \pm 0.03$ and the corresponding unfolded value, obtained from Eq. 5.12, is

$$R_\mu^{unf}(n_\mu > 1) = 1.18 \pm 0.03 \tag{5.14}$$

This value is 7.2σ away from the value for single muon events, consistent with the hypothesis of dilution of R_μ due to the neutron enhancement in the primary nuclei.

Tab. 5.4 gives information obtained with the FLUKA full Monte Carlo simulation (MC2, Sec. 3.3.2) on some variables of single muon events and muon bundles in the OPERA detector. In particular, the average primary mass number $\langle A\rangle$, the average primary energy/nucleon $\langle E/A\rangle$, the fraction of Hydrogen nuclei over the total (H fraction), the ratio of protons over neutrons in the primary radiation N_p/N_n and the measured muon charge ratio R_μ^{unf} are given. From this table one can observe that the underground muon multiplicity selects different primary mass and different p/n ratios.

5.4 Systematic uncertainty on R_μ

The main sources of systematic uncertainties in the determination of R_μ^{unf} are related to the alignment accuracy of the PT system and to the determination of the η value.

5.4.1 PT misalignment

The systematic uncertainty due to misalignment effects was evaluated in different ways. A given offset $\Delta\phi \rightarrow \Delta\phi + \delta\phi$ can be directly propagated in the algorithm which computes the charge ratio to evaluate $R_\mu \rightarrow R_\mu + \delta R_\mu$. The $\delta\phi = 0.2$ mrad uncertainty on the alignment accuracy obtained with magnets off (Sec. 4.3) corresponds to $\delta R_\mu = 0.03$. However a more powerful procedure was used to better estimate this systematics. We considered all muon tracks crossing both arms of each spectrometer, thus providing two independent deflection values $\Delta\phi$ per spectrometer for the same muon track. With perfect alignment and neglecting the energy loss the difference $\delta\Delta\phi = \Delta\phi_{arm_1} - \Delta\phi_{arm_2}$ should be peaked at zero. The two distributions, one for each spectrometer, are shown in Fig. 5.10 together with a Gaussian fit to the central part of the distributions, where the effects of muon energy loss in the magnet iron are negligible. The two peaks are at 0.08 mrad and -0.07 mrad respectively, ∼2 standard deviations away from zero. A misalignment of 0.08 mrad produces an error on the charge ratio $\delta R_\mu \simeq 0.015$. We quote this number as the limiting alignment accuracy of each doublet with respect to the other. This number is conservative since it assumes that all four arms are affected independently from the same uncertainty. In reality only the the outer two doublets of each magnet contribute to this error, since a given offset in the central doublet cancels the systematic uncertainty for $\Delta\phi_{arm_1}$ and $\Delta\phi_{arm_2}$.

5.4.2 Charge misidentification probability

The charge misidentification η was previously estimated using Monte Carlo simulations. As already discussed the value is larger than what is expected from multiple scattering alone. The difference is ascribed to the inclusion of spurious effects, such as the production of secondary particles near the muon trajectory, timing errors, and other second order effects not reproducible with the Monte Carlo program. Therefore we expect that the systematic uncertainty on η is one-sided, being $\eta_{real} \geq \eta_{MC}$. To estimate this difference η was evaluated using experimental data for a subsample of events. We considered all muon tracks crossing both arms of each spectrometer, which provide two independent deflections $\Delta\phi$ of the same muon track. In this case, the probability that the two deflection angles have opposite sign is $p = 2\eta(1-\eta)$ and therefore

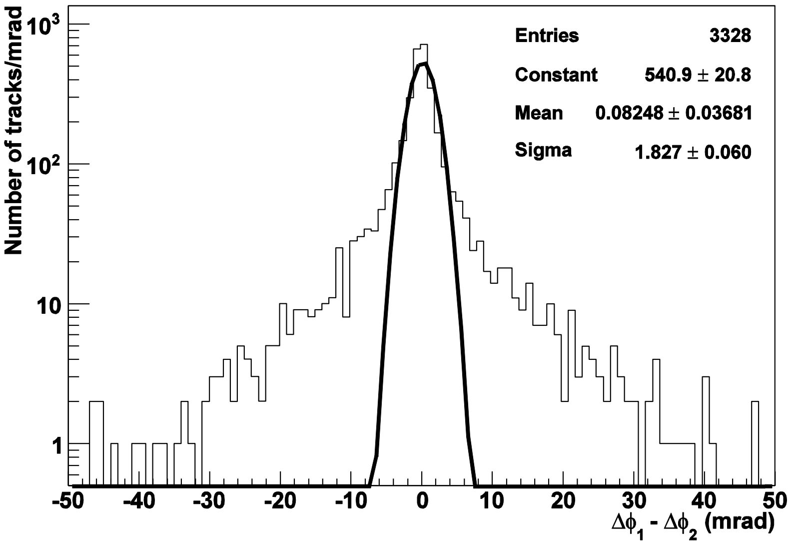

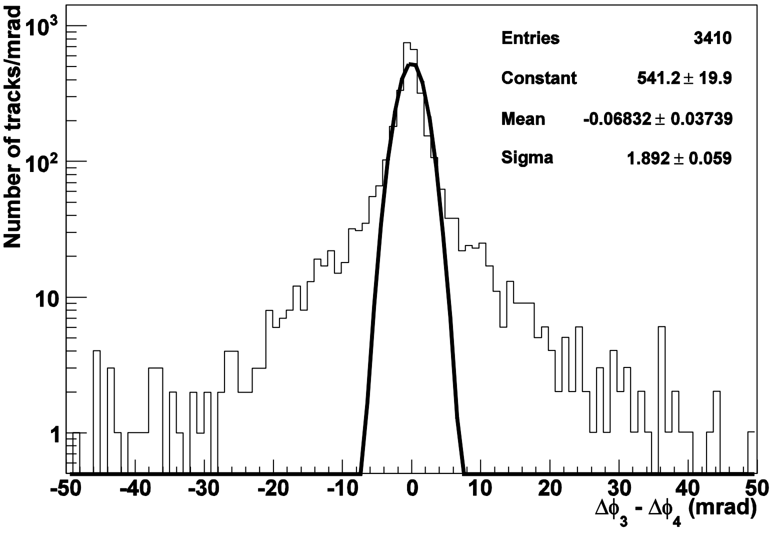

Figure 5.10: Two-arm test. Distributions of the difference of the deflection angles for tracks crossing both arms of one spectrometer: SM1 (top) and SM2 (bottom). In each plot we show the fit of the central part of the distributions to a Gaussian function.

$\eta = 1 - \sqrt{1-2p}$. This formula neglects the correlation between the two $\Delta\phi$ angles, since they are built using a common track (the one in between the two arms). The correct $\eta(p)$ relation was derived using a Monte Carlo simulation applied to the experimental and simulated data. It was found for the case of doublets $\eta_{data} = 0.018 \pm 0.002$ and $\eta_{MC} = 0.012 \pm 0.002$. Considering doublets and mixed configuration together, we found $\eta_{data} = 0.026 \pm 0.002$ and $\eta_{MC} = 0.019 \pm 0.002$. The difference $\delta\eta = 0.007$ was used as an estimate of the systematic uncertainty on η which corresponds to $\delta R_\mu = 0.007$.

The final systematic error is taken as the quadratic sum of its contributions and it is assumed to be the same for single and for multiple muon events:

$$\delta R_\mu^{unf}(\text{syst.}) =^{+0.017}_{-0.015} \tag{5.15}$$

5.4.3 Consistency tests on systematics

In the following, we present some consistency checks to test the systematic error on R_μ.

R_μ as a function of the azimuth angle φ

The effect of PT misalignment is visible in the R_μ distribution as a function of the azimuth angle φ. The R_μ distribution is very sensitive to small biases in the $\Delta\phi$ measurement due to z or x displacement of the PT system, and the effect is amplified by the azimuth distribution. An *intra-doublet* displacement of 0.5 cm along the z-axis (Sec. 4.3) gives a R_μ sinusoidal pattern with an amplitude of 0.25 in the R_μ value. Fig. 5.11 shows the charge ratio measured by each magnet arm and the total measurement as a function of φ. We do not expect an *a priori* constant value of R_μ, since each azimuth φ region reflects a different kinematic region for the surface energy, due to the mountain overburden configuration. If there is a physical dependence of the charge ratio on the surface muon energy, this could lead in principle to an effect in the R_μ versus φ distribution.

A further test which also incorporates local effects consists in comparing the values R_μ^i (i=1,...,4) in each magnet arm. The average difference from the mean value $\sum_i |R_\mu^i - \bar{R}_\mu|/4 = 0.016$ is within the statistical accuracy of each $\delta R_\mu^i = 0.018$.

R_μ stability as a function of data taking

The measurement stability over detector livetime is checked and shown in Fig. 5.12. The three Runs have compatible values that remain constant within the statistical

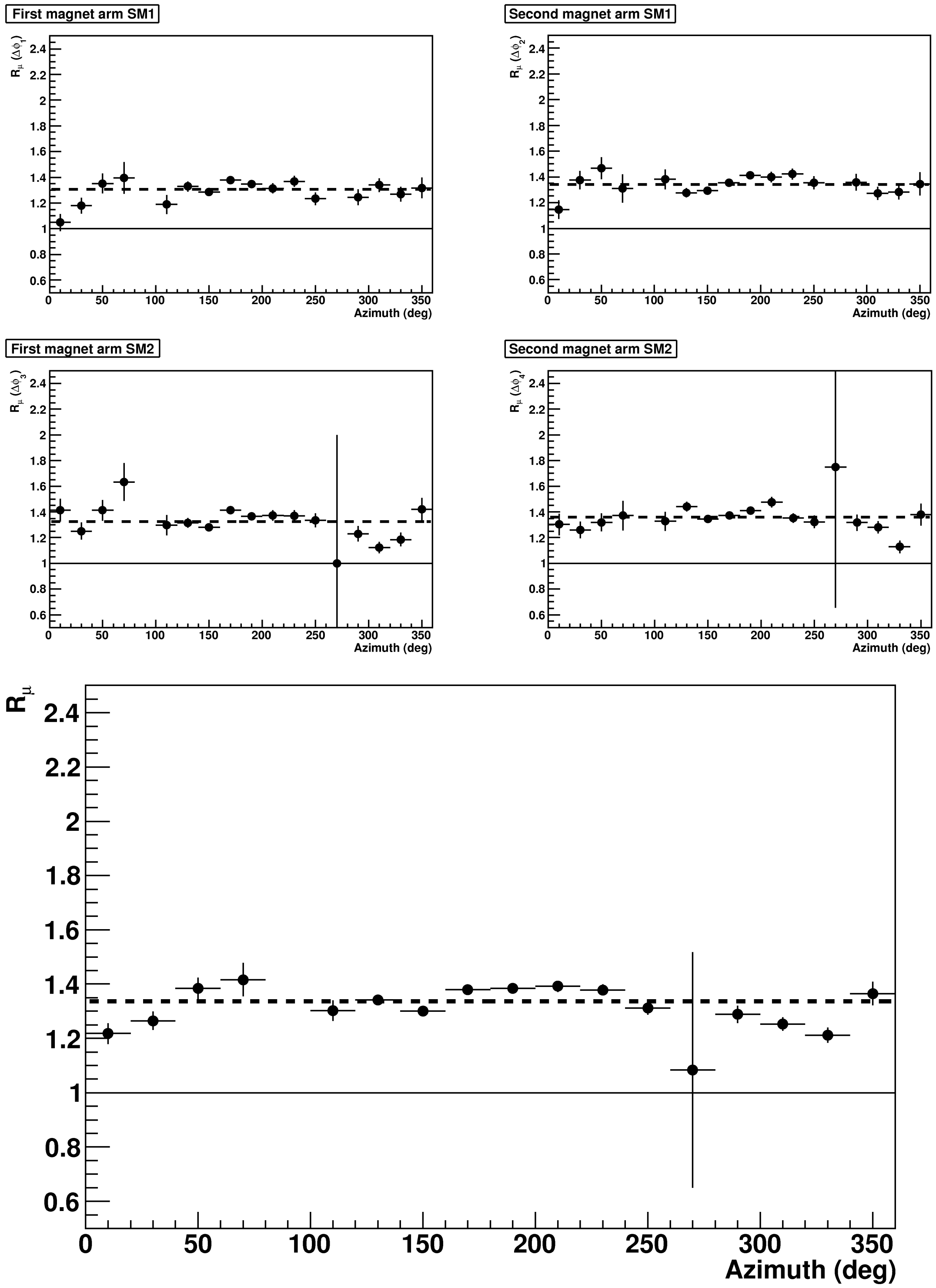

Figure 5.11: Measured charge ratio as a function of the azimuth φ in each magnet arm (top panel) and averaged over all the measurements (bottom panel).

accuracy.

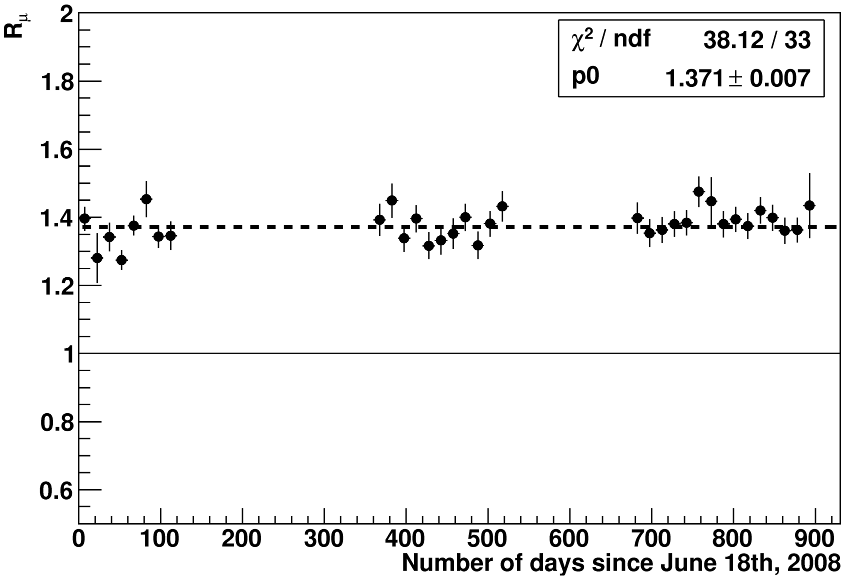

Figure 5.12: Measured charge ratio as a function of the data taking time. The Physics Runs are separated by the CNGS shutdown, where all the OPERA sub-detectors except the TTs are switched off. The R_μ value is constant over the three years of data taking.

Inverted magnet polarity

A consistency check exploited a small data sample (∼9 days during the 2008 Run and ∼7 days during the 2010 Run) obtained after inverting the polarity of the magnetic field. Running with inverted magnetic polarity could in principle cancel the systematic error related to misalignment effects. The result is $R_\mu^{inverted} = 1.35 \pm 0.05$, corresponding to the unfolded value $R_\mu^{inverted} = 1.38 \pm 0.05$. Even if the statistical error is larger than the systematic error quoted above, the result is in good agreement with the value obtained with standard polarity.

Magnet off

A further consistency check exploited a period of data taking with the magnetic field switched off. Analyzing the small data sample (∼13 days during the 2008 Run and ∼10 days during the 2010 Run), we found a charge ratio $R_\mu^{off} = 1.05 \pm 0.03$, consistent with the expected $R_\mu^{off} = 1$.

5.5 R_μ as a function of underground muon momentum p_μ

The underground muon momentum p_μ was computed using Eq. 4.19. The muon charge ratio as a function of p_μ is shown in Fig. 5.13, where the widths of the horizontal error bars correspond approximately to the (average) muon momentum resolution. A linear fit in the range (5,500) GeV/c

$$R_\mu(p_\mu) = a_0 + a_1 \log_{10}[p_\mu/(\mathrm{GeV/c})] \tag{5.16}$$

gives $a_0 = 1.36 \pm 0.03$ and $a_1 = 0.029 \pm 0.018$ with $\chi^2/dof = 3.9/12$. The data are also compatible with the hypothesis of a constant charge ratio, since the fit to a constant in the same range yields $a_0 = 1.409 \pm 0.008$ with $\chi^2/dof = 6.4/13$ and therefore $\Delta\chi^2/dof = 2.48/1$ (corresponding to ~1.6 sigma). The high energy behaviour of R_μ will be discussed in the next Chapter.

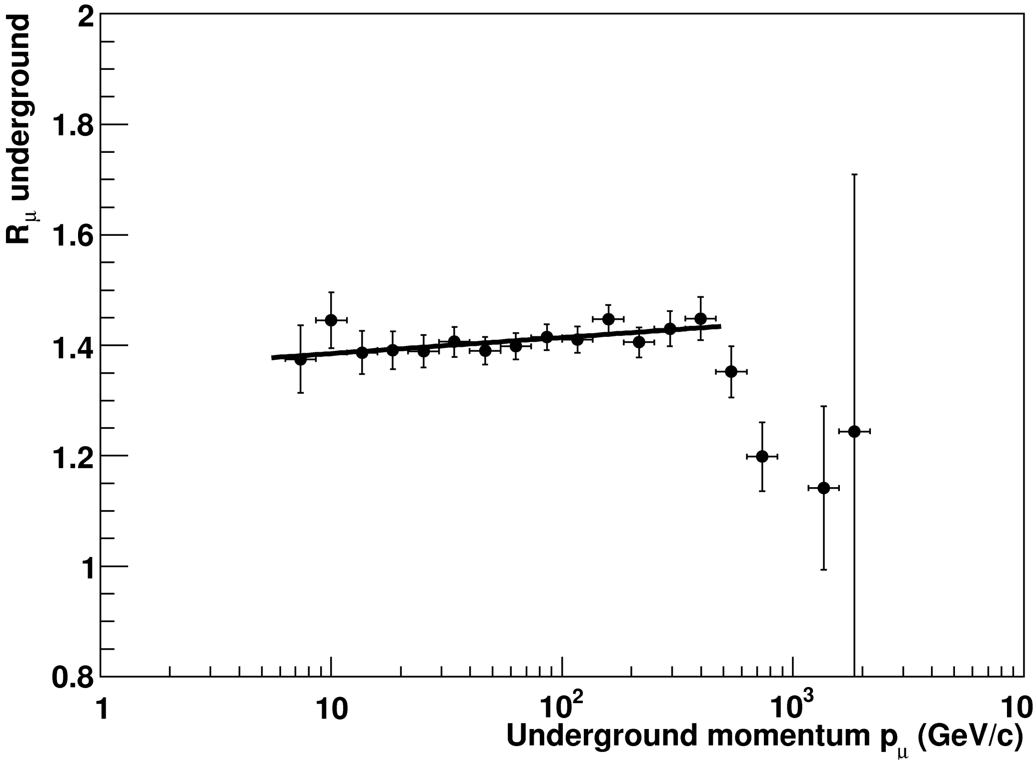

Figure 5.13: Measured charge ratio of underground muons as a function of the reconstructed muon momentum. Data points below ~5 GeV/c and above ~1000 GeV/c are suppressed by the cut on $\Delta\phi$. A fit of the form $R_\mu(p_\mu) = a_0 + a_1 \log_{10}[p_\mu/(\mathrm{GeV/c})]$ in the range (5,500) GeV/c is superimposed to the data.

Chapter 6

R_μ as a function of surface muon energy

In this Chapter we present the analysis of the muon charge ratio as a function of the surface muon energy, discussing the physical implication of the result. The dependence of R_μ on the surface muon energy $\mathcal{E}_\mu$ is described by the parameterization of Eq. 1.28. The approximate expression of the surface muon spectrum can be used to derive a simplified model of the atmospheric muon charge ratio, known as "πK" model. This model predicts a rise in the charge ratio as a function of the "vertical surface energy" $\mathcal{E}_\mu \cos\theta^*$, according to the increasing kaon contribution. A crucial point is the estimation of the surface muon energy $\mathcal{E}_\mu$ from the underground residual energy E_μ and the rock thickness crossed by the muon to reach the detector level.

6.1 Surface muon energy estimation

The muon energy at the surface ($\mathcal{E}_\mu$) is directly related to the underground residual energy ($E_\mu \simeq p_\mu$) and to the rock amount crossed by the muon to reach the detector level. In fact, the energy loss of high energy muons in the rock is usually expressed as

$$-\frac{dE}{dh} = \alpha(E) + \beta(E)E \tag{6.1}$$

where h is the rock depth while the two energy-dependent parameters α and β are the contributions of the ionization energy loss and the radiative processes, respectively. Eq. 6.1 can be integrated to obtain the approximate formula

$$\mathcal{E}_\mu = (E_\mu + \alpha/\beta)e^{\beta h} - \alpha/\beta \tag{6.2}$$

which connects the surface and underground muon energies. However, Eq. 6.2 is valid only on average. The “resolution” $d\mathcal{E}_\mu = \mathcal{E}_\mu^{rec} - \mathcal{E}_\mu^{true}$ is dominated by the statistical fluctuations due to the discrete processes described by the term β [63]. We evaluated $\mathcal{E}_\mu$ with the full Monte Carlo simulation MC2 to build the table $\mathcal{E}_\mu = f(h, p_\mu)$. For this purpose the code MC2 was used since it contains a detailed description of the muon flux at the surface and the muon transport in the Gran Sasso rock.

The (h, p_μ) plane was divided into 10×10 equally-spaced bins. Fig. 6.1 shows the energy distribution in one (h, p_μ) bin. At this point we followed two approaches to estimate the best $\mathcal{E}_\mu$ value representing the matrix bin. In the first approach, the average $\langle\mathcal{E}_\mu\rangle$ value was computed in each bin. The binning was chosen coarse enough to have a large statistical sample in each bin without affecting the resolution $d\mathcal{E}_\mu$, which

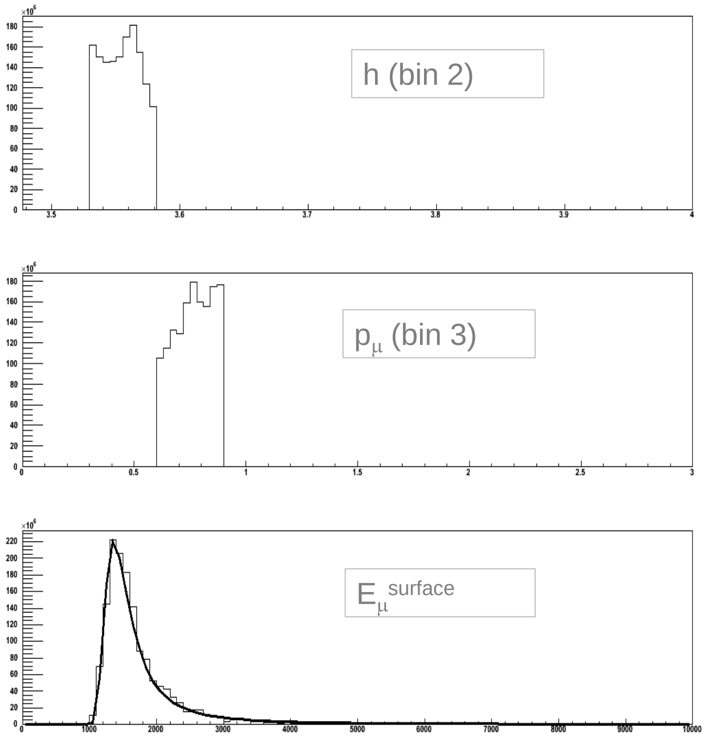

Figure 6.1: An example of a bin in the table $\mathcal{E}_\mu = f(h, p_\mu)$. The first two plots refer to the h and p_μ populations in the bin (2,3), the lower plot is the distribution of the relative MC2 true $\mathcal{E}_\mu$.

is of the order of 0.15 in logarithmic scale [24].

In the second approach, we take the most probable value (MPV) of the Landau distribution of the surface energy in each bin. This is the approach followed in the analysis presented in this thesis. Taking the MPV instead of the "linear" average value allows to have a better resolution and residuals well centered. Using the mean value, the reconstructed energy is systematically overestimated and the residuals are centered on a value below zero.

Since some (h, p_μ) bins are less populated, especially the ones with low p_μ and high h, we interpolated the table $\mathcal{E}_\mu = f(h, p_\mu)$ with the 3D surface shown in Fig. 6.2 where the statistical sample is large. Then we extrapolated the $\mathcal{E}_\mu$ values in the bins where the statistical uncertainty would have been larger with the fixed value procedure.

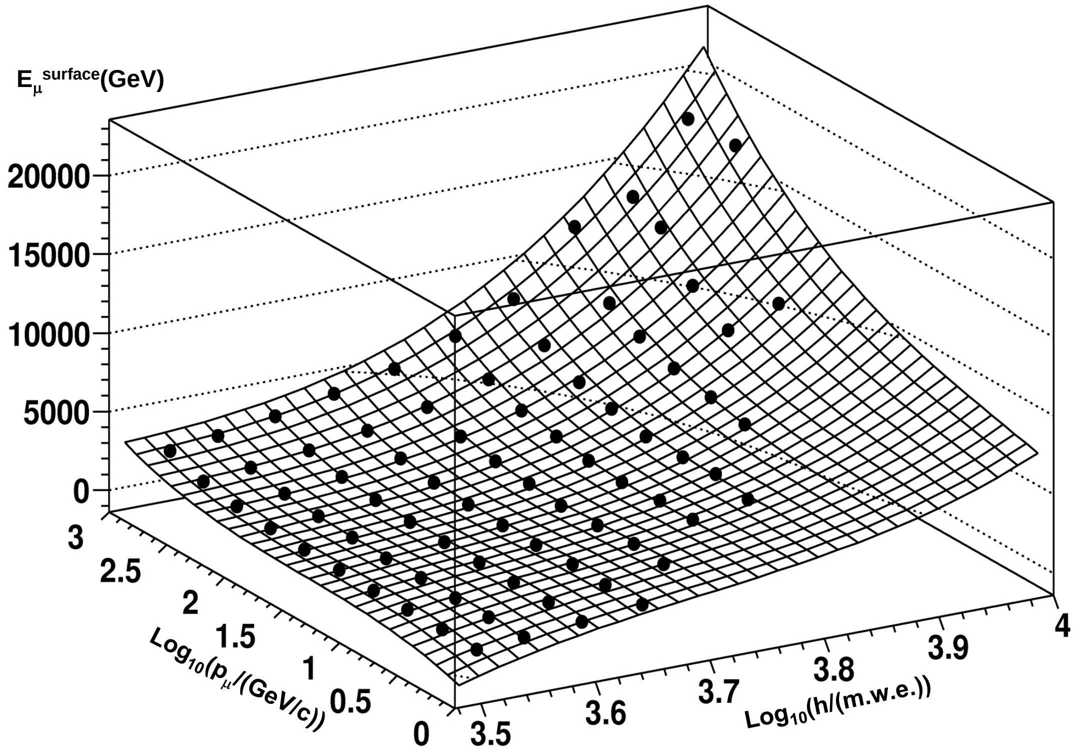

Figure 6.2: The built $\mathcal{E}_\mu = f(h, p_\mu)$ table. The 3D surface interpolates the MPVs in each (h, p_μ) bin.

The resulting energy residuals are again Landau distributed (Fig. 6.3) and well centered around zero. The RMS yields the mean energy resolution achieved $\delta(\log \mathcal{E}_\mu) \sim 0.13$ in logarithmic scale. The correlation between $\mathcal{E}_\mu^{truth}$ and $\mathcal{E}_\mu^{rec}$ is shown in Fig. 6.4. With the method explained, we obtained a good performance in the reconstruction of

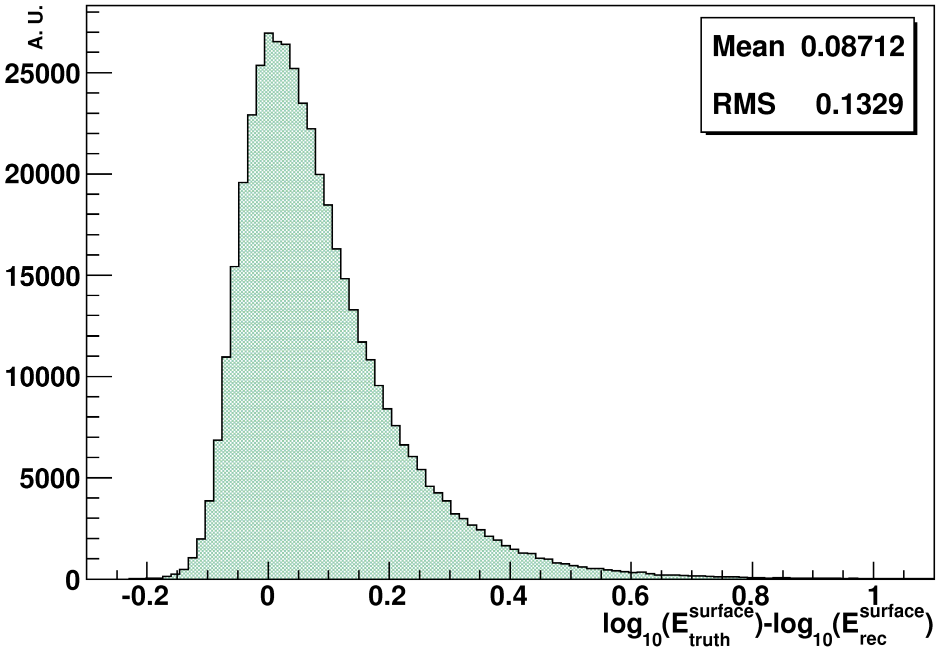

Figure 6.3: The residual distribution $\mathcal{E}_\mu^{truth} - \mathcal{E}_\mu^{rec}$. The RMS yields the mean energy resolution achieved $\delta\mathcal{E}_\mu \sim 0.13$ in logarithmic scale.

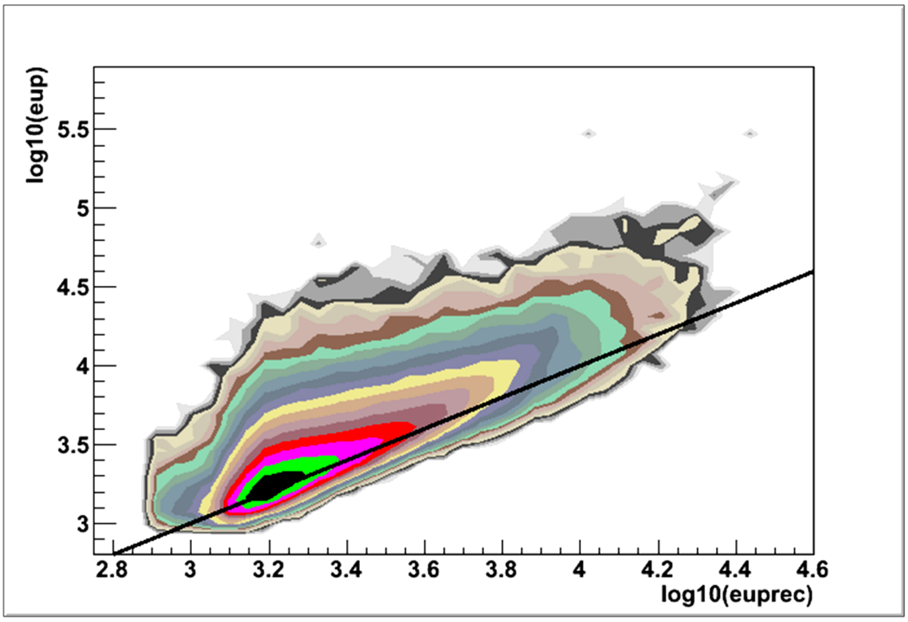

Figure 6.4: The correlation between $\mathcal{E}_\mu^{truth}$ and $\mathcal{E}_\mu^{rec}$. A line is drawn for correlation equal to one. The reconstructed surface energy shows a linear behavior with respect to the true surface energy.

the surface muon energy.

6.2 Muon charge ratio as a function of $\mathcal{E}_\mu \cos\theta^*$

The surface muon charge ratio was computed as a function of the variable $\langle\mathcal{E}_\mu\rangle\cos\theta^*$ binned according to the resolution. As introduced in Chapter 1, the correct variable to describe the evolution of the charge ratio is the product $\mathcal{E}_\mu \cos\theta^*$, the "vertical surface energy" [23]. In this variable the contributions from the different meson parents of the atmospheric muons are discriminated.

Using MC2 the proper binning was computed. For the available statistics in $\mathcal{E}_\mu \cos\theta^*$, the sample was divided in 10 bins in logarithmic scale, shown in Fig. 6.5. The vertical surface energy range covered in $\log(\mathcal{E}_\mu \cos\theta^*)$ is [2.9, 4.2] (≡[800 GeV, 16 TeV]). The bin width is 0.13 in logarithmic scale.

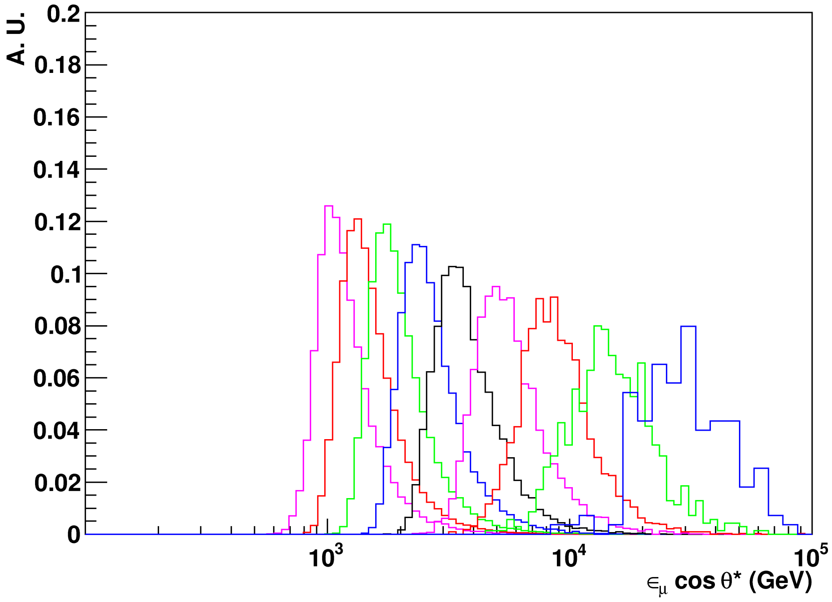

Figure 6.5: The bins selected for the computation of the muon charge ratio at the surface. The true momentum population in each bin is obtained using MC2.

Finally, the experimental values were corrected in each bin for the corresponding charge misidentification. The surface muon charge ratio as a function of $\langle\mathcal{E}_\mu\rangle\cos\theta^*$ is shown in Fig. 6.6 with black points, for single muon events only. OPERA data cover six bins in logarithmic range [2.9, 3.68].

Bin	$\mathcal{E}_\mu \cos\theta^*$ range (GeV)	$\langle \mathcal{E}_\mu \cos\theta^* \rangle$ (GeV)	N_{μ^+}	N_{μ^+}	R_μ^{unf}	δR_μ^{unf}(stat)	δR_μ^{unf}(sys) (%)
1	794 – 1072	922	22620	16683	1.37978	0.015	0.4
2	1072 – 1445	1245	44522	32016	1.4251	0.011	0.5
3	1445 – 1950	1679	16290	11682	1.42361	0.019	1.3
4	1950 – 2630	2265	5039	3767	1.35749	0.031	4.3
5	2630 – 3548	3055	1504	1244	1.22774	0.051	3.1
6	3548 – 4786	4121	393	334	1.19302	0.097	4.0

Table 6.1: Main information for the five bins in $\mathcal{E}_\mu \cos\theta^*$. From left to right: the energy range and average value, the number of muons reconstructed with positive and negative charges, the unfolded charge ratio, the statistical and systematic errors.

The muon charge ratio value rises according to the "πK" model until $\sim$ 2 TeV, then suddenly decreases to the value $R_\mu = 1.19 \pm 0.10$ in the last OPERA bin at about 4 TeV.

Tab. 6.1 gives some information for each of the six bins considered: the energy range and average value, the statistical sample, the unfolded charge ratio, the statistical and systematic errors. The latter were evaluated computing in each bin the two contributions discussed in Sec. 5.4.

In Fig. 6.6 are shown for comparison the data from other experiments for which we could recover information on the $\mathcal{E}_\mu \cos\theta^*$ variable. For the low energy region we took data from Ref. [75] and Ref. [76] (we choose data points with uncertainties δR_μ<0.05) while in the high energy region the data are from Ref. [77] and Ref. [78]. For the latter, since the angular information were not provided in the paper, we plotted the R_μ integrated value in correspondence of the $\mathcal{E}_\mu \cos\theta^*$ value given in Ref. [79]. We also report a recent result from Ref. [80] where the vertical muon charge ratio is given in the range 1-3 TeV (average value 1.3 TeV).

Finally, we fit our data to Eq. 1.28, using a procedure similar to what is described in Ref. [78]. We rewrite Eq. 1.28 in the form:

$$\phi_{\mu^\pm} \propto \frac{a_\pi f_{\pi^\pm}}{1 + b_\pi \mathcal{E}_\mu \cos\theta^*/\epsilon_\pi} + R_{K\pi} \frac{a_K f_{K^\pm}}{1 + b_K \mathcal{E}_\mu \cos\theta^*/\epsilon_K} \tag{6.3}$$

where $R_{K\pi} = Z_{NK}/Z_{N\pi}$ and $f_{\pi^+} = 1 - f_{\pi^-} = Z_{N\pi^+}/Z_{N\pi}$ (and similarly for kaons). f_{π^+} and f_{K^+} were left free to vary while we fixed the kinematic parameters $a_\pi = 0.674$, a_K $= 0.246$, $b_\pi = 1.061$, $b_K = 1.126$ and the fraction of kaons over pions in the atmosphere $R_{K\pi} = 0.149$ [2]. The fit of $R_\mu = \phi_{\mu^+}/\phi_{\mu^-}$ takes into account data from [75] and [76]

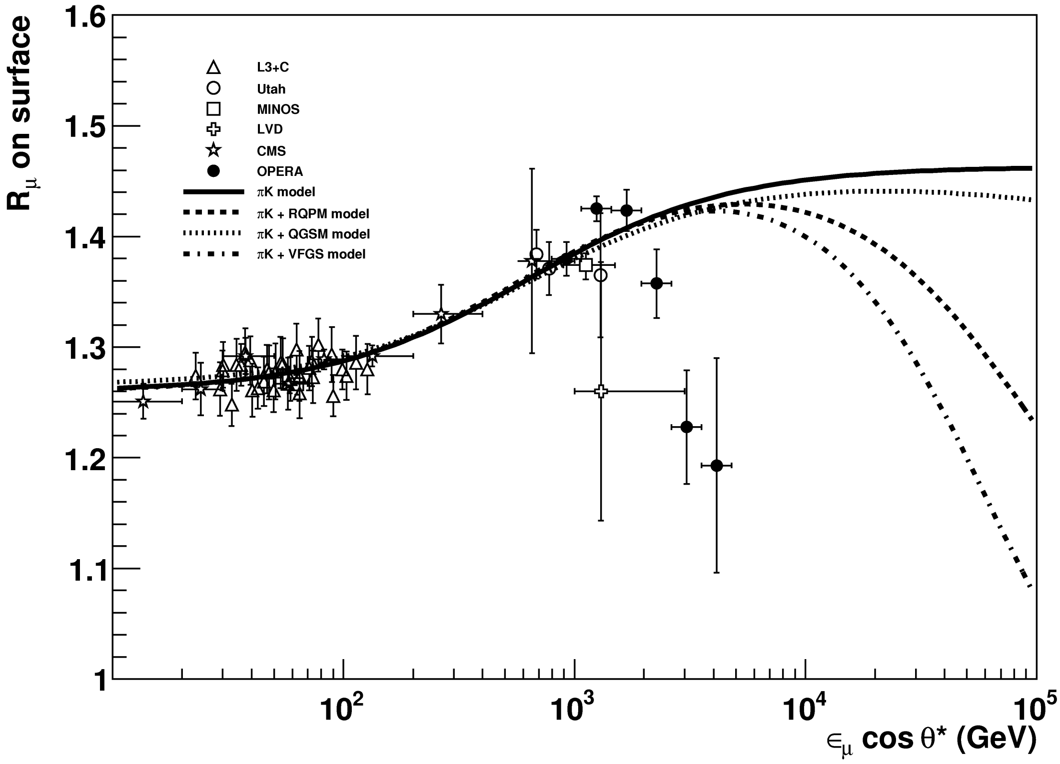

Figure 6.6: R_μ values measured by OPERA in bins of $\mathcal{E}_\mu \cos\theta^*$ (black points). Also plotted are the data in the low energy region from MINOS-ND [75] and L3+C [76] and in the high energy region from Utah [77], MINOS [78] and LVD [80] experiments. The result of the fit of OPERA and L3+C data to Eq. 6.3 is shown by the continuous line. The dashed, dotted and dash-dot lines are, respectively, the fit results with the inclusion of the RQPM, QGSM [81] and VFGS [82] models for prompt muon production in the atmosphere.

for the low energy region and data from this work at higher energies. The fit yields the values $f_{\pi^+} = 0.5484 \pm 0.0013$ and $f_{K^+} = 0.721 \pm 0.010$ which correspond to a ratio $R_\pi = Z_{N\pi^+}/Z_{N\pi^-} = 1.2146 \pm 0.0006$ and $R_K = Z_{NK^+}/Z_{NK^-} = 2.583 \pm 0.023$ for pions and kaons respectively. The result of the fit is shown in Fig. 6.6 as a continuous line.

The contribution of the prompt muon component to R_μ was evaluated for three different charm production models: the phenomenological non-perturbative models RQPM and QGSM [81] and the semi-empirical model from Volkova *et al.* [82]. In Ref. [81] the prompt muon flux and charge ratios are parametrized as a function of the muon energy. The results of the fit extended to include the prompt contribution as predicted by these models are shown in Fig. 6.6. The pion and kaon charge ratios obtained from the fit are unchanged within the statistical errors.

The muon charge ratio decrease above 2 TeV was investigated. As seen in the previous Chapter, two are the main systematic error sources: the PT alignment accuracy and the determination of the η value. In the next Section, we check the possible systematics related to the misidentification evaluation. We compute the surface muon charge ratio as a function of $\langle \mathcal{E}_\mu \rangle \cos\theta^*$ using only experimental data to extract the η value in each bin.

6.2.1 Charge misidentification from experimental data

Since the present statistics is large enough to compute the charge ratio using only doublets, the charge misidentification is extracted directly from experimental data. Dropping the unfolding based on MC1 data we eliminate a possible source of systematic uncertainty (Sec. 5.4). The "bi-arm" test, described in the previous Sec. 5.4, provides the probability that the two deflection angles $\Delta\phi$ in the same magnet have opposite sign, $p = 2\eta(1-\eta)$. Inverting the relation the misidentification $\eta = 1 - \sqrt{1-2p}$ is obtained for doublet configurations. Considering the correlation between the two $\Delta\phi$ angles, the correct $\eta(p)$ relation was derived using a Monte Carlo simulation applied to experimental data. Fig. 6.7 shows the experimental η as a function of $\mathcal{E}_\mu \cos\theta^*$ in the

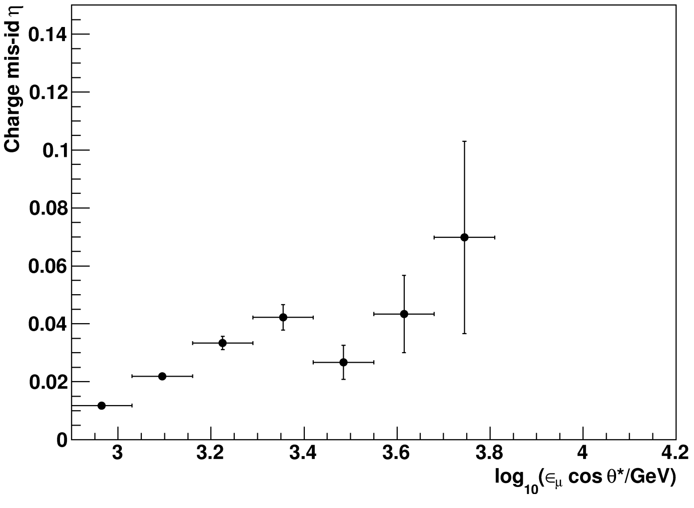

Figure 6.7: The charge misidentification η extracted from experimental data is computed in each OPERA bin in $\mathcal{E}_\mu \cos\theta^*$.

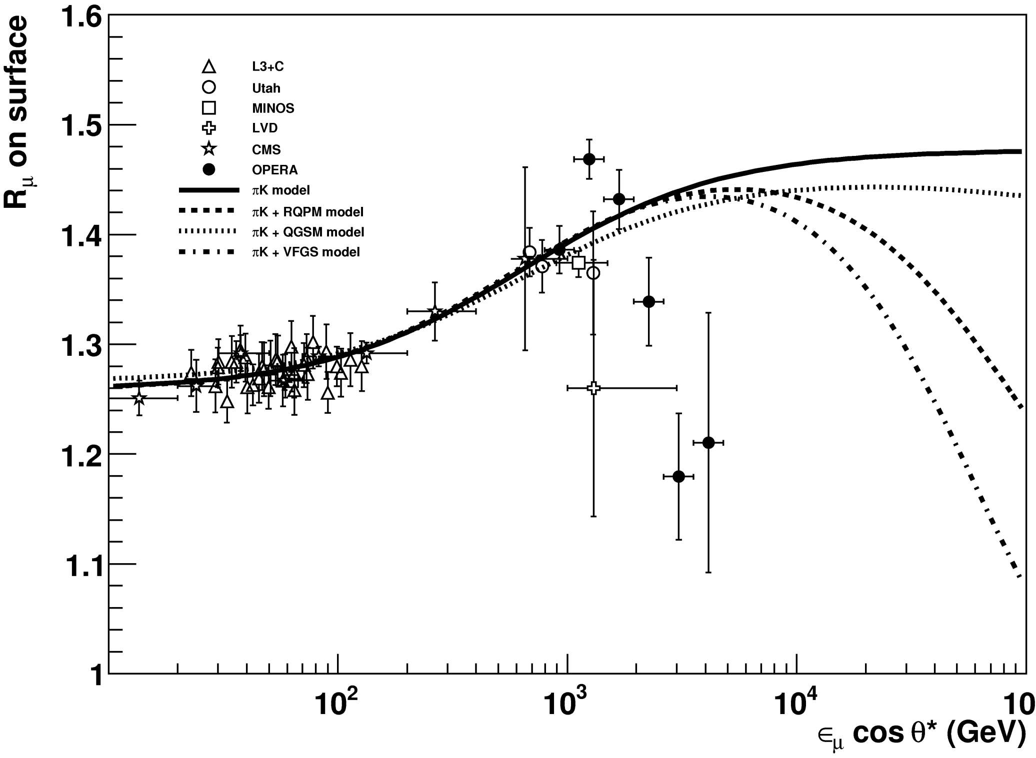

Figure 6.8: R_μ values measured by OPERA in bins of $\mathcal{E}_\mu \cos\theta^*$ (black points). The R_μ values are unfolded using the misidentification extracted from experimental data. The data from others experiments are the same as in Fig. 6.6.

bins selected for R_μ measurement.

The result is shown in Fig. 6.8. The behaviour of the muon charge ratio at high energy is similar to the one obtained using the MC1 misidentification probability η. This ensures that the effect is not due to an underestimated systematic error on η.

The hypothetical physical explanations of the decreasing muon charge ratio at high energy (above 2 TeV) can be ascribed to three different scenarios.

A first hypothesis demands a fast increase of the neutron/proton ratio in the primary beam as a function of the energy. As seen for multiple muon bundles, the increase of the average primary mass number $\langle A \rangle$, i.e. the decrease of the fraction of Hydrogen nuclei over the total (H fraction), leads to a reduced muon charge ratio. This explanation requires a change in the primary chemical composition, i.e. a significant difference in the power spectra of protons with respect to heavier nuclei in the 1-10 TeV energy range. This idea is supported by recent data from the PAMELA and ATIC Collaborations

[83, 84].

An alternative explanation relies on the breakup of the Feynman scaling above TeV energies in the fragmentation region, where no experimental data exist. The spectrum weighted moments Z_{ij} (Eq. 1.16) determine the uncorrelated fluxes of energetic particles in atmosphere. Due to the $(x_L)^{\gamma-1}$ factor, the uncorrelated fluxes depend on the behavior of the inclusive cross section only in the forward fragmentation region, i.e. $x_L \gtrsim 0.05$. Even a moderate violation of the Feynman scaling, i.e. a slight dependence of the inclusive cross section on the center-of-mass energy, can lead up to a decrease in the muon charge ratio.

Finally, charm production could play an important role in the charge ratio at very high energies even if most of the available predictions agree on a crossover energy of the order of $\sim$100-1000 TeV. We observe that our measurement lies in the region where the charmed particle production may start to give an observable contribution to the muon charge ratio. A larger statistical sample or an experimental measurement with a new detector at very large depths could shed light on the region $\mathcal{E}_\mu \cos\theta^* \sim 10$ TeV.

Conclusions

In this thesis, the measurement of the atmospheric muon charge ratio $R_\mu = N_{\mu^+}/N_{\mu^-}$ with the spectrometers of the OPERA detector is presented. The measurement is performed for the first time at the LNGS depth ($\sim$3800 m.w.e.), thus investigating the TeV surface energy range. Thanks to the Gran Sasso overburden configuration, to the instrumented dipolar magnets and to the acceptance of the detector, we measured R_μ in the highest energy region.

The atmospheric muon charge ratio allows to study both high energy hadronic interactions in kinematic regions not yet explored at accelerators and the nature of the primary cosmic rays.

The analysis relies on data taken during the CNGS Physics Runs 2008, 2009 and 2010, for a total of 1454057 muon events, corresponding to about 407 days of livetime. Since the primary physics goal of the OPERA experiment is to observe neutrino oscillation, we used the detector differently from what it was conceived for. The OPERA standard reconstruction software was complemented with a set of dedicated software tools developed for cosmic ray events. A key point for charge reconstruction at high energies is the accuracy of the drift tube station alignment, therefore a refined detector alignment was performed using cosmic ray tracks. A 0.1 mm accuracy was achieved allowing to reach a systematic error at the level of the statistical one.

The muon charge ratio was computed for single and for multiple muons separately. Multiple muon bundles originate on average from heavier and more energetic primaries. For primaries heavier than protons the positive charge excess is reduced and so is the muon charge ratio [73]. In this way we can test the dilution of R_μ due to the neutron enhancement in the primary nuclei. A smaller R_μ value is also expected due to kinematic considerations. The selection of high multiplicity events artificially bias the x_F distribution of muon parents towards smaller values, where the charge ratio is smaller. For single muons the R_μ value integrated over the underground muon spectrum is

$$R_\mu^{unf}(n_\mu = 1) = 1.403 \pm 0.008\,(\text{stat.})^{+0.017}_{-0.015}\,(\text{syst.})$$

to be compared to $R_\mu^{unf}(n_\mu > 1) = 1.18 \pm 0.03$ for muon bundles. This difference of about $\sim 7.2\sigma$ supports the hypothesis of the decrease of the muon charge ratio with increasing primary mass. This is the first indication of such an effect which provides a further handle for the correct understanding and modelling of the secondary production in the atmosphere. With a large statistics, fitting the muon charge ratio as a function of the underground muon multiplicity could disentangle the chemical composition and the hadronic interactions effects discussed above.

The underground muon charge ratio is consistent with past measurements in a similar energy region. Data suggest a slight increase of R_μ with the underground muon momentum, although a fit to a constant charge ratio cannot be excluded ($\Delta\chi^2/dof = 2.48/1$ corresponding to ~1.6 sigma).

The dependence of R_μ on the vertical surface energy $\mathcal{E}_\mu \cos\theta^*$ shows an increase up to ~2 TeV and it is compatible with a model which considers only the π and K contributions to the muon charge ratio. A fit of the low energy data and OPERA data with a simplified description of the atmospheric muon flux provides a value of the pion and kaon charge ratios $R_\pi = Z_{N\pi^+}/Z_{N\pi^-} = 1.2146 \pm 0.0006$ and $R_K = Z_{NK^+}/Z_{NK^-} = 2.583 \pm 0.023$, respectively. The inclusion of the prompt muon component does not modify the fit results. The measured parameter - in particular the kaon charge ratio - could be used to constrain Monte Carlo predictions of multiparticle production. The measurement of the ratio Z_{NK^+}/Z_{NK^-} has also a strong impact on the evaluation of the flux of TeV atmospheric neutrinos, which are dominated by kaon production.

The behaviour of the muon charge ratio above 2 TeV is under investigation. We found a sudden decrease which could be explained invoking three different physical scenarios. A first hypothesis demands a fast increase of the neutron/proton ratio in the primary beam - an idea supported by recent data from the PAMELA and ATIC Collaborations [83, 84]. An alternative explanation relies on the breakup of the Feynman scaling above TeV energies in the fragmentation region, where no experimental data exist. Finally we observe that our measurement lies in the region where the charmed particle production may start to give an observable contribution to the muon charge ratio. A larger statistical sample or an experimental measurement with a new detector at very large depths could shed light on the region $\mathcal{E}_\mu \cos\theta^* \sim 10$ TeV. The data collected by OPERA at the end of its scientific program will allow to improve the measurement in this energy region.

Appendix A

Alignment of the PT System

We describe the procedure followed to align i) PT stations forming a doublet and ii) a doublet with the other ones; in both cases, we treat stations and doublets respectively as indipendent rigid bodies.

For the first case, we use the whole statistics: calling A and B the stations forming a doublet, we use cosmic ray muon tracks to align the second station (B) to the first one (A). We call $\vec{x}_M = (x_M, y_M, z_M)$ the measured coordinates of a particle track in B and $\vec{x}_0$ the corresponding coordinates in B obtained applying a roto-translation with respect to A reference frame. We can write

$$\vec{x}_0 = \mathbf{R}\,\vec{x}_M + \vec{T} \tag{A.1}$$

where $\mathbf{R}$ is the 3D rotation matrix and $\vec{T}$ is the displacement vector. This roto-translated coordinate system has to be equalized to the A reference coordinates (called $\vec{x}_R$) projected on B, using the PT linear fit measured in A:

$$x_R = \beta_R\, z_R + b_R \tag{A.2}$$

where $\beta_R = \tan\phi_A$, the slope of the track in station A, and b_R is the intercept. Equating $x_0 \equiv x_R$, we obtain

$$x_M + R_{xy}y_M + R_{xz}z_M + T_x = \beta_R(z_M + R_{zx}x_M + R_{zy}y_M + T_z) + b_R$$

At the first level, we neglect rotation contributions, and we correct for the dominant translation contributions. We define the residual as

$$x_M - (\beta_R z_M + b_R) = \beta_R T_z - T_x + \text{rotation contributions}$$

Fitting the residual distribution we find out the translation parameters T_x and T_z. These values are used to correct for alignment and we repeat iteratively the whole procedure till the fitted values are compatible with their errors. After three iterations, we reached the statistical accuracy, $\delta\vec{T} \sim 0.1$ mm.

After translation correction, we go back to rotations. By definition, β_R is the slope in the XZ plane in the A reference frame: $\beta_R = x_0/z_0$. Defining $\beta_X = x_M/z_M$ as the XZ slope measured in the B station and β_Y as the YZ slope of the track (measured by the other sub-detectors), we can write

$$\beta_R - R_{xz}\beta_R\beta_X + R_{zy}\beta_R\beta_Y - \beta_X - R_{xy}\beta_Y - R_{xz} = 0 \tag{A.3}$$

Fitting this 3D surface in the slope space, we find out the rotation parameters. Since we obtained values compatible with their errors, $\delta\mathbf{R} \sim 0.1$ mrad, rotation corrections have been neglected.

A similar procedure was followed to align doublets, one with respect to each other. In this case, being separated by the magnet arms, dedicated runs with magnet off were performed. For charge reconstruction, only rotation corrections are significant; at the first iteration, we obtained values compatible with their errors. Moreover, the total statistics accumulated, corresponding to 13.6 days, was used to check and eventually correct for displacement of the $\Delta\phi$ distributions in each magnet arm. We found that the peak position of the distributions are compatible with zero within their statistical accuracy, of the order of 0.2 mrad.

List of Figures

List of Tables

Bibliography

[1] V. F. Hess, Phys. Zeitschr. **13** (1912), 1084.

[2] T. K. Gaisser, *Cosmic Rays and Particle Physics*, Cambridge University Press, Cambridge, 1990.

[3] J. Blumer, R. Engel & J. R. Hörandel, Prog. Part. Nucl. Phys. **63** (2009), 293-338.

[4] P. O. Lagage & C. J. Cesarsky, Astron. Astrophys. **118** (1983), 223.

[5] B. Peters, Nuovo Cimento (Suppl.) **14** (1959), 436.

[6] V. S. Ptuskin, H. J. Völk, V. N. Zirakashvili & D. Breitschwerdt, Astron. Astrophys. **321** (1997), 434-443.

[7] A. D. Erlykin, M. Lipski & A. W. Wolfendale, Astropart. Phys. **8** (1998), 283-292.

[8] A. M. Hillas, Ann. Revs. Astron. Astrophys. **22** (1984), 425.

[9] T. K. Gaisser & T. Stanev, Review of Particle Physics, Cosmic Rays, 2010.

[10] C. Grupen, *Astroparticle Physics*, Springer-Verlag, Berlin, 2005.

[11] T. Stanev, *High Energy Cosmic Rays*, Springer Praxis Books, 2004.

[12] P. Lipari, Astropart. Phys. **1** (1993), 195.

[13] R. P. Feynman, Phys. Rev. Lett. **23** (1949), 1415.

[14] E. Yen, Phys. Rev. D**10** (1974), 836.

[15] R. J. Glauber and G. Matthiae, Nucl. Phys. B**21** (1970), 135.

[16] G. J. Alner *et al.*, Z. Phys. C**33** (1986), 1-6.

[17] W. Heitler & L. Janossy, Proc. Phys. Soc. (London) Sect. A**62** (1949) 374, 669.

[18] T. K. Gaisser, Earth Planets Space **58** (2006), 1-5.

[19] V. A. Naumov, Proceedings of the 2nd Workshop on Methodical Aspects of Underwater/Underice Neutrino Telescopes, Hamburg, 2001; `arXiv:hep-ph/0201310v2`.

[20] W. R. Frazer *et al.*, Phys. Rev D**5** (1972), 1653.

[21] P. K. F. Grieder, *Extensive Air Showers*, Springer-Verlag, Berlin, 2010.

[22] R. N. Cahn and M. B. Einhorn, Phys. Rev. D**4** (1971), 3337.

[23] J. H. Parker *et al.*, in *Proceedings of the 11th ICRC*, ed. by A. Somogyi *et al.* (Akadémiai Kiadó, Budapest, 1970), Vol. X, p. 199.

[24] N. Agafonova *et al.* [OPERA Collaboration], Eur. Phys. J. C**67** (2010), 25-37.

[25] M. Ambrosio *et al.* [MACRO Collaboration], Phys. Rev. D**60** (1999), 032001.

[26] R. Acquafredda *et al.* [OPERA Collaboration], JINST **4** (2009), P04018.

[27] N. Agafonova *et al.* [OPERA Collaboration], JINST **4** (2009), P06020.

[28] N. Agafonova *et al.* [OPERA Collaboration], Phys. Lett. B**691** (2010), 138-145.

[29] Y. Fukuda *et al.* [Super-KamiokaNDE Collaboration], Phys. Rev. Lett. **81** (1998), 1562;
K. Abe *et al.* [Super-KamiokaNDE Collaboration], Phys. Rev. Lett. **97** (2006), 171801.

[30] M. Ambrosio *et al.* [MACRO Collaboration], Eur. Phys. J. C**36** (2004), 323.

[31] D. G. Michael *et al.* [MINOS Collaboration], Phys. Rev. Lett. **97** (2006), 191801;
P. Adamson *et al.* [MINOS Collaboration], Phys. Rev Lett. **101** (2008), 221804.

[32] G. Acquistapace *et al.*, CERN Yellow Report 1998-02 (1998);
`http://proj-cngs.web.cern.ch/proj-cngs`.

[33] C. Amsler *et al.*, Particle Data Group, Phys. Lett. B**667** (2008), 1.

[34] G. L. Fogli *et al.*, Phys. Rev. D**78** (2008), 033010.

[35] L. Arrabito *et al.*, JINST **2** (2007), P05004.

[36] M. De Serio *et al.*, Nucl. Instr. Meth. A**512** (2003), 539-545.

[37] L. Arrabito *et al.*, JINST **2** (2007), P02001.

[38] A. Anokhina *et al.* [OPERA Collaboration], JINST **3** (2008), P07002.

[39] A. Anokhina *et al.* [OPERA Collaboration], JINST **3** (2008), P07005.

[40] T. Adam *et al.*, Nucl. Instr. Meth. A**577** (2007), 523.

[41] A. Cazes *et al.*, JINST **2** (2007), T03001.

[42] S. Dusini *et al.*, Nucl. Instr. Meth. A**508** (2003), 175.

[43] R. Zimmermann *et al.*, Nucl. Instr. Meth. A**555** (2005), 435;
R. Zimmermann *et al.*, Nucl. Instr. Meth. A**557** (2006), 690.

[44] L. Chaussard *et al.*, OPERA Internal Note **29**, 2002.

[45] J. N. Capdevielle *et al.*, KFK Report (1992), 4998; FZKA (1998), 6019.

[46] G. Anelli *et al.*, JINST **3** (2008), S08007.

[47] O. Adriani *et al.*, JINST **3** (2008), S08006.

[48] G. Battistoni, S. Muraro, P. R. Sala, F. Cerutti, A. Ferrari, S. Roesler, A. Fassò, J. Ranft, in *Proceedings of the Hadronic Shower Simulation Workshop*, Fermilab, 2006, M. Albrow, R. Raja eds., AIP Conference Proceeding 896, 31-49, (2007);
A. Fassò, A. Ferrari, J. Ranft and P. R. Sala, CERN-2005-10 (2005), INFN/TC_05/11, SLAC-R-773.

[49] G. Battistoni *et al.*, in *Proceedings of the 20th rencontres de Blois: Challenges in Particle Astrophysics*, ed. by J. Dumarchez and J. T. Thanh Van (The Gioi Publishers, Vietnam, 2008), 283.

[50] M. Ambrosio *et al.*, Nucl. Instr. Meth. A**486** (2002), 663.
P. Lipari, MACRO Internal Notes 88/9 and 91/5.

[51] M. Ambrosio *et al.* [MACRO Collaboration], Phys. Rev. D**56** (1997), 1418.

[52] C. Forti, H. Bilokon, B. D'Ettore Piazzolli, T. K. Gaisser, L. Satta & T. Stanev, Phys. Rev. D**42** (1990), 3668.

[53] G. Battistoni *et al.*, Astropart. Phys. **3** (1995), 157.

[54] N. Mauri, Laurea Thesis, Alma Mater Studiorum, Università di Bologna (2006).

[55] A. Capella *et al.*, Phys. Lett. B**81** (1979), 68; A. Capella *et al.*, Phys. Rev. Lett. **58** (1987), 2015; A. Capella *et al.*, Phys. Rep. **236** (1994), 225.

[56] A. B. Kadailov, Phys. Lett. B**116** (1982), 459; A. B. Kaidalov and K. A. Ter-Martirosyan, Sov. J. Nucl. Phys. **39** (1984), 979.

[57] CMS Collaboration, JHEP**01** (2011), 079.

[58] J. Proudfoot for the ATLAS Collaboration, Nuclear Physics B (Proc. Suppl.) 207-208 (2010), 33-36.

[59] J. Ranft, Phys. Rev. D**51** (1995), 64.

[60] J. N. Capdevielle, J. Phys. G: Nucl. Part. Phys. **15** (1989), 909.

[61] V. N. Gribov, Sov. Phys. JETP **26** (1968), 414; V. N. Gribov & A. A. Migdal, Sov. J. Nucl. Phys. **8** (1969), 583; M. Baker & K. A. Ter-Martirosyan, Phys. Rep. **28**C (1976), 1.

[62] M. Aglietta *et al.*, Astropart. Phys. **20** (2004), 641.

[63] P. Lipari & T. Stanev, Phys. Rev. D**44** (1991), 3543.

[64] G. Battistoni, C. Bloise, A. Ferrari, M. Monteno, V. Patera & E. Scapparone, Astropart. Phys. **7** (1997), 101.

[65] P. K. F. Grieder, *Cosmic Rays at Earth*, Elsevier Science, 2001.

[66] OpRelease Documentation:
`http://operaweb.lngs.infn.it/Opera/software/documentation/OpRelease/index.html`

[67] R. E. Kalman, Transactions of the ASME-Journal of Basic Engineering **82** (Series D), 35-45.

[68] P. V. C. Hough, Proc. Int. Conf. High Energy Accelerators and Instrumentation (1959).

[69] R. Zimmermann, OPERA Internal Note **83**, 2007;
`http://arxiv.org/abs/0706.0800v1, 2008.`

[70] B. S. Wonsak, Ph.D. thesis, Hamburg University, DESY-THESIS-2007-035, 2007 (in German).

[71] M. Ambrosio *et al.* [MACRO Collaboration], Astropart. Phys. **10** (1999), 11.

[72] M. Ambrosio *et al.* [MACRO Collaboration], Astropart. Phys. **19** (2003), 313-328.

[73] G. Battistoni *et al.*, *Proceedings of the 31st ICRC*, Lodz, Poland, 2009.

[74] J. R. Hörandel, Astropart. Phys. **19** (2003), 193.

[75] J. K. de Jong for the MINOS Collaboration in *Proceedings of the 31st ICRC*, Lodz, Poland, 2009.

[76] P. Achard *et al.*, Phys. Lett. B**598** (2004), 15.

[77] G. K. Ashley II *et al.*, Phys. Rev. D**12** (1975), 20.

[78] P. Adamson *et al.* [MINOS Collaboration], Phys. Rev. D**76** (2007), 052003.

[79] P. Schreiner and M. Goodman for the MINOS Collaboration, in *Proceedings of the 30th ICRC*, ed. by R. Caballero *et al.* (Universidad Nacional Autónoma de México, Mexico City, Mexico, 2008) Vol. 5, p. 1221.

[80] N. Agafonova *et al.*, in *Proceedings of the 31st ICRC*, Lodz, Poland, 2009.

[81] E. V. Bugaev *et al.*, Phys. Rev. D**58**, 054001 (1998).

[82] L. V. Volkova and G. T. Zatsepin, Phys. At. Nucl. **71** (2008), 1782.

[83] O. Adriani *et al.*, Science, Vol. 332, No. 6025 (2011), 69-72.

[84] A. D. Panov *et al.*, Bulletin of the Russian Academy of Sciences: Physics Vol. 73, No. 5 (2009), 564-567.